Technische Universität München

Lehrstuhl für Biologische Bildgebung

All-optical Ultrasound Detection for Optoacoustic Imaging

Georg Wißmeyer

Vollständiger Abdruck der von der Fakultät für Elektrotechnik und Informationstechnik der Technischen Universität München zur Erlangung des akademischen Grades eines

Doktors der Naturwissenschaften (Dr. rer. nat.)

genehmigten Dissertation.

Vorsitzender: Prof. Dr.-Ing. Klaus Diepold

Prüfer der Dissertation:

1. Prof. Dr. Vasilis Ntziachristos

2. Prof. Dr. rer. nat. Axel Haase

3. Prof. Dr.-Ing. Christian Jirauschek

Die Dissertation wurde am 18.04.2019 bei der Technischen Universität München eingereicht und durch die Fakultät für Elektrotechnik und Informationstechnik am 13.11.2019 angenommen.

Abstract

Physiology aims at understanding the fundamental physical and biochemical processes in organisms, ranging from unicellular microorganisms on the nanometre scale up to sections of multicellular plants and animals on the decimetre scale. Biomedical imaging is the most relevant tool for studying physiology and disease, as it allows the visualization of morphology and functionality that is either too small to be resolved by the human eye or that is obscured by overlaying tissue. Among the many imaging modalities, optoacoustic (photoacoustic) imaging has gained increasing attention over the past two decades. The optoacoustic principle combines optical absorption contrast with acoustic resolution at increased imaging depths and allows for label-free and non-invasive imaging, resulting in an imaging method that is harmless for biological tissue.

Although optoacoustic imaging has advanced dramatically with applications devised in tomography, microscopy and endoscopy, it has not achieved a clinical breakthrough yet, mainly due to the limited performance of applied piezoelectric detectors. In response to the need for sophisticated optoacoustic sensors, this thesis is dedicated to all-optical methods for ultrasound detection.

The first part reviews the field of existing ultrasound sensors as well as their typical applications, ranging from classic piezoelectric elements based on lead zirconate titanate (PZT) to advanced detectors based on optical interferometry.

The second part introduces the application of fiber-based Fabry-Pérot resonators (π-BGs) in optoacoustic microscopy for the first time. The detection schemes are characterized in terms of sensitivity and frequency response and are furthermore applied to optoacoustic imaging of biological specimen, such as *ex vivo* zebrafish and *in vivo* mouse models.

The final part describes the development of a novel optical resonator, the Asymmetric Etalon (AsE). The sensor is characterized and its suitability for imaging applications is validated by imaging *ex vivo* samples using methods suitable for optoacoustic endoscopy.

Contents

List of Abbreviations

π-BG π-shifted Bragg Grating

π-FBG π-shifted Fiber Bragg Grating

1D 1-dimensional

2D 2-dimensional

3D 3-dimensional

AR Acoustic Resolution

ASE Amplified Spontaneous Emission

AsE Asymmetric Etalon

BG Bragg Grating

CA Coronary Angiography

CCD Charge Coupled Device

CMUT Capacitative Micromachined Ultrasound Transducer

CRF Coherence Restoring Filter

CRPI Coherence Restored Pulsed Interferometry

CT Computed Tomography

CW Continuous Wave

DAQ Data Acquisition

EDFA Erbium-Doped optical Fiber Amplifier

FBG Fiber Bragg Grating

FD Frequency Domain

FM Fluorescence Microscopy

FOV Field Of View

FSR Free Spectral Range

FWHM Full Width at Half Maximum

ICG Indocyanine Green

IVUS Intravascular Ultrasound

LED Light Emitting Diode

LUS Laser Ultrasonics

MIP Maximum Intensity Projection

MM Multi Mode

NA Numerical Aperture

NDT Non-Destructive Testing

NEP Noise Equivalent Pressure

NIR Near-Infrared

OAM Optoacoustic Microscopy

OAT Optoacoustic Tomography

OCT Optical Coherence Tomography

OR Optic Resolution

PCI Percutaneous Coronary Intervention

PI Pulsed Interferometry

PM Polarization Maintaining

PMT Photomultiplier Tube

PMUT Piezoelectric Micromachined Ultrasound Transducer

PVDF Polyvinylidene Fluoride

SHG Second Harmonic Generation

SM Single Mode

SNR Signal-to-Noise Ratio

SOI Silicone On Insulator

TD Time Domain

THG Third Harmonic Generation

US Ultrasound

WD Working Distance

1 Introduction

1.1 Biomedical Imaging

Biomedical imaging is a crucial tool for both basic biological research as well as for disease diagnosis. In its fundamental interpretation, biomedical imaging describes the technology of visualizing the anatomy and functionality of biological specimens from the cellular level up to entire organisms. It includes research on fundamental physiological processes, anatomical mapping of organisms, monitoring of biomarkers of health and disease, development of medical treatments, and monitoring of patient response to those treatments.

The physical principles of biomedical imaging differ by modality. The most common contrast mechanisms are based on optical absorption (e.g. bright-field microscopy), X-ray absorption (e.g. X-ray radiography and computed tomography), magnetic resonance (e.g. magnetic resonance tomography), radioactive tracers (e.g. positron emission tomography) and acoustic absorption (e.g. ultrasound transmission tomography) [1].

Research on biomedical imaging technologies focuses on pursuing novel modalities as well as on advancing established technologies with the aim of an improved understanding and treatment of diseases. Among prevalent imaging technologies, ultrasonography and X-ray imaging have had a particularly widespread impact on clinical diagnosis in the past century. However, these prevalent technologies exhibit crucial deficiencies, such as limited contrast in biological tissue, restricted imaging depths or the utilization of ionizing radiation. As a consequence, a number of new imaging methods have emerged in recent decades and an overview is depicted in Figure 1.1, with the respective spatial resolutions mapped against the imaging depths. While the map reveals how the established biomedical imaging technologies complement one another, it also reveals that imaging deep inside tissue at high resolution has not been achieved yet. Thus, the current frontier of biomedical imaging is the challenge of increasing both imaging depth and image resolution in tissue, while simultaneously keeping radiation levels within legal limits of safe exposure (see Appendix).

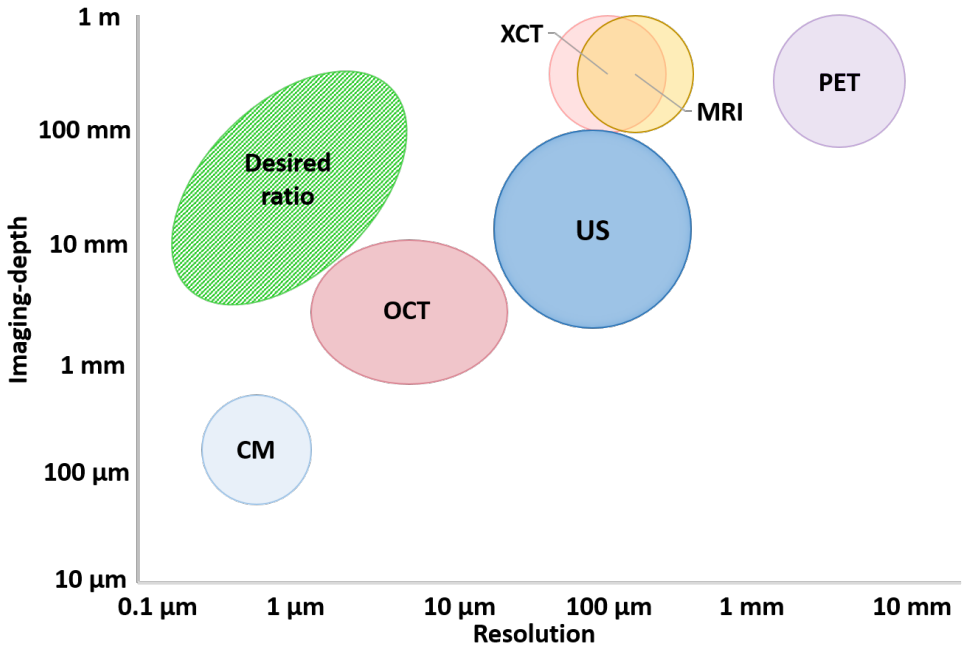

Figure 1.1: Comparison of biomedical imaging technologies: The resolution of established modalities is schematically arranged against the respective imaging depth [2–4]. The desire for improved resolutions at higher depths is the driving force behind efforts to research and develop optoacoustic imaging. (CM, Confocal Microscopy; MRI, Magnetic Resonance Imaging; OCT, Optical Coherence Tomography; PET, Positron Emission Therapy; US, Ultrasonography; XCT, X-ray Computed Tomography.)

In pulse-echo ultrasonography, also referred to as medical ultrasound imaging, ultrasound waves are emitted from a single transducer element or a transducer array and the acoustic waves echoing off structures within tissue are recorded by the same element or array. The recorded signals can then be reconstructed as 2D or 3D images with the image contrast given by varying acoustic impedances in tissue. Ultrasound imaging offers mediocre resolution, and its applicability e.g. at tissue-bone interfaces is limited; however, it does provide imaging depths in the range of centimetres as well as the great advantages of live imaging and harmless interaction with living tissue [4]. Diagnostic ultrasonography usually operates at maximum acoustic pressures of around 1 MPa and at acoustic frequencies of 1 - 10 MHz, both regimes that are not hazardous to tissue (see Appendix). Another advantage of medical ultrasound imaging comes with the simplicity of ultrasound imaging systems, ultimately allowing high portability and low operating costs.

Magnetic resonance imaging (**MRI**) applies an intensive oscillating magnetic field to

generate polarized hydrogen atoms inside tissue, and a radio-frequency (**RF**) system then excites and detects the magnetic resonance e.g. of hydrogen atoms. Hence, MRI contrast is based on the location and density of hydrogen atoms, primarily in fat and water inside tissue. MRI allows for whole-body imaging enabled by high penetration depths and resolutions on the sub-millimetre scale, even deep inside tissue. As MRI does not apply ionizing radiation and exhibits high contrast in soft tissue, it has proven to be particularly valuable for medical imaging and was therefore heralded for many years as the future of biomedical imaging. However, the technology for MRI imaging is very complex and depends on a sophisticated apparatus to generate strong magnetic fields and operate the RF detectors. Consequently, the resulting high costs for its purchase and operation limit broad application of this imaging modality. Moreover, MRI does not yet offer spatial resolutions in the sub-μm to μm regime and is limited in terms of available contrast media [5].

Similar to MRI, X-ray radiography and X-ray computed tomography (**CT**) can achieve penetration depths that allow for full-depth imaging of the human body at resolutions of up to 100 μm. The absorption contrast of X-rays is particularly suitable to image anatomical features and its straightforward design has made X-ray-based imaging systems standard equipment in hosptials, clinics, and private practices. The major drawback of X-ray-based methods is the ionizing nature of X-ray radiation, which poses a severe health risk as it can damage living tissue - in particular DNA - and may lead to mutations and cancer [6].

Optical contrast methods, such as confocal microscopy (**CFM**), have pushed the boundaries of spatial resolution down into the range of 500 nm and better [7], but their penetration depths do not exceed 100 μm due to extensive scattering (diffusion) of light in tissue. Optical scattering occurs to a varying degree across the entire optical EM spectrum; the degree of scatter depends on parameters such as the photon energy and the type and thickness of the interrogated medium. Light propagating in biological samples such as human tissue experiences scattering and becomes fully diffusive at depths ranging between 0.3 to 1 mm. Therefore, optical scatter is regarded as the fundamental limitation to purely optical imaging modalities [2].

In summary, the advancement of biomedical imaging stands or falls with increasing imaging depth and improving image resolution while minimizing associated health hazards such as ionizing radiation. Moreover, there are a number of practical aspects to novel imaging modalities, such as detector size and image acquisition speed, that determine how well an imaging modality can be translated to clinical applications.

1.2 Motivation for Optical Ultrasound Detection

Optoacoustic imaging - commonly referred to also as photoacoustic imaging [8] - is an alternative imaging method to purely optical imaging, and it has gained increasing attention over the past two decades. It allows for improved imaging depths without utilizing radiation harmful to tissue [2, 9]. Image contrast originates as a result of two processes: photon absorption in tissue and the optoacoustic effect. In general, light can interact with matter in three different ways: transmission, scattering and absorption [10].

In optically transparent or very thin media, photons may be transmitted without any form of interaction and consequently without a change in photon energy or direction of propagation. Inside a medium of different composition or density, photons may be deflected or deviated from their original path by scattering elements ranging from gas molecules in air to organic molecules in tissue. Alternatively, photons may be absorbed inside a medium in a process where the photon energy is partially or completely transferred to an absorber and it is this photon absorption that is essential for optoacoustic signal generation. Upon absorption, some or all of the photon energy is converted into heat, followed by a thermoelastic expansion at a specific location in the medium. This expansion creates acoustic waves that serve as optoacoustic (or photoacoustic) signals. Typically optoacoustic imaging detects only acoustic waves at ultrasound frequencies, utilizing ultrasound transducers and methods similar to the ones applied in pulse-echo ultrasound imaging [4]. The physical principle of the optoacoustic effect is discussed in more detail in chapter 2.

One of the key advantages of optoacoustic imaging is the increase in imaging depth over what can be achieved with purely optical methods, since optoacoustic imaging detects acoustic waves, which in tissue experience scattering two to three orders of magnitude weaker than light, particularly in the visible spectrum [2, 11]. In typical fluorescence imaging of tissue, both excitation light and emitted light undergo heavy scattering along their respective optical paths, limiting meaningful imaging to depths of 80 - 100 μm in the case of fluorescence microscopy and to depths of 400 - 700 μm in the case of fluorescence tomography [12]. In contrast, optoacoustic microscopy has been demonstrated with imaging depths of 3 mm [13] and optoacoustic tomography with depths of up to 5 cm [14]. The unique depth advantage of optoacoustic imaging has had a major impact on biomedical imaging in the past two decades [15, 16].

While the benefits of optoacoustic imaging are well-known in the biomedical imaging community, neither optoacoustic microscopy, tomography, nor endoscopy has yet achieved

a breakthrough in clinical translation. One of the key reasons for this standstill lays in the historical development of optoacoustic imaging: still today, piezoelectric sensors are the ultrasound detectors most commonly applied to optoacoustic imaging, but they were originally developed for classic pulse-echo ultrasonography, where acoustic signals are around three orders of magnitude stronger [17]. Thus, today's ultrasound detectors do not offer adequate sensitivity for many demanding clinical applications, despite the improvements in piezoelectric materials and focused sensing geometries. In addition to sensitivity, miniaturization is another challenge: many clinical applications require imaging devices small enough for handheld scanning or integration into a catheter endoscope. Since the physical dimensions of the piezoelectric element determine its sensitivity and frequency response, most piezoelectric sensors cannot be miniaturized enough to meet the requirements of e.g. optoacoustic endoscopy or reflection-mode microscopy.

These challenges are illustrated in the following subsections, which describe two published studies that demonstrated the need to push the field of optoacoustic imaging further. The two studies contributed to the initial research in the framework of this thesis and involved intravascular endoscopy [18] and gastrointestinal endoscopy [19], where sensor miniaturization as well as sensor sensitivity are key for clinical translation. The studies helped to identify and demonstrate general technical limitations in the applicability and functionality of state of the art sensors as biomedical imaging devices. They also showed how optoacoustic imaging can complement or replace certain imaging modalities, avoiding their intrinsic limitations.

1.2.1 Example 1: Intravascular Endoscopy

In cardiology, the most commonly applied diagnostic imaging approach for percutaneous coronary intervention guidance is coronary angiography (**CA**). In this technique, a contrast medium that can be visualized using X-ray imaging is flushed through vasculature such as coronary arteries using an intravascular catheter. In this way, CA visualizes changes in the vasculature lumen, such as thrombosis and occlusion. However, CA involves harmful ionising radiation and the use of a catheter can cause vascular complications. To avoid these limitations, novel intravascular imaging technologies have recently been investigated [20].

Pulse-echo intravascular ultrasound (**IVUS**) endoscopy was first introduced by Yock et al. in 1989 [21] and more recently, high-frequency IVUS techniques have become the intravascular imaging techniques most commonly used in clinical applications [20]. IVUS

provides complementary contrast to CA by quantifying vessel wall thickness as well as the extent of arteriosclerotic plaque thickness. It therefore provides the possibility of diagnosis and management of cardiovascular diseases, including critical indications such as during coronary stent placement. Here, the typical imaging depth with a 40 MHz piezoelectric IVUS transducer is around 5 mm, and the axial and lateral resolutions are 270 μm and 500 μm, respectively [18].

Another imaging modality for intravascular endoscopy is optical coherence tomography (**OCT**). Intravascular OCT was first introduced by Tearney et al. in 1996 [22] and was soon successfully applied in clinical translation. Similar to IVUS, OCT allows imaging of vascular morphology and therefore enables the visualisation of arteriosclerotic plagues, implants such as coronary stents, and features of cariodvascular diseases that affect lumen diameter and wall thickness. A typical imaging depth of around 1 - 2 mm is achieved with axial resolution on the order of 20 μm and lateral resolution around 30 - 40 μm that are governed by the applied focusing optics [22] (Figure 1.1).

Although IVUS and OCT play an important role in clinical diagnosis, both modalities visualize and quantify only morphological features, yet it is also important to examine metabolic and functional aspects of tissue, since processes such as inflammation can contribute to arterosclerotic plaques. This requires another modality of complementary contrast that allows the overlay of morphological and metabolic information.

Near-infrared fluorescence (**NIRF**) imaging is an imaging modality that allows the detection of tracers such as molecular reporters and fluorophores in biological tissue and can therefore provide complementary contrast to morphological imaging provided by IVUS. Consequently, a hybrid IVUS and NIRF intravascular catheter system was seen as a promising approach to further improve diagnosis and management of cardiovascular disease.

Figure 1.2 demonstrates the catheter setup developed for *in vivo* intravascular imaging. The main components of the experimental setup included the optical light delivery and collection via photomultiplier tube (**PMT**) of the NIRF modality, ultrasound signal generation and collection by piezoelectric transducer for the IVUS modality as well as the back-end for mechanical movement of the sensor and data recording. The subject was administered indocyanine green (**ICG**) by systemic injection, then NIRF imaging was used to image the distribution of the dye as a measure of impaired endothelial permeability. For histology imaging, both ICG and autofluorescence from fluorescein isothiocyanate (**FITC**) were recorded.

Figure 1.3 shows cross sectional IVUS and co-registered NIRF images of a swine iliac

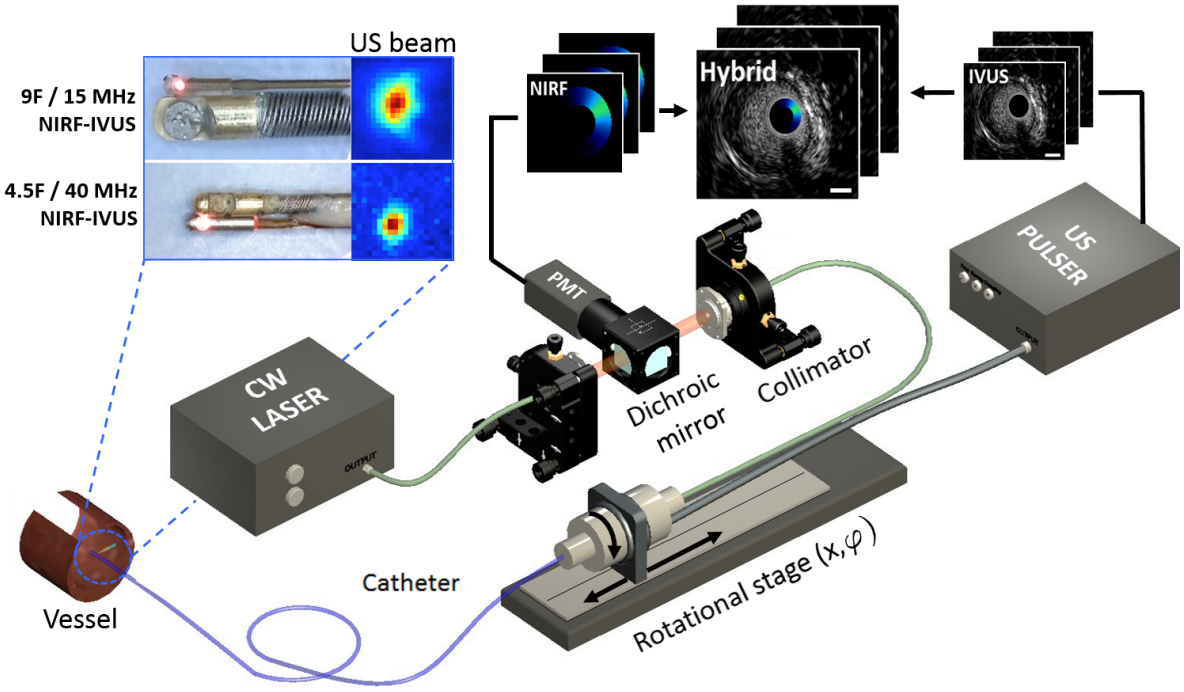

Figure 1.2: Design and operation mode of the hybrid IVUS-NIRF imaging system for intravascular endoscopy: The sensor head employed either a 15 MHz or 40 MHz ultrasound module driven by an ultrasound pulser and a rigidly coupled optical fiber for the NIRF modality. Illumination was provided by a 750 nm continuous-wave-laser and a photomultiplier tube was used to detect fluorescence signal. The hybrid catheter was rotated and moved along the axis of the vessel with the help of an electro-optical rotational coupler and a (x, φ) rotational stage. A back-end system first recorded and processed signals of the NIRF and IVUS modality individually, then combined the morphological and metabolical information into a hybrid image.

artery *in vivo*. The artery was inflated by an angioplasty balloon and the injured areas could then be identified by NIRF contrast, whereas IVUS was not able to localize the injuries. Fluorescence microscopy (**FM**) and histology of the excised artery confirmed the injured regions identified by NIRF. Further details of the imaging setup, the *in vivo* experiments and the signal processing were published in the related article by Bozhko et al. [18].

The findings presented in this pilot study demonstrated the feasibility of hybrid NIRF-IVUS *in vivo* imaging under realistic clinical conditions and highlighted the value of complementary morphological and metabolical contrast. As a result, this approach could lead to a new diagnosis tool for cardiologists, supporting decisions between surgical intervention or medication-based treatment. At the same time, the spatial resolution

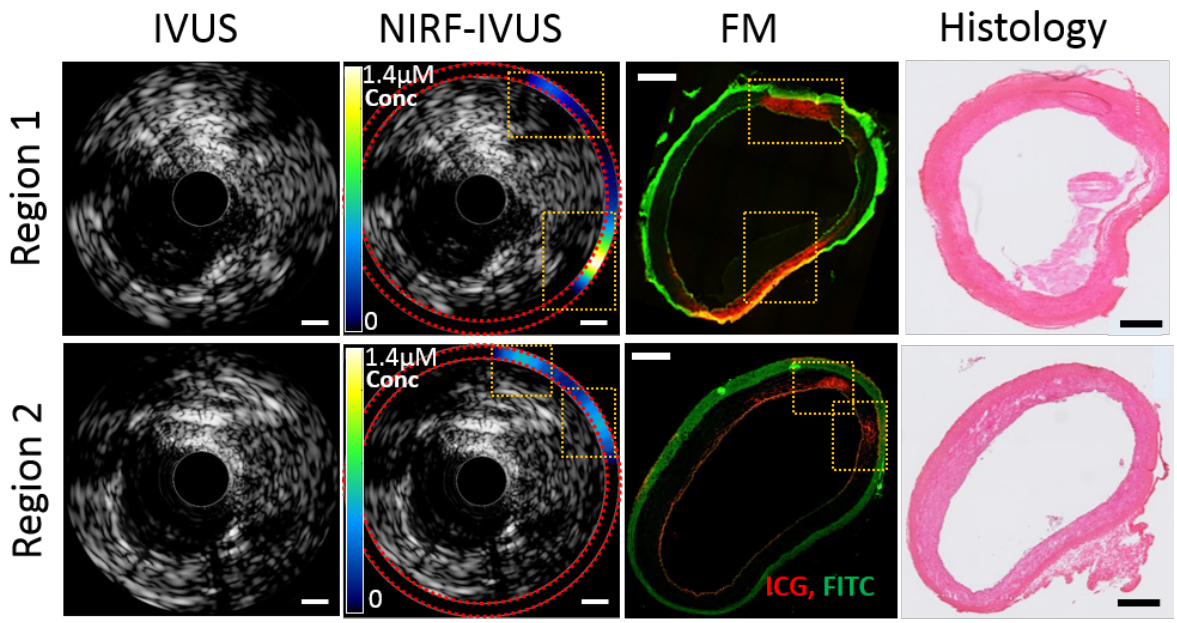

Figure 1.3: ***In vivo*** **cross sectional images of two regions of an injured swine iliac artery:** IVUS images were recorded with a 15 MHz ultrasound module and reveal the vessel morphology but not the injury location (scale bar, 1 mm). Hybrid NIRF-IVUS images highlight injured regions as labelled by ICG aggregation (yellow boxes)(scale bar, 1 mm). Fluorescence micrographs with ICG depicted in red and FITC autofluorescence in green, as well as histology images for comparison (FM and histology scale bars, 0.5 mm).

achieved by IVUS was too poor for detailed morphological readout and sophisticated diagnosis of vascular wall conditions. The reason for this limitation is lack of sensitivity and frequency bandwidth in the piezoelectric ultrasound transducers. The NIRF modality suffers from its inherent limitation given by optical scattering in tissue and was therefore not able to penetrate deep into the vessel wall in order to e.g. overlay NIRF and IVUS signals at depths exceeding few hundreds of microns.

Here, optoacoustic imaging could be a potent alternative or supplementary modality as it combines the advantages of an enhanced imaging depth with improved optical absorption contrast as well as improved image resolution (see chapter 2 for a detailed discussion). Additionally, the optoacoustic modality could target a variety of optical absorbers via multi-spectral illumination at the same time, possibly avoiding the need for multiple modalities within one device and therefore dramatically reducing the size of the overall sensor head.

However, the relatively poor sensitivity of the applied miniaturized ultrasound detectors

bars the existing combination of components for illumination and ultrasound detection from being used for optoacoustic imaging. With sophisticated ultrasound detectors, intravascular optoacoustic imaging at optical resolutions could provide morphological, metabolic and functional information at spatial resolutions of below 20 μm [23], but this advance seems long in coming, despite recent advances in the micro-fabrication of ultrasound transducers (see chapter 3).
Instead, an all-optical combination for both light delivery for optoacoustic excitation as well as optical detection of ultrasound [24] could be a game changer for cardiovascular endoscopy, by simultaneously decreasing sensor-size, increasing image resolution, and allowing label-free imaging of various absorbers and fine morphological features.

1.2.2 Example 2: Gastrointestinal Endoscopy

Currently, classic white light endoscopy (**WLE**) is the most commonly applied form of endoscopic imaging and is complemented by other modalities such as confocal laser endoscopy (**CLE**) and fluorescence imaging [25,26]. However, WLE is capable of imaging only the lumen surface, and other techniques such as CLE have an insufficient penetration depth into the lumen wall. As a consequence, these modalities are insufficient to examine the sub-surface gastrointestinal morphology and provide early disease detection, which is vital for e.g. the visualization of prodromal cancer stages [25].
Optoacoustic endoscopy allows imaging of the lumen wall at depths of hundreds of μm and with high resolution, based only on the intrinsic optical absorption contrast of the tissue and without the need for labelling. Similar to optoacoustic microscopy (**OAM**), optoacoustic endoscopy can be performed in acoustic resolution (**AR**) and in optical resolution (**OR**) modes (see chapter 2). While the AR modality is usually resolution limited by US diffraction in the commonly focused piezoelectric ultrasound detector, AR endoscopy allows imaging deeper than 1 mm, exceeding the normal thickness of a lumen wall. OR setups, in contrast, achieve superior resolutions of around 10 μm, but are affected by light scattering and are not suitable for imaging tissue morphology deeper than around 0.3 - 0.5 mm. In this context, a hybrid optical and AR endoscope design for optoacoustic imaging was elaborated, utilizing a piezoelectric transducer. The resulting combination of AR and OR modalities into a hybrid endoscope was tested in terms of penetration depth as well as resolution at various imaging depths in phantoms and *ex vivo* tissue samples [19].
Figure 1.4a visualizes the interrogation and operation setup of the endoscopic probe including light delivery and data acquisition. The suggested probe design includes a multi-

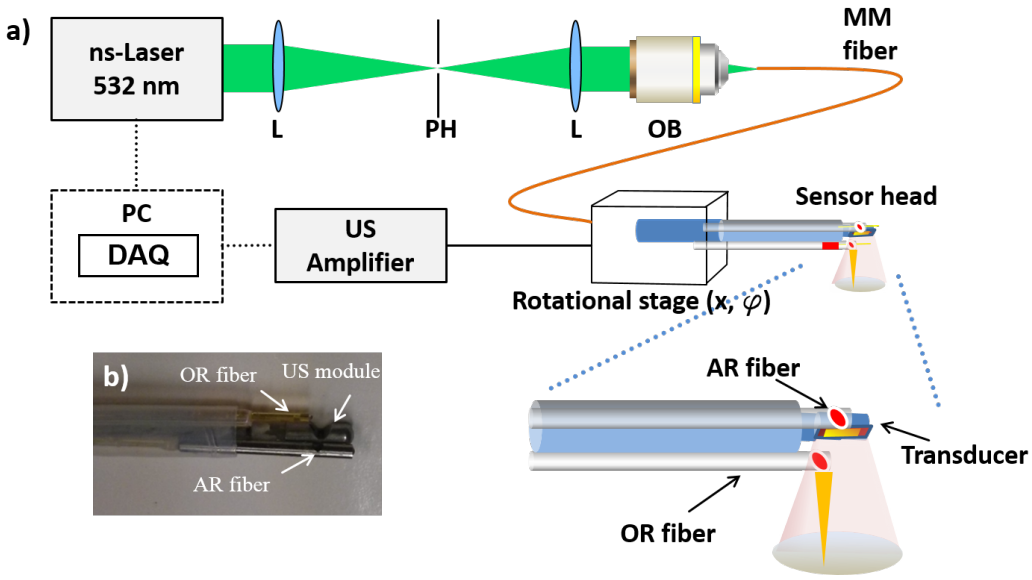

Figure 1.4: Experimental setup for hybrid AR and OR optoacoustic endoscopy: (a) Light delivery, optoacoustic signal detection and scanning mechanism. (b) Close-up of the hybrid sensor head.

mode optical fiber for alternating light delivery for broad illumination in the AR-mode and for focused illumination via a gradient index (**GRIN**) lens in the OR-mode. The hybrid sensor head also featured a piezoelectric module for the detection of optoacoustic signals and is depicted in Figure 1.4b.

Figure 1.5 shows a bright-field microscopy image and a set of optoacoustic images taken from an *ex vivo* mouse ear. The AR image resolved bigger blood vessels in the range of 80 - 100 μm, and the OR image resolved smaller vessels in the range of single μm up to few tens of μm. While the OR images demonstrated good resolution and imaging of superficial vascular morphology, the AR modality achieved deeper imaging governed by the focal distance of the piezoelectric element. However, both modalities failed to adequately image the fine and continuous network of blood vessels visible in the bright-field image. Further details of the setup, the system characterization as well as a detailed discussion were published in the related article by He et al. [19].

While the resulting images were encouraging for the further development of (hybrid) optoacoustic gastrointestinal endoscopy probes, two fundamental limitations of the demonstrated system became apparent:

1. The sensitivity of the applied piezoelectric ultrasound detector was too low to achieve high SNR in the AR modality, and it also impeded the visualization of fine

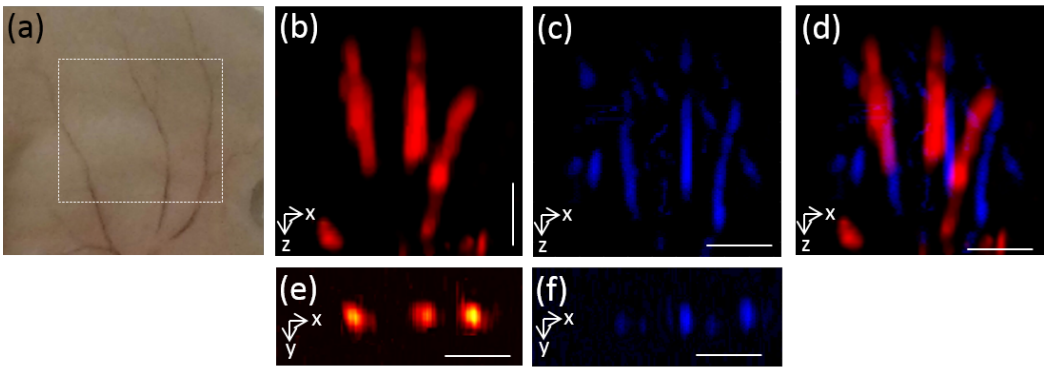

Figure 1.5: ***Ex vivo*** **images of vasculature in a mouse ear:** (a) Bright-field microscopy image with a white rectangle highlighting the ROI for AR and OR imaging. (b) AR modality. (c) OR modality. (d) Hybrid AR and OR image. (e)-(f) Cross sections of the AR and OR modality, respectively. Scale bars, 0.5 mm.

morphological features in the OR modality.

2. The acoustic focus of the applied piezoelectric ultrasound detector limited the lateral resolution in the AR modality to around 200 μm at depths of 1 mm.

Optical ultrasound detectors could overcome these limitations and improve the performance of an optoacoustic endoscopy probe. In contrast to piezoelectric elements, the sensitivity of optical ultrasound detectors does not necessarily scale with the detector size. Hence, detector miniaturization for the application in an endoscopy probe does not reduce the detector sensitivity and optical detectors could therefore increase contrast in both the AR as well as the OR modality. Furthermore, the optoacoustic images in the presented AR modality are maximum intensity projections (**MIP**) recorded with a single ultrasound detector and the scanning of the probe-head was performed by simultaneous cylindrical rotation and linear movement. Hence, a dense and miniaturized array of ultrasound detectors could increase image resolution and drastically simplify the scanning process [2]. However, piezoelectric transducers cannot be arranged in such dense and miniaturized arrays, primarily because of a loss in sensitivity due to miniaturization, but also due to manufacturing considerations such as the dicing and wiring of individual piezoelectric elements. Capacitative micro-machined ultrasound transducers (**CMUTs**) and piezoelectric micro-machined ultrasound transducers (**PMUTs**) are currently investigated for similar applications, but it is the all-optical detection of ultrasound that presents the most promising approach for ultrasound detection in sophisticated optoacoustic imaging modalities.

1.3 Thesis Objectives

The motivation to perform research on novel technologies for ultrasound sensing came from the studies in section 1.2, where the limitations of present sensors for endoscopic applications became apparent. Following these insights, the aim of the research presented in this thesis was to investigate the theoretical and experimental applicability of optical ultrasound detection schemes in order to substitute prevalent piezoelectric devices. Optoacoustic imaging first became possible as a result of piezoelectric sensors, but the imaging modality has now advanced beyond the confined capabilities of this sensing technology. In other words, the extremely weak acoustic signals generated in optoacoustics require sensor bandwidths and sensitivities that exceed those supplied by piezoelectric technologies. Furthermore, sensor footprint is an elementary factor when investigating optoacoustic imaging in demanding applications, such as intravital endoscopy and microscopy of thick samples. Only through improvements in ultrasound detection can optoacoustic imaging advance towards the next generation of applications, such as intra-cellular and epi-illumination (reflection-mode) microscopy, high-resolution tomography, and intravascular endoscopy.
In light of the motivation stated above and the need for advanced acoustic detectors, the aim of this thesis can be divided into three parts:

1. Analysis and review of the current research and state of the art on ultrasound detectors for optoacoustic imaging.

2. Transfer and application of an all-optical ultrasound sensing technique to a prevalent optoacoustic imaging application (multi-modal microscopy).

3. Development and application of advanced optical ultrasound sensors and corresponding read-out methods.

1.4 Thesis Outline

Following the research goals and motivation for this work, the dissertation is structured into six chapters:
Chapter 1 puts optoacoustics into relation with prevalent well-established imaging techniques, emphasizing its distinct advantages by discussing two experiments performed in intravascular and gastrointestinal endoscopy, respectively.
Chapter 2 then discusses theoretical aspects of optoacoustics, in particular the underlying

photoacoustic effect as well as its eventual implementation in optoacoustic tomography, microscopy and endoscopy.
Chapter 3 gives an account of the current state of the art for ultrasound detectors and is based on a review about predominant ultrasound detection based on piezoelectric sensors, micromachined transducers and optical ultrasound sensors. In the context of optical ultrasound sensors, various interferometric and non-interferometric sensing approaches as well as corresponding interrogation and read-out methods are discussed.
Chapter 4 then addresses the first application-driven part of the thesis, where an optical ultrasound sensor, based on a π-FBG resonator, is implemented into a microscopy setup for the first time. Here, the novel sensor is characterised and its performance is demonstrated by hybrid bright-field and optoacoustic microscopy images of inorganic phantoms and *ex vivo* samples.
Chapter 5 advances from the findings discussed in chapter 4 and introduces an all-optical microscopy setup, where multi-photon fluorescence is combined with optoacoustics by employing an acoustic reflector for reflection-mode imaging. The setup is characterized accordingly and its performance subsequently demonstrated by hybrid microscopy imaging of thick *in vivo* specimen.
Chapter 6 introduces a novel detector design, conceived and fabricated for the first time in the framework of this thesis. Throughout the chapter, emphasis is put on its underlying design, its manufacture and characterization as well as on its possible application in optoacoustic endoscopy and the related field of ionoacoustics.
Chapter 7 completes the work by summarizing the presented research and putting it into context of current findings in the literature. In addition, it highlights the great potential of optical ultrasound detection and introduces prospective approaches of optical sensors tailored for optoacoustic imaging.

2 Optoacoustic Imaging

2.1 Introduction

Optoacoustic imaging introduced demanding requirements on ultrasound detectors in terms of sensitivity, bandwidth and detector size. Moreover, these requirements vary fundamentally for different optoacoustic imaging modalities, in particular for tomography and microscopy, and it is vital to achieve a better understanding of these modalities when developing novel ultrasound detectors. The following chapter therefore provides a theoretical basis about optoacoustic imaging as well as about the individual aspects of optoacoustic tomography, microscopy and endoscopy. It includes a discussion about the interaction of light with matter, the photoacoustic effect as well as absorbers such as endogenous or exogenous chromophores which are the source of contrast in optoacoustic imaging. Moreover, the generation and detection of optoacoustic signals as well as methods for signal processing and image reconstruction of the respective imaging modalities are discussed. The chapter is based on [2, 11, 27–32] and further in-depth sources on optoacoustic tomography and microscopy can be found e.g. in [9, 33] and [8, 34], respectively.
Findings and insights presented and discussed in this chapter were incorporated into publications related to this thesis. In particular, observations that affected the design of optoacoustic detectors in terms of bandwidth and sensing geometry were published in [17, 19, 35].

2.2 The Photoacoustic Effect

The principle of optoacoustic imaging is based on the photoacoustic effect and has been first described by Alexander Bell in 1880 [36]. However, extended research on this field was not performed before the 1960s, at the dawn of spectrally pure and powerful lasers which enabled a controlled generation of optoacoustic signals [37]. The photoacoustic effect was applied in the related field of laser ultrasonics before [38], but the transition

towards biomedical imaging was first performed in the mid-1990s and initial *in vivo* images with meaningful quality were published in the 2000s [9,37]. While the motivation for optoacoustic imaging has already been described in section 1.2, it might be relevant to point at the main challenge for the advancement of optoacoustic imaging once again: the development of highly sensitive and broadband ultrasound transducers. Similar to the broad availability of piezoelectric transducers in the 1990s and 2000s that led to the rise of optoacoustics, a new generation of ultrasound transducers has the potential to pave the way for advanced optoacoustic modalities such as imaging of sub-micron absorbers (nanoscopy) or the creation of ultra-dense arrays for minimally invasive tomographic endoscopy [17].

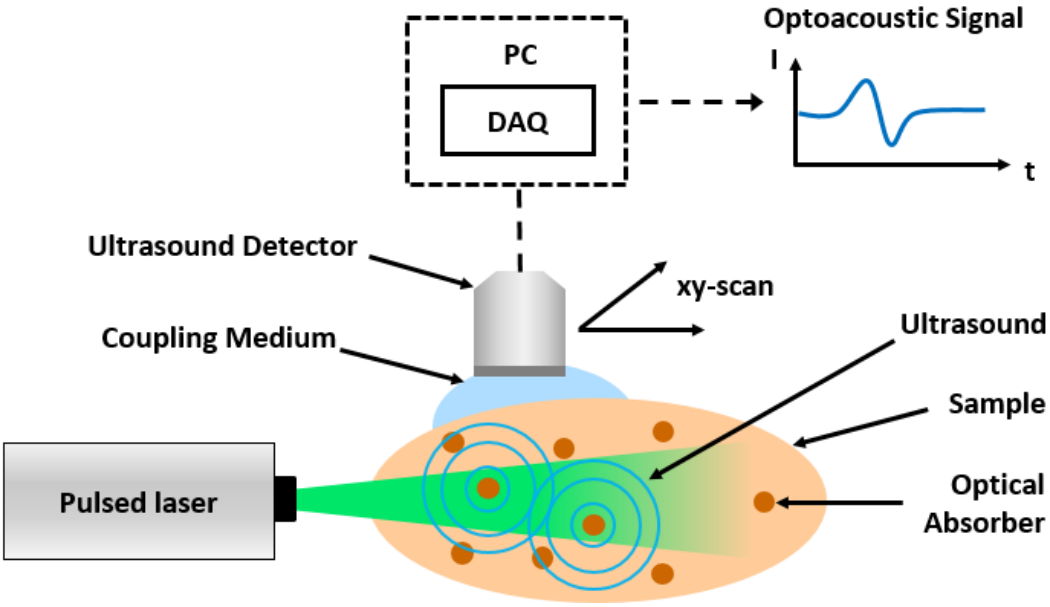

Figure 2.1: The principle of optoacoustic imaging: A pulsed laser source illuminates a given sample and upon optical absorption, the absorbed energy is converted into heat. The corresponding local temperature rise then results in a thermoelastic expansion and the subsequent generation of acoustic waves.

The underlying photoacoustic effect is depicted in image Figure 2.1. Here, a medium (such as a biological tissue sample) is irradiated by non-ionizing laser pulses and upon photon absorption by particles inside the medium, the subsequent heating and thermoelastic expansion generates ultrasonic waves that spread spherically. These ultrasonic waves can then be detected by ultrasound detectors and the recorded signals processed in order to create a biomedical image. In its fundamental layout, optoacoustic signal processing and image reconstruction can be performed by methods analogous to those applied in classic ultrasonography.

Optoacoustic imaging and its submodalities strongly depend on the wavelength of the applied excitation light as well as on the nature of the examined absorbers, such as endogenous and exogeneous chromophores in tissue. Therefore, essential physical principles of the photoacoustic effect, such as the light-matter interaction, the non-radiative relaxation as well as the photoacoustic wave equation are discussed in the following subsections.

2.2.1 Light-Matter Interaction

Interaction Mechanisms

The interaction of photons with matter occurs on a broad spectrum, ranging from high energy γ-rays to low energy regions in the infrared and beyond [8]. The five main interaction mechanisms are depicted in Figure 2.2 and the categorization depends on the respective photon energy-levels in the region between μeV and keV: [8, 27, 32]:

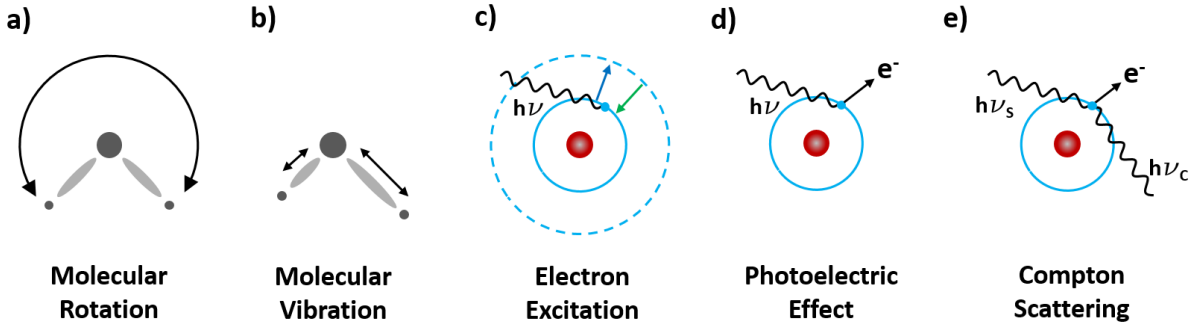

Figure 2.2: Light-matter interaction mechanisms.

a) Molecular Rotation: Photons with wavelengths at the microwave region have low energies ranging from μeV to meV. Photon absorption by a molecule then leads to an elevation in the molecule's quantized rotational energy state and the energy is dissipated to surrounding matter by friction, e.g. by rotational reorientation of a molecule substructure.

b) Molecular Vibration: In the infra-red region, photons exhibit energies from meV up to few eV and upon photon absorption, the energetic state of a molecule may be elevated via innate vibrational modes. Similar to molecular rotation, energy is then dissipated to surrounding matter by friction.

c) Electron Excitation: Photons in the visible range ($\sim$ 400-700 nm for the human eye), intersecting with the NIR ($\sim$ 700-1300 nm) and the UV region (100-400 nm), have energies in the order of eV and may transfer an atom's or molecule's electron to a higher excited stage upon absorption. Energy dissipation can then happen via radiative or non-radiative relaxation. Here, radiative de-excitation relates to energy dissipation by photo-luminescence, either by fluorescence or by phosphorescence, and is the foundation for fluorescence based imaging methods such as fluorescence microscopy. In the framework of optoacoustic imaging though, non-radiative de-excitation is the key mechanism for acoustic signal generation. In this process, the energy of the excited electron is transitioned into kinetic energy such as rotational motion of a molecule and thus converted into heat. In optoacoustic imaging, this process generates acoustic signals via thermoelastic expansion and represents the source of contrast in optoacoustic imaging (commonly referred to as "optical absorption contrast").

d) Photoelectric Effect (Ionization): In the UV region at wavelengths below 400 nm, photon energies range between eV and around 120 keV. At this energy level, the photoelectric effect is the predominant process where an electron is split off an atom or molecule upon photon absorption. As this ionizing process produces free radicals, it is not suitable for biomedical imaging in tissue.

e) Compton Scattering: For photon energies of above 120 keV and corresponding wavelengths below the UV region, Compton scattering applies. Here, the photon wavelength is increased as energy is effectively transmitted to an electron that is still bound to the atom or molecule. Similar to the ionizing energy levels of the photoelectric effect, photon energies in the keV regime and beyond are not relevant for optoacoustic imaging.

Excluding absorption methods with higher photon energies that are harmful for biological tissue, it is only photon absorption at energies in the range of eV that leads to non-radiative thermoelastic expansion and the subsequent generation of ultrasound waves in a given absorber (see Figure 2.1). Exemplarily, a photon energy of 2 eV [39] corresponds to an excitation wavelength of around 620 nm.

Light Absorption

A Jablonski-diagram illustrating the electron excitation upon photon absorption in the eV regime is shown in Figure 2.3. Upon photon absorption, electrons are lifted from

the energetic ground state S_0 to a higher vibrational energy level of the first excited singlet state S_1. Absorption occurs at a time scale of fs and the subsequent descent to the lowest vibrational energy level of S_1 occurs within ps. At this point, radiative (fluorescence and phosphorescence) or non-radiative relaxation may occur.

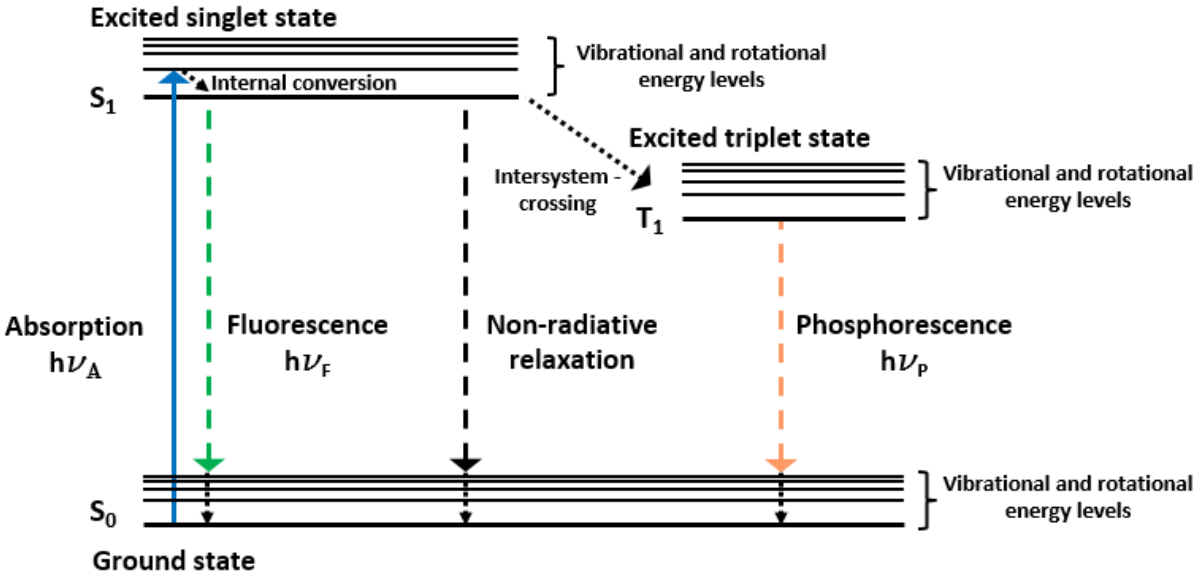

Figure 2.3: Jablonski-diagram for electron excitation: De-excitation occurs via radiative (fluorescence or phosphorescence) and non-radiative relaxation. $h\nu$ relates to the energy of the absorbed, fluorescent and phosphorescent photons, respectively (adapted from [8]).

In fluorescence, the excited state drops to a higher vibrational level of the ground state by the spontaneous emission of a photon within ns after absorption. Also at this state, the descent to the lowest vibrational energy level of S_0 occurs within ps. The emitted photons have a lower energy (at higher wavelength) than the absorbed photon due to energy conversion by non-radiative relaxation in the vibrational and rotational energy levels of S_1 and S_0. This difference in energy level is commonly known as the Stokes-shift [39].
In phosphorescence, the electron in S_1 undergoes inter-system crossing towards an excited triplet state T_1. The subsequent descent to the ground state is a forbidden transition in terms of quantum mechanics and leads to an extended life time of this state of ms up to s [8]. Eventually, the transition to S_0 occurs with the emission of a photon analogous to fluorescence. For the sake of this survey, triplet states, energy transitions such as internal conversion from excited singlet states S_2 to S_1 as well as virtual energy states (e.g. used in Raman-scattering) are not further discussed here.
The third process is non-radiative relaxation to the ground state and represents the

fundamental principle of the photoacoustic effect. In this non-radiative process, energy is dissipated via kinetic energy, leading to local heating and thermoelastic expansion (and contraction) which corresponds to the local generation of acoustic signals. Consequently, optoacoustic imaging is non-ionizing, has no inherent radiative energy dissipation and is purely based on optical absorption.

Absorption Spectra

The intensity of ultrasound signals generated by the photoacoustic effect is proportional to the foregone photon absorption. Hence, the illuminating light intensity as well as the absorption coefficient of the respective absorber are the governing factors for optoacoustic signal generation. For biological tissue, the optical fluence of the applied laser is governed by safety standards which is e.g. $100\frac{mJ}{cm^2}$ in the NIR (see subsection 8.1.2). While in non-biomedical applications such as in NDT, the threshold for the optical fluence is commonly higher than in biomedical applications, the maximum applied fluence is one of the main limiting factors in optoacoustic imaging. On the other hand, absorption coefficients of endogenous absorbers in tissue strongly correlate with the wavelengths of the applied excitation lasers. This principle allows to select certain excitation wavelengths for absorbers of interest in analogy to fluorescent imaging. The spectra from a selection of predominant endogenous absorbers in optoacoustic imaging are depicted in Figure 2.4. These absorption spectra are particularly important for optoacoustic imaging. For example, the high overall absorption of oxygenated (HbO_2) and deoxygenated hemoglobin (HHb) allows to image vasculature in tissue, which is one of the most popular implementations in optoacoustic imaging [40]. Additionally, the wavelength-dependent difference in absorption spectra of HbO_2 and HHb allows for targeted optoacoustic excitation and as a consequence for spectral differentiation of the recorded optoacoustic signals. The resulting ratio of HbO_2 and HHb can then be interpreted as a measure for blood oxygenation in tissue. The graph in Figure 2.4 also indicates a spectral range in the visible region from 400 nm to 700 nm for lipids and water where little light is absorbed. This region effectively enables optoacoustic imaging in tissue, which typically consists out of 80 % of water. It also allows optoacoustic imaging lipids in tissue, such as in subcutaneous fat layers. However, it is important to separate certain absorbers in tissue in order to interpret images correctly. Melanin for example has a continuously high absorption coefficient and in melanin-rich samples, such as zebrafish (see chapter 4), optoacoustic excitation with a single wavelength can lead to overlapping optoacoustic signals from both haemoglobin and melanin.

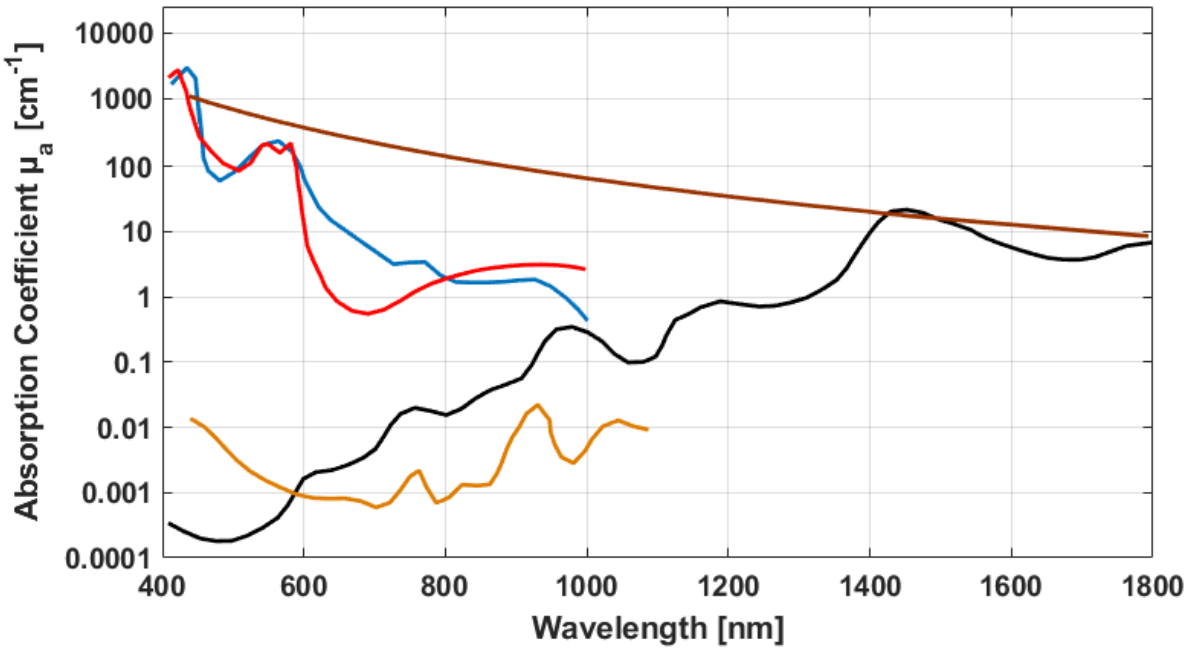

Figure 2.4: Absorption coefficient spectra for significant endogenous chromophores in tissue: Water (black), lipids (yellow), melanin (brown), oxyhaemoglobin (red) and deoxyhaemoglobin (blue). Spectra data from [40].

Moreover, exogenous chromophores can be applied as targeted sources of contrast. These chromophores are based e.g. on proteins or carbon structures and can be applied in tissue analogous to fluorescence microscopy. In the framework of multi-spectral optoacoustic tomography, dyes such as ICG have already been succesfully demonstrated [40]. Other exogenous contrast agents, such as carbon nano-structures, are a promising approach for creating customized absorbers [41]. However, the limited individual absorber size still limits the amount of absorbed photon energy, which eventually leads to weak overall optoacoustic signal intensities.

2.2.2 Photoacoustic Wave Equation

The key to optoacoustic imaging is to identify the geometry and composition of a sample by measuring the spatial and temporal information of optoacoustic signals. It is therefore vital to understand the formation and propagation of acoustic waves generated by the photoacoustic effect. When describing an acoustic wave in the framework of optoacoustic imaging, there are two relevant temporal conditions [28, 42]:

a) **Thermal confinement:** An optoacoustic signal can only be generated locally and

therefore spatially distinguished, when the pulse duration of the excitation laser is shorter than the thermal relaxation time. Here, τ_{th} specifies the time duration of the heat inside a given voxel (ideally assumed to be a spherically symmetric volume that is excited via photon absorption) to disperse into the surroundings. τ_{th} is given by

$$\tau_{th} = \frac{d_V^2}{D_{th}} \tag{2.1}$$

where d_V is the voxel diameter and D_{th} is the thermal diffusivity in the medium.

b) **Stress confinement:** If the duration of the excitation laser pulse is shorter than the stress relaxation time τ_S, then pressure rises throughout the medium during excitation are negligible. Here, τ_S is given by

$$\tau_S = \frac{d_V}{v_s} \tag{2.2}$$

where v_s is the speed of sound in the respective medium.

As will be discussed later, typical resolutions in optoacoustic tomography are around 50 μm, corresponding to τ_S of around 30 ns. Therefore, τ_S is the governing factor when deciding upon the excitation laser and pulse durations ranging from hundreds of ps to a few ns are commonly selected for optoacoustic signal generation (see chapter 4).
The wave equation for a propagating acoustic wave $p(\vec{r}, t)$ that suffices the assumption of thermal confinement as well as the assumption of stress confinement can be derived from the equation of motion and the generalized Hooke's law. It is then given by [42]:

$$\left(\nabla^2 - \frac{1}{c^2}\frac{\partial^2}{\partial t^2}\right) p(\vec{r}, t) = -\frac{\Gamma}{c^2}\frac{\partial}{\partial t} H(\vec{r}, t) \tag{2.3}$$

Here, the heating effect on the volume of a material is given by the dimensionless Grueneisen-parameter Γ

$$\Gamma = \frac{\beta v_s^2}{C_p} \tag{2.4}$$

with β constituting the isobaric heat expansion coefficient and C_p the isobaric heat capacity of the absorber, respectively. An exemplary derivation of the optoacoustic pressure generated in a given sample in dependence of the Grüneisen parameter is described in the Appendix (subsection 8.1.2) and a typical value for Γ is 0.2 in soft tissue [43]. Next, $H(\vec{r}, t)$ is the heating function describing energy absorption over time

in a given voxel depending on the energy of the absorbed photons (or that of absorbed electromagnetic radiation in general). It is given by

$$H(\vec{r},t) = \nu\mu(\vec{r})\Phi(\vec{r},t) \tag{2.5}$$

where ν is the heat conversion efficiency commonly approximated as $\nu \sim 1$ and $\Phi(\vec{r},t)$ is the optical fluence rate. Here, $\Phi(\vec{r},t)$ is not to be mixed with the optical fluence (see Appendix 8.1.2) and corresponds to the temporal derivative of the laser excitation intensity:

$$\frac{\partial}{\partial t}\Phi(\vec{r},t) = I(\vec{r},t) \tag{2.6}$$

Equation 2.3 allows a relevant observation [27]: Since the temporal derivative of $H(\vec{r},t)$ governs the right term of the equation, optoacoustic excitation can only occur when temporally differentiable illumination is applied, such as pulsed or modulated lasers. In the framework of this thesis, optoacoustic excitation is performed by pulsed laser light only. Excitation by modulated light might enable the application of light excitation that is less cost-intensive than pulsed lasers, such as LEDs. Optoacoustics by light modulation is a rather novel research field and has been extensively discussed in [44].
The right term of equation 2.3 describes the generation of optoacoustic signals while the left term describes the propagation of an acoustic wave through a medium.
A solution for equation 2.3 can be received by finding the corresponding Green function and assuming local stress confinement as well as a local energy absorption in the form of the delta function $H(t) = \delta(t)$. The pressure field in infinite space can then be written as [42, 45]:

$$p(\vec{r},t) = \frac{\Gamma}{4\pi v_s^2}\frac{\partial}{\partial t}\left[\frac{1}{v_s t}\int_V H(\vec{r'})\ \delta\left(t - \frac{\left|\vec{r} - \vec{r'}\right|}{v_s}\right) d\vec{r'}\right] \tag{2.7}$$

Here, the heating function is integrated over the illuminated volume and $\vec{r'}$ lies within this volume. The solution for a spherical absorber at $\vec{r_s}$ with radius a is then [28, 29]:

$$p(\vec{r},t) = p_I\left[U\left(a - v_s t - R\right) + \frac{R - v_s t}{2R}U\left(R - |a - v_s t|\right)U\left(a + v_s t - R\right)\right] \tag{2.8}$$

Here, p_I is the initial pressure amplitude, U is the Heaviside function (defined as $H(x) = 0$ for $x < 0$ and $H(x) = 1$ for $x \geqq 0$) and R is the distance between the detector and the acoustic source with $R = \left|\vec{r} - \vec{r'}\right|$. Additionally, the absorber has a finite volume and is

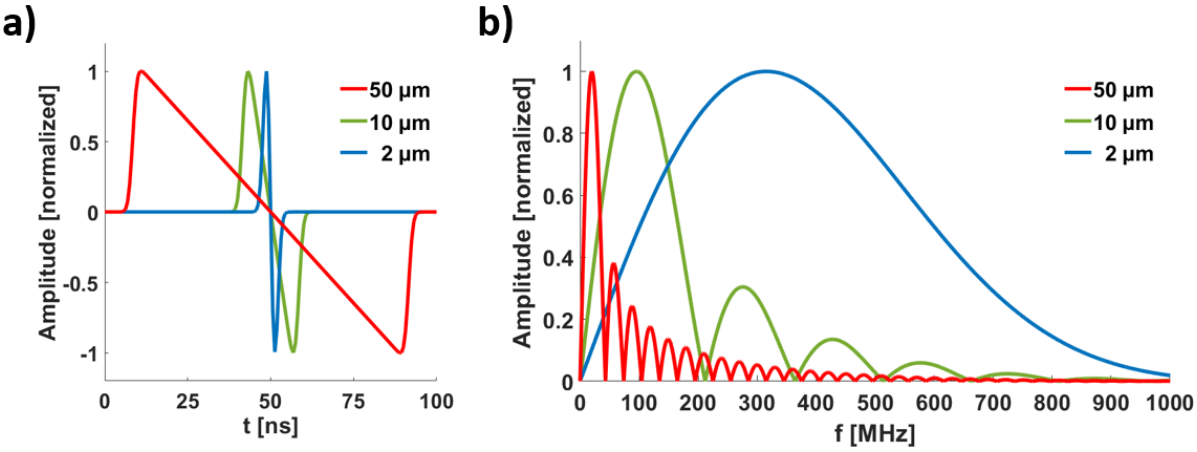

Figure 2.5: Simulated optoacoustic signals for differently sized spherical absorbers: (a) Normalized optoacoustic signals for spheres with 2 μm, 10 μm and 50 μm diameters, typical for absorber sizes in optoacoustic microscopy and tomography, respectively. (b) Corresponding frequency spectra exemplifying application-dependent bandwidth requirements for applied ultrasound detectors. Inspired by [42, 46].

assumed to have a homogeneous composition throughout its volume.

Ideal Optoacoustic Signals

Equation 2.8 is the basis for simulating optoacoustic signals and the corresponding time domain signals recorded at a virtual ultrasound detector at point $\vec{r}$ are shown in Figure 2.5a. The signals represent a bipolar N-shape which is characteristic for longitudinal waves propagating through a fluid medium where signal duration decreases with diminishing sphere diameters. For this example, ideal absorbing spheres with radii of 2 μm and 10 μm were modelled, corresponding to absorbers typically examined in optoacoustic microscopy. The sphere with a 50 μm radius corresponds to a bigger absorber as found e.g. in an prevalent optoacoustic tomography application. Note that in this simulation the acoustic amplitudes were normalized for the sake of demonstration and that for an equal fluence, the respective amplitudes would diminish correlating to the absorber diameter. Moreover, the spheres were assumed to be fluid, allowing to disregard resilient forces inside the absorber. In order to integrate the effect of the finite duration of the optoacoustic excitation (from a pulsed laser source), the time domain signals are convolved with a Gaussian function with a FWHM of 1 ns.
The corresponding frequency content of the modelled absorbers depicted in Figure 2.5b is obtained by applying a fast Fourier transformation to the respective time domain signals. The frequency content is assembled in a number of lobes with a successively

decreasing amplitude and as expected, the central frequency is inversely proportional to the absorber diameter. The point of the highest frequency content of an absorber is commonly referred to as the central frequency and can be estimated via [47]

$$f_C \approx 0.8\frac{v_s}{2a} \tag{2.9}$$

where v_s is the speed of sound in the absorber and a denotes the absorber radius. The full bandwidth of acoustic signals emitted by an optoacoustic source is derived as the FWHM of the lobe, generally of the prominent first lobe in the respective frequency spectrum.

It is particularly important to consider the estimated frequency content of target absorbers when choosing appropriate ultrasound detectors, in order to match the detectors frequency response to the central frequency of the ultrasound source. As Figure 2.5 indicates, a given transducer might be optimized to be sensitive towards ultrasound emitted by micron-sized absorbers in optoacoustic imaging, with a central frequency of hundreds of MHz. On the other hand, this very transducer would then lack sensitivity when applied in optoacoustic tomography, where the frequency content of acoustic signals does not exceed the range of tens of MHz. Note that the frequency content close to the absorbers in optoacoustic tomography is as broad as in microscopic applications, but that the attenuation of acoustic signals is frequency dependent with higher frequencies becoming lost over small distances (see chapter 3 for more details).

2.3 Optoacoustic Imaging Modalities

In order to utilize the photoacoustic effect for biomedical imaging, it is not sufficient to simply record the generated ultrasound signals in an arbitrary manner. In fact, the way that ultrasound signals are recorded and worked on, is a defining prerequisite for the various optoacoustic imaging modalities and their corresponding applications. In the following subsections, the three branches of optoacoustic imaging - tomography, microscopy and endoscopy - will be discussed, including the respective imaging and setup geometries, the acoustic detector characteristics as well as the data processing and image reconstruction techniques. For the sake of a clearly arranged survey, optoacoustic microscopy and endoscopy are discussed separately, although both modalities do overlap in terms of image acquisition and reconstruction.

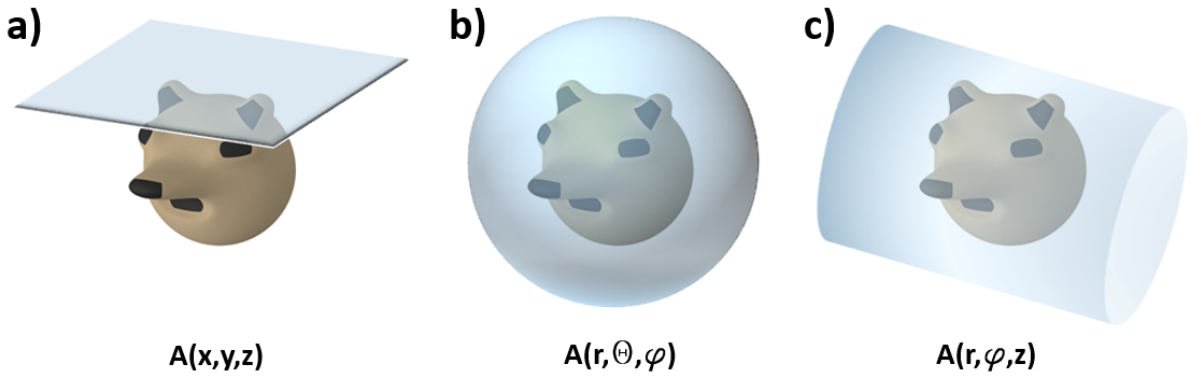

Figure 2.6: Ideal detector conceptions for optoacoustic tomography: Detector scanning perpendicularly to and across (a) an infinitely wide plane, (b) a sphere and (c) an infinitely long cylinder. In the former case, the plane is located atop a given sample and in the two latter cases the samples are enclosed in the respective volumes (adapted from [49]).

2.3.1 Optoacoustic Tomography

Tomographic techniques in general, including X-ray CT, MRI as well as optoacoustic tomography, are based on mathematical algorithms that enable computer-based image reconstruction [42].

In optoacoustic tomography, one of the most common techniques for image reconstruction is the back-projection method. Here, a single detector or a detector array is moved relative to a geometrically advantageous surface across a given sample as depicted in Figure 2.6. For each point of the scan, time-domain signals are then recorded along with the respective detector position. For image reconstruction, the recorded data is time-reversed and back-projected onto a geometrical frame that conforms with the scanning geometry of the detector. The time-domain signals are then summed up within that volume, yielding a 3D map of the optoacoustic sources in the sample. An ideal scenario of a spherical scanning geometry has a point-like ultrasound detector with an omni-directional sensitivity field where the detector is moved along an unlimited number of scan positions across the surface of the sphere. Assuming such an ideal geometrical frame, which is analogously adaptable for an infinite plane or an infinite cylinder, the back-projection algorithm yields an exact reproduction of the absorber distribution within the measured volume [48].

Mathematically, the back-projection algorithm is derived as a solution of the optoacoustic wave equation 2.3. In the case of a spherical detection geometry and when postulating stress and thermal confinement, it describes the absorber distribution as [48]

$$A(r,\theta,\varphi) = -\frac{1}{2\pi v_s^2 \Gamma} \int\int_{S_0} dS_0 \frac{1}{t} \frac{\partial p(\vec{r_0},t)}{\partial t}\bigg|_{t=\frac{|\vec{r_0}-\vec{r}|}{v_s}} \tag{2.10}$$

with

$$dS_0 = r_0^2 \sin\theta_0 d\theta_0 d\varphi_0 \tag{2.11}$$

as elements of the spherical detector surface S_0. Here, the detector measures the acoustic signals originating at $\vec{r}$ at position $\vec{r_0}$. The equation shows that the complete absorption distribution can be calculated in time domain based on the quantity $-\frac{1}{t}\frac{\partial p(\vec{r_0},t)}{\partial t}$. This conclusion also applies to absorption distributions in planar ($A(x,y,z)$) and cylindrical ($A(r,\varphi,z)$) scanning geometries. An ample derivation of equation 2.10 as well as immersed discussions for planar and cylindrical detection geometries are found in [45, 49, 50].
For the context of this work, it is important to point out the implications of this approach for the development of optical ultrasound detectors: When aspiring towards close-to-ideal tomographic imaging, both miniaturization of detector size as well as maximation of detection bandwidth are desirable.
A number of alternative reconstruction methods exist that amend or substitute back-projection algorithms. One of the relevant alternatives is the so called model-based method that allows the integration of given experimental factors, such as of individual detector responses. As all reconstruction methods have identical requirements for ideal detection geometries and sensor specifications, these approaches are not discussed in further detail here. Relevant literature can be found e.g. in [39, 51, 52].

Spatial Resolution

The spatial resolution of an optoacoustic imaging setup is divided into two components: axial and lateral resolution. In an optoacoustic tomography setup, the applied detection geometry defines the respective resolution notations. In this work, a simplified circular geometry is chosen as depicted in Figure 2.7. It describes a representative 2D setup, where an ultrasound detector of diameter D is rotated around a given sample in the distance r_0. The scan is performed by incremental steps of θ and the acoustic signals from absorbers, which are positioned at r_n inside the volume, are recorded for each step. The sample is acoustically matched to the ultrasound detector or a detector array by a coupling medium and the speed of sound is assumed to be constant throughout the enclosed volume. Note that for the sake of clarity, the laser excitation is not depicted in the illustration.

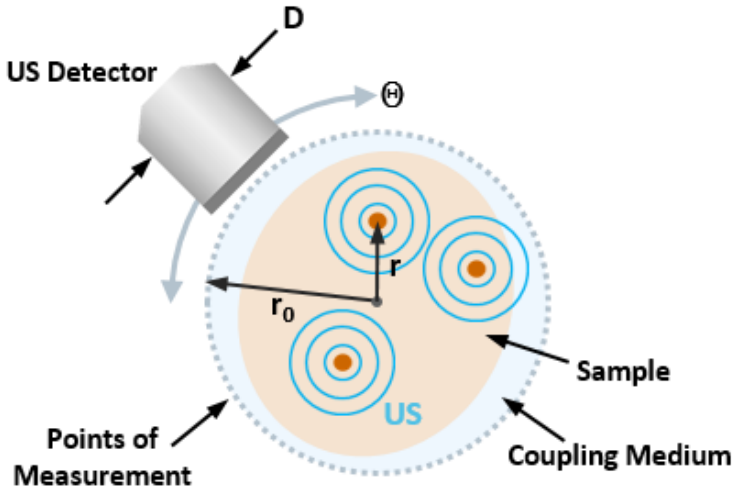

Figure 2.7: Common geometry for optoacoustic tomography: An ultrasound detector with a sensor diameter D detects optoacoustic signals from a sample in a circular scan with incremental steps in θ. The distance between the geometrical center of the circle and an absorber within the sample is r_0 and its radius is r. The sample is embedded in an acoustic coupling medium and uniformly irradiated by an excitation laser (not illustrated).

The axial resolution is spatially invariant and, e.g. in the circular 2D geometry, defined as the resolution along the axis between the detector and the geometrical center of the arrangement. At a sampling rate that is much higher than the upper limit of the frequency response of the ultrasound detector and when assuming the detector to be an ideal point detector, the axial resolution is [15]

$$a \approx 0.6\,\lambda_{CO} = 0.6\frac{v_S}{f_{CO}} \tag{2.12}$$

where λ_{CO} is the acoustic wavelength corresponding to the upper detector cut-off frequency f_{CO} at -6 dB and v_S is the speed of sound in the respective sample. For sufficiently small detectors, this approximation is applied to characterize the highest achievable axial resolution in any type of optoacoustic tomography system.

For the lateral resolution on the other hand, the finite size of point-detectors is relevant, as the achievable resolution decreases proportionally to the sensor aperture via [28]

$$R_{AP}(r) = \frac{r}{r_0}\,D \tag{2.13}$$

where D denotes e.g. the sensor diameter of a piezoelectric detector as shown in Figure 2.7, r_0 the radius of the circular scan and r the distance between the absorber

and the geometrical center of the scan. The lateral resolution of the illustrated detection geometry is then given by [15]

$$R_{LAT}(r) = \sqrt{a^2 + R_{AP}(r)^2} \tag{2.14}$$

Here, R_{AP} usually is the governing term when characterizing tomography setups based on piezoelectric detectors and with it the diameter of ultrasound sensors. An approach to improve the lateral resolution is to apply acoustically focused ultrasound sensors, mostly cylindrically or curved piezoelectric elements as well as sensors equipped with an acoustic lens [45, 50]. By utilizing an acoustic focus, the overall sensitivity of a sensor is translated to a smaller sensing area, thus amplifying its sensitivity towards acoustic signals. In fact, the sensing volume corresponds to an ellipsoid with the length and diameter depending on the wavelength of the acoustic signals. This ellipsoidal volume is the drawback of this approach, as there is an inherent trade-off when simultaneously addressing spatial resolution and achievable imaging depth: when improving the numerical aperture (**NA**) of the focusing element, the resolution increases but the imaging depth decreases, impeding the design of tomographic systems with equal resolution over the full field of view (**FOV**). Aspects related to focused ultrasound detectors are discussed in more detail in [11] and [39].

Discussion

The application of optical ultrasound detectors in optoacoustic tomography has a number of advantages that are related to an improved spatial resolution as well as to an increased imaging speed. Naturally, the goal is to create close-to-ideal detectors and setup geometries with the three relevant aspects being the sensor size, the bandwidth and the detection geometry. The latter includes the sensor density (or spatial sampling rate) and the total amount of sensors recording optoacoustic signals. As discussed in section 2.3.1, the spatial resolution depends on the bandwidth and the size of the applied ultrasound sensor. With resonator based optical detectors as well as with free-beam refractometric detectors, the bandwidth of piezoelectric and CMUT based ultrasound transducers has been already surpassed [17]. While there are piezoelectric transducers with central frequencies of more than a GHz [16, 53], such transducers have only been applied in transmission mode optoacoustic microscopy yet, as these are focused transducers that have small working distances in the sub-millimetre range. Also in terms of detector size, optical ultrasound detectors may be designed and fabricated with much smaller footprints

than piezoelectric elements (see chapter 3), allowing for an improved overall resolution as seen in Equation 2.14. While focused ultrasound transducers can compensate for size deficits by smaller virtual detection volumes, the actual sensor size remains the same. This eliminates the possibility to create detector arrays with high and ultra-high densities, as would be necessary for fast image acquisition and advanced applications such as 2D arrays of ultrasound sensors, effectively yielding an acoustic camera.
An alternative all-optical method for optoacoustic tomography is discussed and illustrated in more detail in subsection 3.4.1 and Figure 3.7, respectively [54]. Here, acoustically induced changes in a collimated interrogation beam can be either visualized on a screen for 2D image acquisition or monitored by a fast CCD for 3D image acquisition. In future, this approach could allow for simplified tomographic imaging without the need for computational image reconstruction.

2.3.2 Optoacoustic Microscopy

Optoacoustic microscopy is divided into acoustic resolution (**AR-OAM**) and optical resolution optoacoustic microscopy (**OR-OAM**). AR-OAM utilizes focused ultrasound detectors and an unfocused light source for optoacoustic excitation. Due to weak scattering of acoustic waves in tissue, imaging depths of up to 3 mm with lateral resolutions of 45 μm can be achieved [13]. For detectors with 1.2 Ghz central frequency, resolutions of up to 5 μm have been shown, albeit at penetration depths of around 30 μm [53]. Similar to optoacoustic tomography, the axial resolution is governed by the bandwidth of the acoustic detector. While AR-OAM resolutions do not exceed those of advanced tomographic setups which achieve higher imaging depths in the cm scale [30], the modality has the big advantage of simplicity: imaging with fairly high resolutions can be performed without the need for complex scanning geometries and computationally intensive reconstruction algorithms but is a mere 2D projection of the measured acoustic signal peaks. Additionally, the excitation laser does not rely on a sophisticated method for light delivery but a simple diffuse illumination of the sample to facilitate equal fluence throughout the interrogated volume. On the other hand, AR-OAM is inherently limited by the low bandwidth of the commonly applied piezoelectric sensors. For a 400 MHz central frequency, a penetration depth of only 100 μm is achieved, without even considering increased distances due to an applied coupling medium [55]. However, the detector geometry is very similar to the one depicted in Figure 2.6a, where an ultrasound detector is scanned across a plane atop the sample in a raster pattern. Consequently, AR-OAM can be combined with tomographic imaging of the same sample when increasing

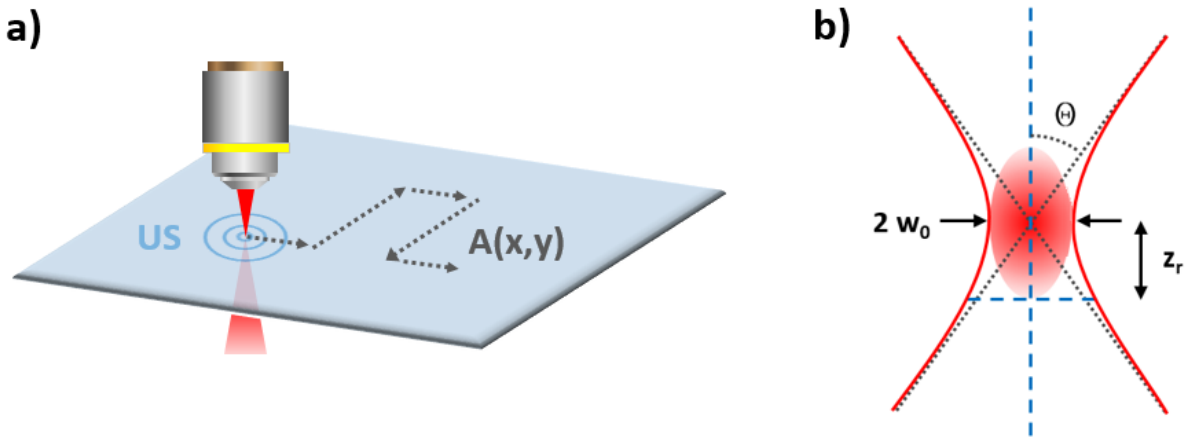

Figure 2.8: Optical resolution optoacoustic microscopy: (a) The optical focus is raster-scanned through a sample across the focal plane. (b) Illustration of a refraction limited focal spot with the radius of the beam waist w_0 and the Rayleigh length z_r.

the detector distance z relative to the actual image plane and positioning the detector out of focus. This hybrid imaging method has been demonstrated and introduced as optoacoustic mesoscopy [46].

In summary, AR-OAM is an attractive imaging modality e.g. in the area of non-destructive testing [17], but due to limited resolutions and penetration depths, it is not a widely used method in biomedical imaging. Moreover, the application of optical ultrasound sensors in AR-OAM would demand for the development of acoustically focused optical sensors, which seems unjustified as of the limited achievable outcome.

OR-OAM pursues the inverse setting to AR-OAM: While the ultrasound detector may be of an unfocused nature, it is a highly focused optical beam that excites a confined volume in a given sample. Hence, the focusing characteristics of the applied optics, such as the magnification, numerical aperture and the working distance, define the lateral resolution. For high-NA objectives, lateral resolutions of 0.5 μm have been demonstrated [56, 57], albeit at depths below 100 μm. As OR-OAM aims at label free microscopic imaging at the cellular and sub-cellular level, such low imaging depths are acceptable given the high lateral resolution and even exceed the depths reached by purely optical microscopy [2, 31].

The typical geometry of OR-OAM is illustrated in Figure 2.8. Here, an optical excitation beam is tightly focused by a microscope objective and the sample is moved in a raster pattern across the ROI in the focal plane. Similar to AR-OAM, time resolved acoustic signals (A-line scans) are recorded for each point in the scanned sample plane and plotted as maximum amplitude (**MAP**) or maximum intensity projections (**MIP**).

Commonly, either the objective or the sample are adjusted along the z axis for precise alignment. While photons undergo scattering within the sample, the emitted acoustic waves undergo a frequency dependent attenuation, but are hardly scattered (see chapter 3) [58]. Consequently, imaging depths have been pushed up to 1 mm by performing e.g. multi-photon excitation [2]. The imaging speeds of both AR-OAM and OR-OAM are limited by the scanning speed of the applied translational stages, the repetition rate of the pulsed excitation laser as well as by the signal processing bandwidth. A way to circumvent the limitation by mechanical scanning speeds of inert translational stages is to scan a given sample by galvanometric mirrors as shown in chapter 4.

Spatial Resolution

Analogous to optoacoustic tomography, axial and lateral resolution need to be discussed separately in optoacoustic microscopy. Here, the lateral resolution of AR-OAM depends on the acoustic wavelength λ_0, the aperture D and the focal distance l of the detector [9]. It can be written as

$$R_{(AR)_{lat}} = 0.71\ \lambda_0 \frac{2\,l}{D} \tag{2.15}$$

In contrast, the principle of optical focusing for OR-OAM is illustrated in Figure 2.8b. Here, it is the beam waist of the optical focus that defines the resolution. For a diffraction limited focusing setup and a Gaussian beam, the divergence angle in the far-field is given by [59]

$$\theta = \frac{\lambda}{\pi\ w_0} \tag{2.16}$$

where λ is the wavelength of the excitation laser and $2\,w_0$ corresponds to the beam waist and thus to the optical resolution. w_0 can then be expressed as

$$w_0 = \frac{2\,f\,\lambda}{\pi\,d} \tag{2.17}$$

where d represents the beam diameter that is incident on the focusing lens or objective [27]. The corresponding lateral resolution in an OR-OAM setup follows in the form of [9]

$$R_{(OR)_{lat}} = 0.5\ \frac{\lambda}{NA} \tag{2.18}$$

where the NA is the numerical aperture of the applied lens or microscope objective. Interestingly, equations 2.15 and 2.18 differ only in the prefactor. This lies in the different origin of the equations: while AR-OAM is based on the amplitude of the acoustic signals, OR-OAM depends on the intensity of the optical illumination [9].
Especially when applying high frequency ultrasound sensors and optics with a low NA in an OR-OAM setup, it is reasonable to consider the Rayleigh length of the optical focus. The Rayleigh length Z_R is depicted in Figure 2.8b and is defined as the distance between the optical focus and the beam radius at $\sqrt{2}\,\omega_0$ along the optical axis [59].

$$Z_R = \frac{\pi\ w_0^2}{\lambda} \tag{2.19}$$

Accordingly, $2\,Z_R$ corresponds to the depth-of-focus and can be regarded as a limitation

to the axial resolution of OR-OAM [27]. Hence, the NA of the focusing optics should be chosen in a way as to guarantee a depth-of-focus that is smaller than the axial resolution of the system.
The axial resolutions for AR-OAM and OR-OAM are both given by [31]

$$R_{(AR/OR)_{ax}} = 0.88\,\frac{v_S}{f_A} \tag{2.20}$$

where f_A corresponds to the signal bandwidth and is commonly approximated by the detection bandwidth of the ultrasound detector. Note that the tompgraphic axial resolution in Equation 2.14 and the OAM axial resolution in Equation 2.20 are related, but that values vary for OAM in the literature [31, 55]. Throughout this work, the pre factor 0.88 in Equation 2.20 is applied when characterising microscopy images.

Discussion

In general, optoacoustic microscopy applies AR-OAM methods when addressing absorbers at depths in the mm range and OR-OAM when aiming at diffraction limited resolution in depths of a mm and below. Another important aspect when creating an OAM setup is to consider the location of the ultrasound detector. Note that in Figure 2.8, no acoustic detector is depicted. The reason for this is to avoid confusion, as ultrasound detection can be performed from the illumination side (epitaxial-/**epi-illumination** or **reflection-mode** microscopy) or from the adverse direction of the sample (**transmission-mode** microscopy). Transmission-mode geometries have the advantage that highly sensitive focused piezoelectric sensors can be employed. Here, the optical excitation and the acoustic detection volume are aligned confocally [46, 60]. In contrast, reflection-mode microscopy has the vital aspect that thick samples, such as *in vivo* skin, can be imaged without the need for excision. This makes reflection-mode detection geometries sought-after, as the simultaneous excitation of and the read-out in close proximity to a given micron-sized volume is very challenging. Nevertheless, only focused piezoelectric sensor designs reach sensitivities exceeding 10 Pa and successful approaches with piezoelectric sensors in reflection-mode setups utilise either acoustic deflectors that are optically transparent or sensors that have an embedded aperture for light delivery [31]. Rathermore, it is optical detection of ultrasound that lately allowed the creation of advanced multi-modal epi-illumination microscopes [17, 60]. These methods rely on unfocused ultrasound detection, including methods such as the deflection of tightly focused light beams as well as miniaturized optical resonators that can be installed in close proximity to the acoustic

source. These and other methods are discussed in more detail in chapter 3.

2.3.3 Optoacoustic Endoscopy

Optoacoustic endoscopy has major overlaps with optoacoustic microscopy in terms of detection geometries and image reconstruction. In particular, light delivery and ultrasound detection have the same underlying principles, with image formation based on optical and acoustic resolution. Consequently, the achievable spatial resolution of a given optoacoustic endoscope is governed by equations 2.15, 2.18 and 2.20, for AR and OR resolutions, respectively.

The general principle of optoacoustic endoscopy is illustrated in Figure 2.9 and is divided into two areas: Forward-looking and side-looking endoscopes.

Forward-looking geometries can be implemented with an optical fiber for light delivery and a second fiber with an embedded optical ultrasound detector for forward looking ultrasound detection (see chapter 6). Alternatively, these tasks might be combined into a single fiber with double cladding, where the fiber core constitutes an optical resonator or arm of a fiber interferometer (see chapter 3) and the excitation light is delivered into the sample through the first fiber cladding. This design is particularly useful to examine the quality and extent of occlusions along the lumen axis, e.g. in coronary arteries [61]. Note that this principle provides a single A-scan with distance and absorption informations of the occlusion rather than an actual image. This aspect also applies, when a grin lens is attached to the fiber facet, resulting in either focused or re-collimated excitation light. Here, grin lenses are used to re-collimate the light at the output of an optical fiber and are therefore predestinated for the use in forward-looking endoscopy.

Side-looking geometries utilize an angled fiber tip, prism or mirror to reflect the excitation laser perpendicular to the fiber axis. Ultrasound detection can then be performed with e.g. a fiber based detector [62] that is located on frame with the illumination fiber. Commonly, a grin lens in front of the reflecting element allows for OR and the ultrasound detector is directed towards the optical focus. Image formation is then performed by helicoidal scanning along the z-axis or by step-by-step circular scans around the fiber axis, if the mechanics do not allow a free rotation of the sensor. The possibility of optical focusing with a GRIN lense is not depicted in Figure 2.9. For every measured point in time, an A-scan is recorded and projected onto a cylindrical surface as respective MIP. Side-looking geometries allow to examine e.g. the vessel wall as well as the control of stent placements [18].

In both approaches, optical fibers are the foundation for light delivery. OR endoscopes

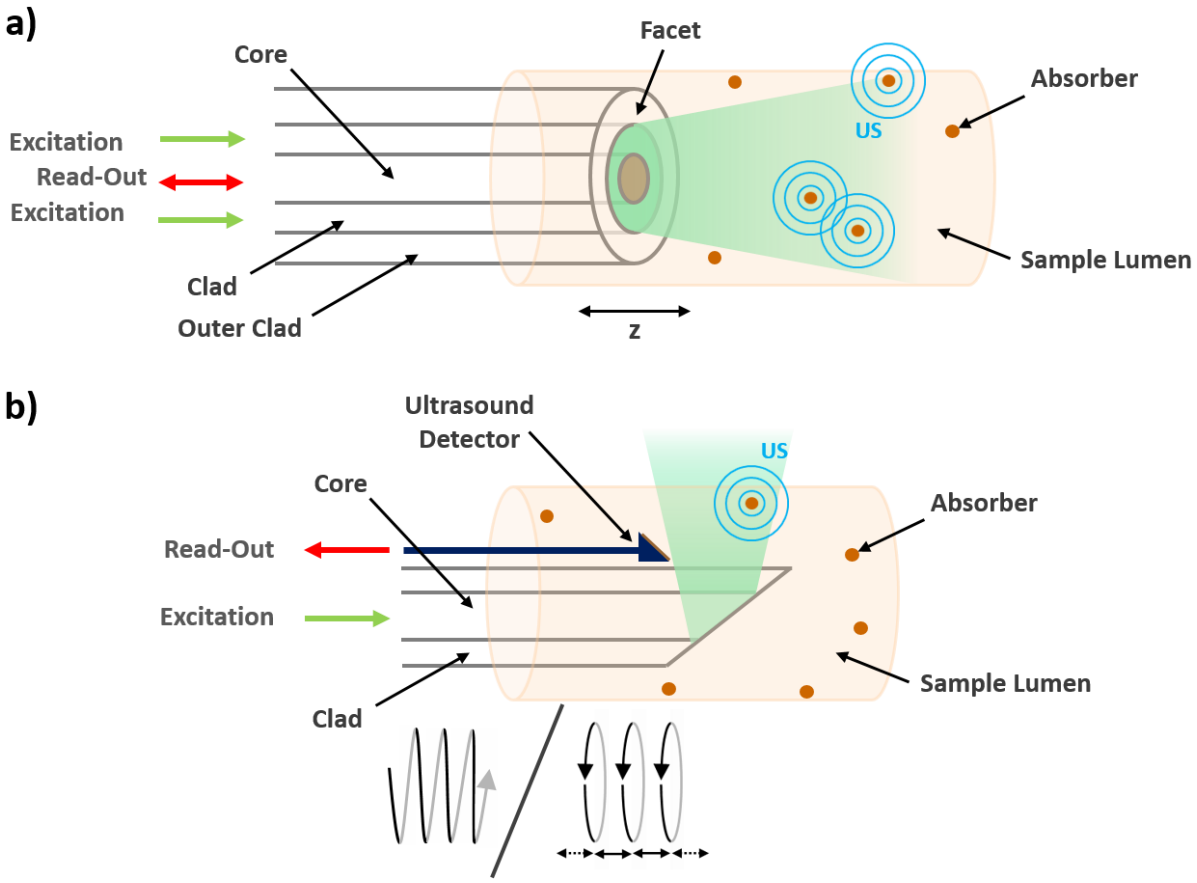

Figure 2.9: Common working principles for optoacoustic endoscopy: (a) Forward-looking orientation: A double-clad fiber delivers light for optoacoustic signal excitation in the outer cladding and houses an interferometric ultrasound detector in the core. (b) Side-looking orientation: Excitation light is reflected perpendicular to the fiber axis and ultrasound detection is performed by a sensor on frame with the illumination fiber. Side-looking geometry allows to perform continuous helicoidal scans or step-by-step 360° scans.

commonly rely on fibers with core diameters of few μm that allows for either single or few mode propagation of the excitation light depending on the respective wavelength. Moreover, the excitation light needs to be focused into the sample, which is commonly performed by a GRIN lens. In AR on the other hand, multi-mode fibers with cores in the range of hundreds of μm are utilized, allowing for optical excitation with higher pulse energies in the sample.

Discussion

An example for hybrid AR and OR imaging was illustrated in the introduction (see subsection 1.2.2), where the experiment was based on a hybrid AR and OR sensor head for gastrointestinal endoscopy [19]. The AR of about 250 μm was achieved at a depth of 1.5 mm with a 20 MHz piezoeletric ultrasound detector. In contrast, the OR of about 13 μm was achieved at around 800 μm and optical focusing was performed by a GRIN lens attached to the facet of the illumination fiber combined with a 90° micro-prism. The advantage of the hybrid approach can be seen in Figure 1.5, where high-resolution and in-depth imaging complement each other. While in gastro-endoscopy the detector size allows for relatively big sensor heads and multi-modal imaging approaches, e.g. intravascular imaging requires detectors with diameters in the scale of 1 mm and resolutions only available by OR designs. Hence, the application of piezoelectric transducers is rather limited and e.g. fiber based optical ultrasound detectors are currently a highly promising alternative approach. An exception to this limitation are unfocused ultrasound transducers (IVUS) for the determination of vessel diameters and other coarse physiological vessel properties [18]. One of the big advantages of all-optical fiber based optoacoustic endoscopy could be its seamless integration with other imaging modalities in the future, such as fluorescence imaging and OCT [63].

3 Review on Ultrasound Detectors

The detection of acoustic signals in biomedical imaging and sensing is commonly performed by piezoelectric materials, micro-machined devices or by optical means, such as refractometric or interferometric principles. In the following chapter, we review and compare a broad selection of such methods for the optical detection of ultrasound and conclude, why optical detectors might presently be the most promising technology for the application in optoacoustic imaging. Particular emphasis is put on the discussion of resonator based detectors and its read-out methods, which are crucial in regard to miniaturized applications as discussed in the motivation for this work (see 1.2).
Findings presented in this chapter and the underlying technological survey were published as review article in [17].

3.1 Introduction

Optoacoustic imaging demands more sophisticated ultrasound detectors than classic ultrasonography. In contrast to ultrasonography, acoustic signals are generated deep within a given sample such as tissue and especially optoacoustic signals with a high frequency content undergo enhanced acoustic attenuation. Additionally, tomographic reconstruction methods require detectors with wide opening angles and small overall dimensions in order to enable dense arrays of ultrasound detectors (see subsection 2.3.1). The most relevant specifications of ultrasound detectors as they relate to optoacoustic sensing and imaging are:

a) **Sensitivity:** The generation of optoacoustic signals is limited by the maximum employable optical fluence. Hence, ultrasound detectors should display sensitivities ranging from the sub-Pascal to Pascal range [64]. In ultrasonography, a typical acoustic signal reflected from an organ/tissue interface has a pressure magnitude of around 200 kPa [4]. In biomedical optoacoustic imaging, the theoretically highest achievable optoacoustic signal would be generated with the maximum applicable laser fluence for tissue, resulting in a pressure magnitude of around 0.8 kPa (see

appendix). Commonly, detector sensitivity is constituted via its noise level and is given as noise-equivalent pressure (**NEP**). In order to ease the comparison between various detector designs and technologies, detector sensitivity is often related to the bandwidth by: $\left[\frac{mPa}{\sqrt{Hz}}\right]$.

b) **Bandwidth and Central Frequency:** These two parameters are critical for both image resolution as well as for the size range of optical absorbers and structures that can be detected in tissue. In order to simultaneously detect signals originating from absorbers ranging from hundreds of microns to sub-micron in scale, ultrasound detectors need to display broad bandwidths as well as high central frequencies. For example, when resolving a perfect optical absorber of 100 μm diameter, a frequency response of 15 MHz is required. At the same time, an absorber of 1 μm diameter would already require a frequency response of up to 1.5 GHz.

c) **Detector Size:** Although often neglected when comparing performance parameters of acoustic sensing elements, the actual detector size is crucial. For example, the piezoelectric elements demonstrated for cardiovascular ultrasonography in chapter 1.2.1 had a cylindrical shape with diameters of around 0.8 mm (40 MHz central frequency) and 1.2 mm (15 MHz central frequency), respectively. The backing material, the electrically insulating sheath as well as the electrical wiring and connectorization additionally add up to the overall sensor dimensions. In contrast, e.g. an optical fiber-based ultrasound detector with superior sensing performance has been demonstrated with an effective size of 0.25 x 0.27 mm (see phase-shifted fiber Bragg gratings in chapter 4). When comparing e.g. piezoelectric to resonator based optical detectors, it is advantageous to relate detector sensitivity to detector size by: $\left[\frac{mPa\ mm^2}{\sqrt{Hz}}\right]$.

d) **Detector Aperture:** Depending on the underlying technology as well as on the geometry of a sensing element, its detector aperture (or acceptance angle) may enable or limit its use for specific applications. In the case of optoacoustic microscopy for example, image resolution is often determined by the optical resolution or rather by the focal diameter of the excitation beam. Here, the detector aperture may comprise only a few degrees, as long as it is aligned to the optoacoustic signal origin. On the other hand, optoacoustic tomography and mesoscopy require signal detection with a wide aperture so as to amount to a high number of projections of signal origins. The latter is essential for precise image reconstruction and can improve image acquisition time. In the case of optical ultrasound detectors, fiber-based sensors have been demonstrated with an axially symmetric acceptance angle (see chapter 4), which

is ideal for endoscopic applications. As another type of optical ultrasound detectors, optical micro-ring resonators possess cone-shaped acceptance angles of up to 30 °, which is suitable for tomographic applications [65].

e) **Total Impulse Response:** The output of a measurement device when recording external impulse changes, such as pressure deviations recorded by an ultrasound detector, is called impulse response. In the case of optoacoustic imaging, the total impulse response is a convolution of electrical and spatial impulse response. Here, the electrical response heeds the not ideal signal processing performance of a given ultrasound detector which prohibits the accurate reproduction of the original signal. As will be discussed below, e.g. the piezoelectric element acts as a bandpass filter around a thickness-dependent central frequency. Furthermore, the frequency dependent electrical amplification of a recorded acoustic signal contributes to this distortion. The spatial impulse response relates to the detector size as discussed in c). As the detector size is finite, an incoming acoustic signal might be recorded successively at multiple points on the detector surface. As a consequence, the recorded time domain signal is distorted and will lead to a decrease in overall resolution of an imaging system. In comparison, optical detectors are often wideband and can be miniaturized to micron scales, diminishing e.g. the bandpass filter effect of a detector as well as the smearing of the temporal signals, respectively.

In the following sections, various acoustic sensing technologies are introduced and representative performance parameters are summarized in tables 3.1 to 3.4, respectively.

3.2 Piezoelectric Transducers

Supposedly, the most widespread way to detect, generate and steer acoustic signals is based on the piezoelectric effect which occurs in crystalline structures that are not centrosymmetric and can generally be divided into two categories [4, 66, 67]:
The first category is called the *direct* piezoelectric effect and is depicted in Figure 3.1. Here, pressure is applied onto a piezoelectric element with the subsequent stress generating an electric polarization in the crystalline structure. The applied pressure is then proportional to the e.g. longitudinal dimensional change of the piezoelectric element and in turn to the voltage that can be detected across electrodes attached to it. When applied in optoacoustic imaging or ultrasonography, pressure is created by impinging acoustic waves.

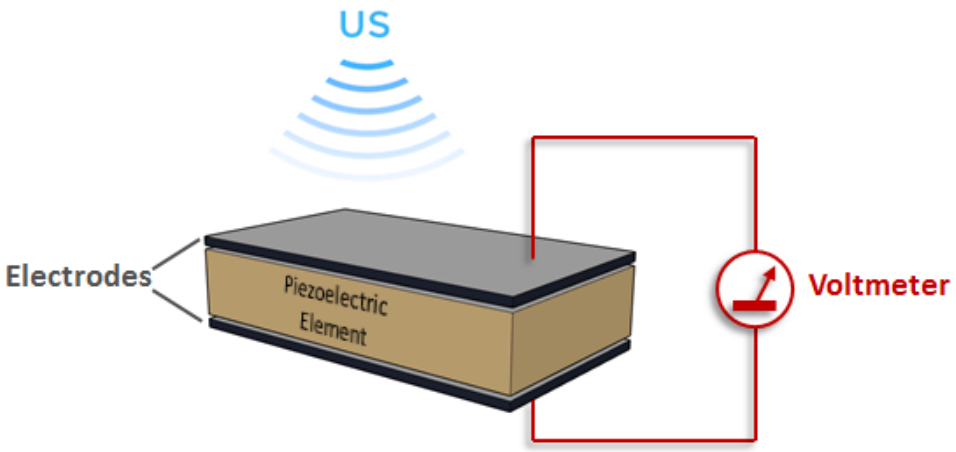

Figure 3.1: Mechanical energy conversion in a piezoelectric element: Mechanical stress is applied by incident acoustic (ultrasound) waves.

The second category is called the *converse* piezoelectric effect and is shown in Figure 3.2. In contrast to the direct effect, a voltage is applied and creates an electric field in the piezoelectric element. The electric field then aligns the randomly oriented piezoelectric domains that in turn induce strain onto the entire element. An alternating electrical field can then create a successive compression and extension along the axis of the element and thus create acoustic waves. Among other applications, the converse effect can be utilized as ultrasound transducer as well as translational element in precision actuators and motion controllers.

Piezoelectric elements constituted the enabling factor for ultrasonography and as a consequence, ultrasound diagnostics has evolved around piezoelectric technology since the 1950s [4]. The crucial reason for this development was the ability of piezoelectric transducers to both generate and detect ultrasound signals. Furthermore, piezoelectric transducers that have not been extensively miniaturized are relatively sensitive, easy to operate and can be manufactured to suit 1D and 2D transducer arrays. As a consequence, decades of development have led to highly sophisticated piezoelectric elements that advanced and even enabled optoacoustic imaging systems such as in the case of hybrid ultrasonography-optoacoustic sensors [19].

The most commonly applied piezoelectric material is lead zirconate titanate (**PZT**), a durable and easy to manufacture polycristaline ceramic [66]. More recently, a number of polymer-based piezoelectric materials have been introduced, such as vinylidene fluoride (**VDF**) and tetrafluoroethylense (**TeFE**) [68] which offer an increased sensitivity to

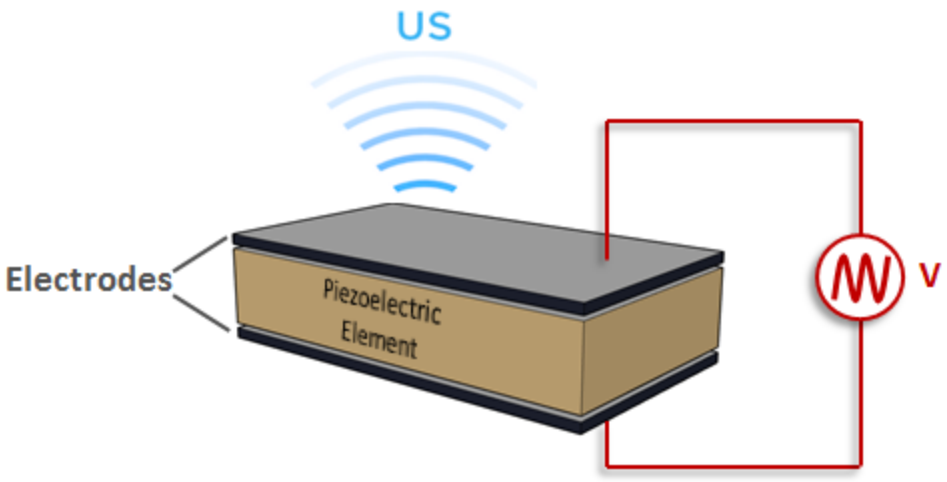

Figure 3.2: Electrical energy conversion in a piezoelectric element: Acoustic (ultrasound) waves are created by an applied alternating voltage.

acoustic signals and transparency of the piezoelectric element, respectively. On the other hand, these novel materials lack the rigidity and durability of PZT elements and consequently they have not been broadly applied yet. A detailed mathematical essay of piezoelectricity can be found in reference [67]. For reviewing piezoelectric elements for the detection of ultrasound, it is sufficient to note the natural vibrating frequencies (also referred to as central or resonant frequencies) of a piezoelectric element [67]:

$$f_{res} = nf_0 = n\frac{\nu_0}{2l} \;\; with \;\; n = 1, 2, 3, .. \tag{3.1}$$

Here, an individual resonant frequency f_{res} may be an odd multiple of the original resonant frequency f_0, with the loss-free acoustic propagation speed ν_0 and the thickness of the piezoelectric element l. Looking at the sensitivity towards acoustic perturbations and considering the requirements formulated in section 3.1, piezoelectric transducers are ultimately limited in their application for optoacoustic imaging. The main reason for this limitation lays in the sensitivity that scales with the surface area of a given piezoelectric element, limiting miniaturization approaches as well as the creation of small and densely packed arrays of ultrasound transducers. The latter is particularly important for increasing the resolution in tomographic applications while not decreasing the overall imaging depth due to lower sensitivity.

Another reason for the inherent limitation of piezoelectric transducers is based on the highest achievable central frequencies. Here, the central frequency is inversely proportional to the height of the piezoelectric element and the manufacturing of such ultra-thin

elements is reaching technical limitations. While piezoelectric micro-machined ultrasound transducers (**PMUTs**) bypass this limitation by vapor deposition technologies [69], this approach is not easily feasible e.g. for the assembly of curved detector arrays spanning multiple centimetres.
Table 3.1 showcases a number of commercial piezoelectric ultrasound transducers. It is worth mentioning non-intuitive relations between specialized designs, as e.g. piezoelectric transducers are available that exhibit a particularly high sensitivity of around 0.2 $\frac{mPa}{\sqrt{Hz}}$. This is achieved by manufacturing a spherically focused piezoelectric element with a big surface. As each surface part of the piezoelectric element is then oriented vertically towards the acoustic source, also the central frequency of 50 MHz is fairly high in comparison. In contrast, a flat piezoelectric element - as utilized in subsection 1.2.1 - has a lower central frequency of 15 MHz, although the element surface is more than 30 times smaller than that of the spherically focused transducer.

Table 3.1: Piezoelectric ultrasound transducers.

	Central Frequency [MHz]	Size $[mm]$	NEP $\left[\frac{mPa}{\sqrt{Hz}}\right]$	NEP × area $\left[\frac{mPa\,mm^2}{\sqrt{Hz}}\right]$
Olympus V214-BB-RM (piezoceramic)	50	30	0.2	6
Precision Acoustics Needle Hydrophone (VDF)	12	1	14.4	14.4
Boston Scientific Atlantis PV [60]	15	0.8	450	360

(NEP, noise equivalent pressure)

3.3 Micromachined Transducers

Micromachined ultrasound transducers are an emerging alternative to classic piezoelectric elements and are generally divided into two categories: piezoelectric micromachined ultrasound transducers (**PMUTs**) and capacitive micromachined ultrasound transducers (**CMUTs**). It is a very exciting approach to a wide range of applications related to ultrasound sensing, as PMUTs and CMUTs can create and shape ultrasound wave fronts similar to piezoelectric elements but with ultra-high density transducer arrays and micron sized individual transducer elements. Both types are produced by semiconductor

fabrication technologies and are commonly created on silicon substrates. This very nature of micromachined transducers might enable fully integrated optoacoustic devices in the future, as together with e.g. silicon-on-insulator (**SOI**) platforms, it allows to embed lasing elements, optical waveguides as well as electronic circuits comprising photodiodes and amplifiers into a single micro-device.
Strictly speaking, SOI based optical resonators are usually manufactured using identical methods to PMUT and CMUT production, but micromachined optical resonators such as micro-rings are discussed together with other resonator designs in subsection 3.4.3, as most optical detectors may only detect but not produce acoustic signals.

3.3.1 Piezoelectric Micromachined Transducers

The configuration of a typical PMUT is depicted in Figure 3.3 [69, 70]. A piezoelectric film is sandwiched between two thin electrodes and manufactured on top of a membrane or a lever. When perturbed by acoustic signals, the membrane can oscillate longitudinally due to a cavity or clearance in the silicon substrate beneath. Piezoelectric materials such as VDF or aluminium nitrate (**AIN**) are common in PMUTs due to their applicability in micro-electro-mechanical system (**MEMS**) manufacturing [71]. The fabrication process of a PMUT array is depicted in Figure 3.4, where the geometry of an individual element is shown in close-up view and the deposition process of the constituting layers is shown in cross-sectional view [72].

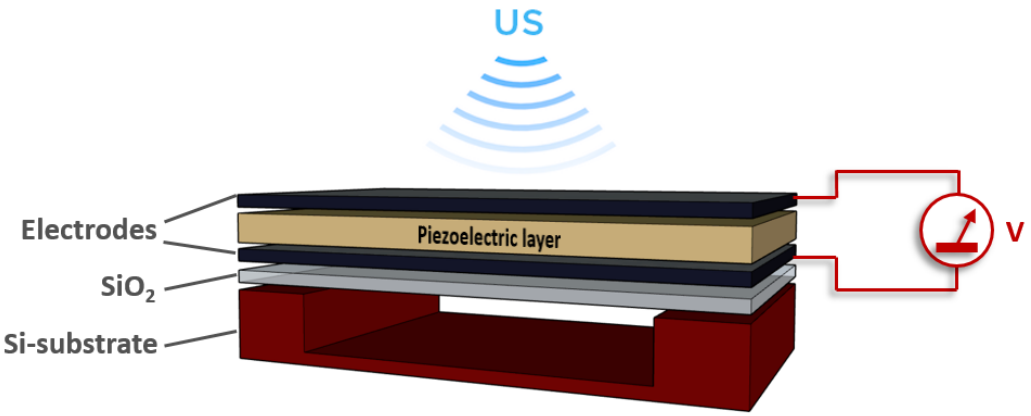

Figure 3.3: Basic principle of a PMUT element: A piezoelectric element is fabricated atop a cavity etched into silicon substrate, with mechanical stress applied by incident ultrasound waves [69].

Ordinary piezoelectric transducers utilize the longitudinal vibration mode (d_{33}-mode) of the piezoelectric material or composite. In PMUTs on the other hand, the piezoelectric

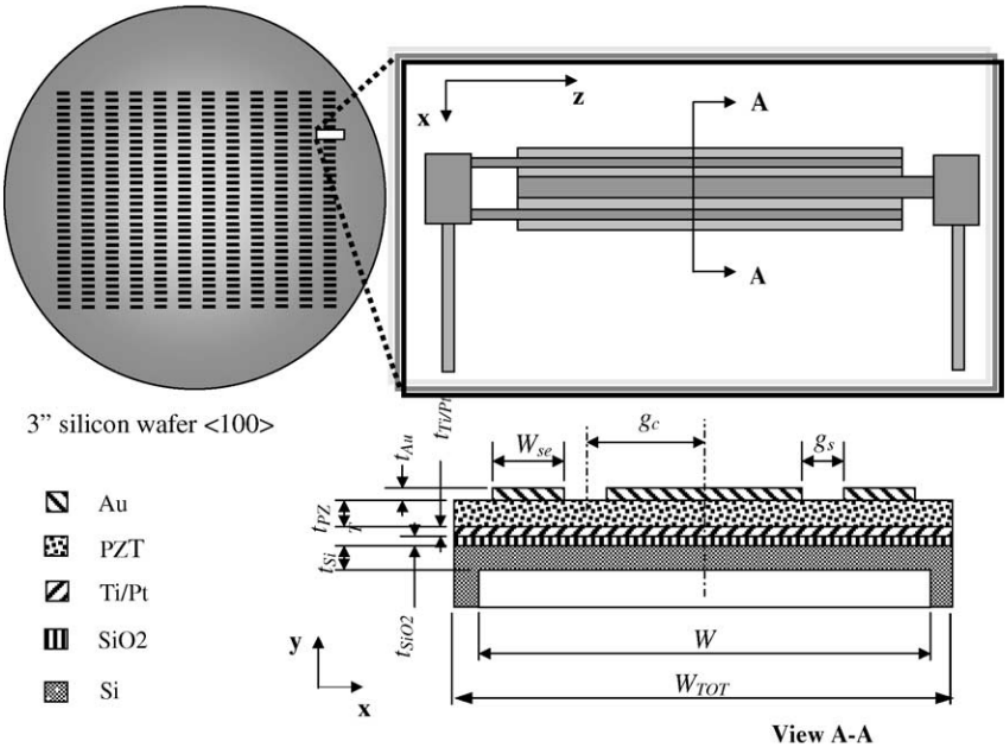

Figure 3.4: Principle of PMUT production: Multilayer transducers are fabricated on a silicon wafer with close-up top-view and cross-sectional view. Reproduced with permission from [73].

effect can utilize lateral vibration modes (d_{31}-mode) that propagate along the surface of the membrane, perpendicular to the PMUT axis. When creating acoustic signals, the bulging of the membrane is caused by lateral strain that is in turn induced by a voltage applied to the piezoelectric film. When detecting acoustic signals, longitudinal oscillations of the membrane induce lateral strain on the piezoelectric film, inducing a voltage across it [69]. As a consequence of operating in the d_{31}-mode, the resonant frequency of PMUTs does not depend on the thickness of the piezoelectric film such as in thick piezoelectric elements, but rather on the membrane size as well as constraining and mechanical parameters of the PMUT element. In the case of PMUTs manufactured atop of cavities etched into silicon substrate, the bandwidth is consequently constrained by the lateral dimension of the aperture. This is particularly useful, as piezoelectric film thicknesses range from μm to sub-μm [74], corresponding to central frequencies of hundreds of MHz up to the GHz scale. While higher frequencies are generally advantageous in order to improve image resolution in optoacoustic tomography, acoustic attenuation in water and tissue is frequency dependent and therefore a limiting factor for the overall imaging

depth. The attenuation can be estimated as around 0.5 dB per MHz per cm [4], e.g. corresponding to an attenuation of 50 dB over 1 mm depth for ultrasound signals with a frequency of 1 GHz.
A 64 x 4 array of PMUTs was successfully applied in *in vivo* intracardiac ultrasonography imaging in swine studies, where the PMUTs were operated at 5 MHz [75]. Due to the small array size and the low central frequency, the image resolution was as low as 1 mm and worse. Another approach demonstrated PMUTs in d_{33}-mode for optoacoustic breast tomography with a module consisting out of 25 individual transducers with a central frequency of around 1 MHz, a bandwidth of 0.8 MHz and a sensitivity of 0.5 Pa NEP [76].

3.3.2 Capacitative Micromachined Transducers

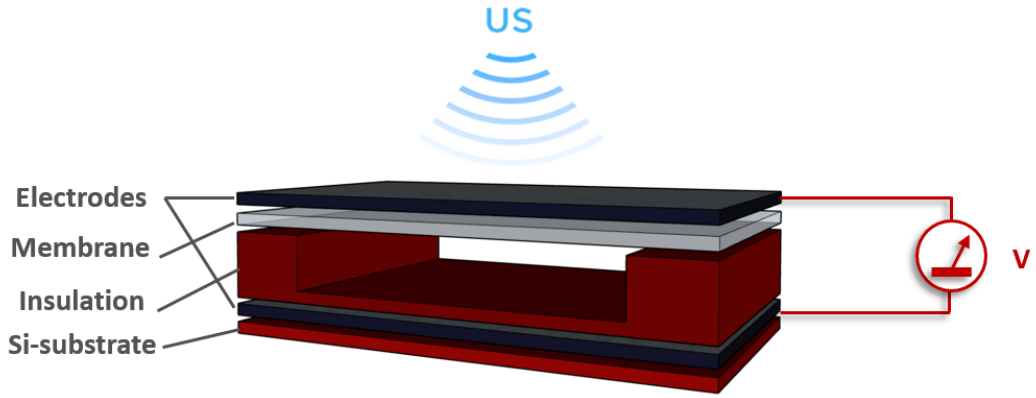

Figure 3.5: Basic principle of a CMUT element: Mechanical stress is applied onto the element by incident acoustic waves (Ultrasound), resulting in an alternating capacitance [69].

The working principle of a CMUT is depicted in Figure 3.5 [69, 77]. Here, a thin electrode is attached to a membrane that is in turn suspended on top of a cavity in the Si-substrate or a deposited Insulation. Within the substrate or beneath the insulation, a second electrode is embedded, effectively creating a capacitor. The top electrode may be fabricated of silicon nitrate and the bottom electrode might be the Si-substrate itself. When applying voltage onto the electrodes, the subsequent electric field leads to an electrostatic attraction between the electrodes. The membrane and substrate stiffness constitute the restoring force, counteracting against the electrostatic attraction between the electrodes. Utilizing this force interplay and applying an alternating voltage onto the electrodes, acoustic signals can be generated by the oscillating membrane [69]. In a similar way, acoustic waves that perturbate the membrane change the capacitance of the

CMUT and in turn induce detectable voltage shifts across the electrodes.
CMUTs are more widespread and advanced than PMUTs, as the they can be fabricated using existing MEMS technology and without the need for challenging aspects of piezoelectric element fabrication, such as thin film deposition [77]. In order to demonstrate the technological progress of CMUTs, image 3.6 shows a photograph of a commercial piezoelectric pulse-echo ultrasound device for ultrasonography in comparison to a handheld probe based on a CMUT array. While the sensitivity of individual CMUTs is not exceeding that of piezoelectric transducers yet, CMUTs offer a number of advantages, such as the very high array-density. Together with phased array activation, a high transducer density allows for precise electronic steering and focusing of 1D and 2D ultrasound wavefronts [69].

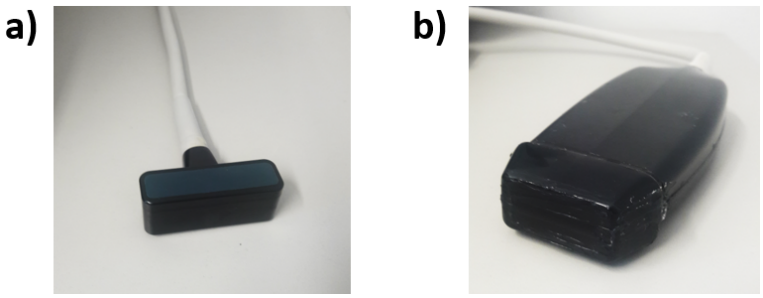

Figure 3.6: Commercial piezoelectric and CMUT based handheld ultrasonography probes: (a) Piezoelectric 128-element array with 300 μm pitch, 7.5 MHz central frequency. (b) 128-element CMUT array with 70 μm pitch, 10 MHz central frequency. Both devices have an embedded acoustic matching layer and a cylindrical lens for acoustic focusing. Probes fabricated by Vermon S.A. (Chambray-Les-Tours; France) and provided by Dr. Murad Omar, Helmholtz Zentrum Muenchen.

For the application in optoacoustic imaging, CMUTs were fabricated and characterized with acceptance angles of ±18 deg [78] especially at higher frequencies, the acceptance angle of CMUTs is up to 10 times broader compared to PZT-based hydrophones (Table 3.1). This is particularly advantageous, as the spatial extent and the frequency response of ultrasound detectors is a determining factor for tomographic image reconstruction and the resulting image quality. A 2D CMUT array with 16 x 16 elements and an individual transducer size of around 30 μm has been reported (see Table 3.2) [72]. Here, the researchers bonded the CMUT array with an integrated circuit (**IC**) that included a high voltage pulser and a pre-amplifier for creating and detecting ultrasound signals, respectively. With the pre-amplifier installed in close proximity to the CMUTs, losses along transmission wires as well as external noise were diminished. The complete device had a dimension of 5.6 mm x 6.9 mm which makes it highly attractive for miniaturized

sensor heads.

Table 3.2: Micro-machined ultrasound transducers.

	Material	f [MHz]	Area $[mm^2]$	NEP $\left[\frac{mPa}{\sqrt{Hz}}\right]$	NEP × area $\left[\frac{mPa\,mm^2}{\sqrt{Hz}}\right]$
PMUT [76]	PZT / SiO_2	0.8	0.81	0.56	0.45
CMUT [72]	Silicon	5	0.06	1.8	0.11

(NEP, noise equivalent pressure)

3.4 Optical Ultrasound Detectors

The following sections review the performance and perspective of established optical methods for ultrasound sensing in the framework of optoacoustic imaging. These optical methods are divided into three categories: refractometric detectors, interferometric detectors and resonator based detectors.

Refractometric methods are based on the detection of ultrasound-induced changes in refractive index (**RI**) inside a medium or sample (see Figure 3.7). Essentially, a change in RI, e.g. at the interface between two media, induces observable modulations of the intensity, the deflection angle or the phase of an interrogating (or read-out) laser beam. Interferometric methods are based on the interaction of ultrasound with a specific component of an interferometric setup (see Figure 3.8 to Figure 3.13). In two-beam interferometers, ultrasound may interact directly or indirectly with one of the interferometer arms, perturbing e.g. a beam or a reflector, respectively. In resonator as well as in Doppler-based interferometers, ultrasound interacts with the resonator or the reflector itself. In each case, the recording of ultrasound is then achieved by observing intensity or frequency shifts at the interferometer output.

It is interesting to note that current research on optical ultrasound detectors has picked up on all of these rather diverse methods, ranging from free beam interferometers to micron-sized silicon resonators, rather than to focus on a particular method only. Hence, various interferometers and their implementation with free beam optics or optical fibers as well as read-out methods for the interrogation of optical resonators are presented in the following two sub-chapters. Although sensing and read-out mechanisms are often

intertwined, because some sensing mechanisms rely on specific interrogation mechanisms and vice versa, they are discussed individually for the sake of presentation simplicity.

3.4.1 Refractometric Detectors

A well established refractometric method utilizes intensity variations of an interrogating light beam that is reflected from the interface between two adjacent media. The two media posses a different RI and when perturbed by ultrasound, the respective RI at the interface shifts according to the photoelastic principle. As a consequence, the intensity of the reflected interrogation beam is modulated proportionally to the pressure variations induced by the ultrasound and can be recorded by a photodiode. The working principle is depicted in Figure 3.7a with the interrogation beam of a cw-laser reflected off a glass-water interface.

A similar design has been successfully applied in optoacoustic microscopy improves the basic principle by splitting the interrogation beam into two components, polarizing each component differently and by recombining them in the same beam path [79]. The two components of the reflected light are then monitored separately and recording their intensity ratio allows to improve the SNR of the system. This design achieved a NEP of 1 kPa (corresponding to 100 $\frac{mPa}{\sqrt{Hz}}$) and a bandwidth of 100 MHz (see Table 3.3). The latter is limited mainly by the rise time of the photodiode and - in the hypothetical case of applying it in optoacoustic tomography - also by the diameter of the interrogation beam and the size of the reflecting interface.

A similar and particularly successful design for all-optical optoacoustic microscopy exploits surface plasmon resonances (**SPR**) to detect RI changes. In this setup, a polarized interrogation beam induces surface plasmon waves on a metal-coated glass surface adjacent to the coupling medium. Ultrasound waves interacting with this interface then alter the resonance condition of the SPRs and consequently the intensity of the reflected interrogation beam. Ultrasound recording is then performed by monitoring the reflected intensity with a photo-sensitive element, similar to the way described above.

Another design is based on optical fibers and aims at minimally invasive applications, such as intravascular endoscopic laser ablation of plaque, where ablation progress can be monitored by recording acoustic shockwaves during the procedure [80]. It is particularly useful for this application that refractometric sensing commonly exhibits a wide dynamic range, allowing to detect acoustic pressure from kPa up to MPa [17].

Deflection-based sensing is another refractometric method that has been successfully applied in optoacoustic imaging [81, 82]. Here, ultrasound is detected by measuring the

deflection of an interrogation beam that is passing through a coupling medium which in turn is in contact with the acoustic source. In the framework of acoustic sensing, beam deflection is induced by ultrasound waves modulating the RI of the medium along the expanding wave fronts. These wave fronts resemble interfaces of two media with different RIs and deflect the interrogation beam accordingly. The basic principle is shown in Figure 3.7b, where the reflected interrogation beam is resized and guided onto a quadrant photo diode (**QPD**). The QPD measures the beam deflection very precisely by monitoring shifts in the lateral intensity ratios recorded from four adjacent photodiodes. Contrary to intensity sensitive methods described above, the bandwidth of deflection-based methods is primarily limited by the diameter of the interrogation beam, where a thinner beam implies a higher achievable bandwidth. Hence, bandwidth dependent applications, such as optoacoustic microscopy, use needle-beams as thin as 90 μm in diameter, achieving a theoretical bandwidth of 17 MHz. While this bandwidth is not ideal, the high sensitivity of 11.4 Pa successfully compensates for it, as was demonstrated by OAM images of single erythrocytes [81].

Phase-sensitive methods constitute the third refractometric sensing method and utilize Schlieren photography, phase-contrast imaging and shadowgraphy for imaging. In this approach, ultrasound induces phase-shifts inside a highly collimated interrogation beam that is guided through a coupling medium or under certain conditions through the sample itself [83]. Inside the interrogation beam, light rays converge or diverge depending on pressure induced shifts in the RI of the coupling medium, creating a perturbed beam as demonstrated in Table 3.3c. This beam is then tightly focused through a spatial light filter (such as a pinhole) that is located in the Fourier plane. Here, perturbed light rays with out-of-phase photons are filtered out and subsequently collimated again for a negative contrast projected onto a screen or recorded by a CCD/CMOS camera. Alternatively, the beam can be focused onto an obstruction target (such as an annular obstruction target), filtering out the in-phase photons at the focal spot for a positive contrast image of the intensity distribution of the original acoustic field. Recording these intensity distributions over time with a fast camera allows for tomographic reconstruction of 3D images of the acoustic field.

Phase-sensitive methods were originally developed for e.g. the characterization of active piezoelectric elements or the study of acoustic shock waves on aircraft [84, 85]. Here, high acoustic intensities of hundreds of kPa allowed for an easier acoustic detection than would be the case in biomedical sensing, where intensities are smaller. Phase-sensitive setups were demonstrated with a sensitivity in terms of 5.1 kPa NEP [84] and a bandwidth of

Table 3.3: Refractometric ultrasound detectors.

	Bandwidth [MHz]	Sensing element, size [mm]	NEP $\left[\frac{mPa}{\sqrt{Hz}}\right]$	NEP × area $\left[\frac{mPamm^2}{\sqrt{Hz}}\right]$
Intensity-sensitive [79]	100	Prism, 15	100	22×10^3
Beam-deflectometry [81]	17	Needle-beam, 0.09	2.76	N.A.
Phase-sensitive [85]	110	Schlieren-beam, 10	486	N.A.

(NEP, noise equivalent pressure; N.A., not applicable)

up to 110 MHz [85].

The most promising aspect of phase sensitive ultrasound detection and the corresponding experimental approach is shown in Figure 3.7d. Here, optoacoustic signals are generated with no immediate contact to the Schlieren beam. Instead, an acoustic lens with a high numerical aperture (**NA**) collects acoustic signals and focuses them into a volume that is in turn interrogated by the Schlieren beam as discussed above and shown in Figure 3.7c. This approach has a number of advantages: Firstly, the sample is decoupled from the optical path of the Schlieren beam, hence avoiding interference of the sample with the beam. Secondly, it allows for a separation of the optoacoustic excitation laser and the interrogation beam, avoiding the creation of parasitic optoacoustic signals inside the acoustic coupling medium. Thirdly, this method allows for real-time tomography imaging without computational tomographic reconstruction [54]. The latter is particularly important, as from a detection point-of-view, both the axial and the spatial resolution are limited only by the optical resolution of the system and e.g. the speed of the CMOS sensor.

3.4.2 Interferometric Detectors

The first applications of optical interferometry as a measuring device for vibrational displacements were enabled by the advancement of lasers in the 1960s [86, 87]. In the 1970s, optical fibers [88] and optical resonators [89] were first presented to detect acoustic signals. Eventually, methods for the interferometric non-contact detection of acoustic signals, e.g. using the Doppler-effect, were demonstrated in the 1980s and 1990s [90].

Two-beam interferometers, such as Michelson interferometers (**MI**) depicted in Figure 3.8

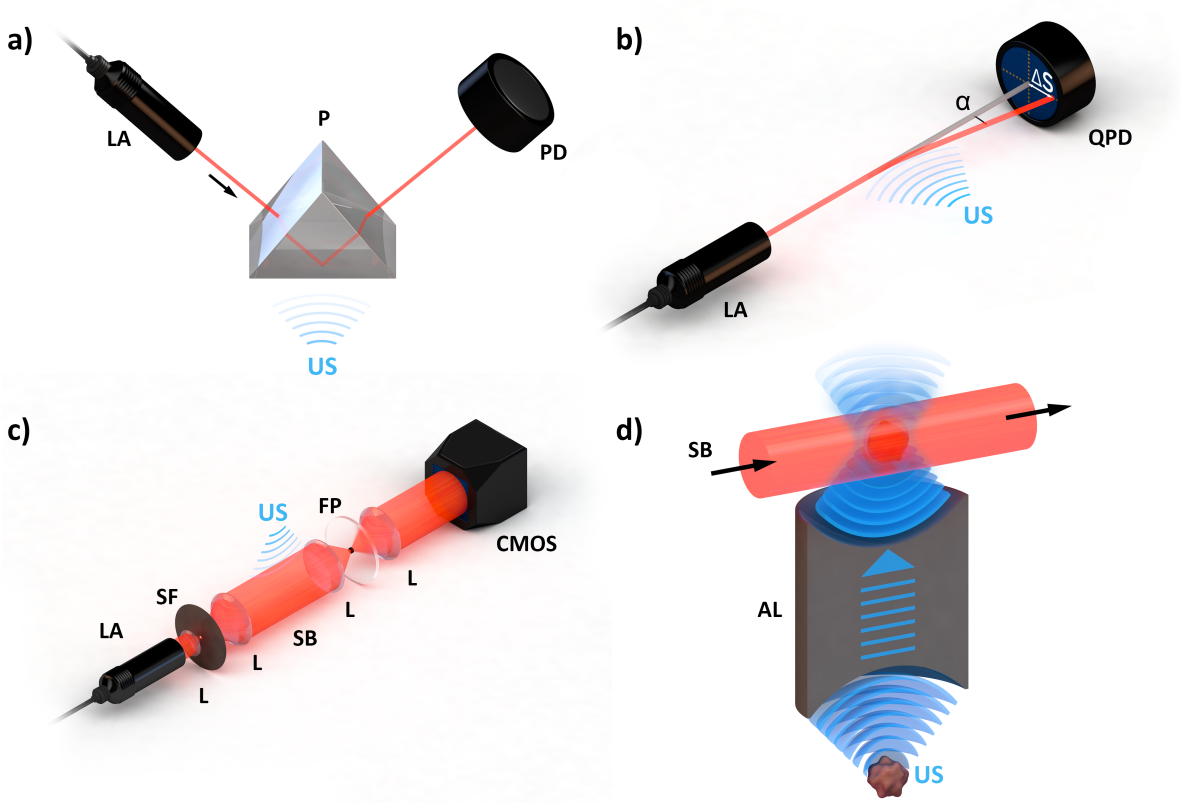

Figure 3.7: Refractometric ultrasound detectors: (a) Intensity-sensitive detection. (b) Beam-deflection. (c) and (d) Phase-sensitive detection with direct (c) and indirect (d) acoustic coupling of the optoacoustic source to the Schlieren beam. AL, acoustic lens; CMOS, CMOS camera; FP, Fourier plane; L, lens; LA, laser; P, prism; PD, photodiode; QPD, quadrant photo detector; SB, Schlieren beam; SF, spatial filter; US, ultrasound.

and Mach-Zehnder interferometers (**MZI**) shown in Figure 3.9 measure phase variations caused by ultrasound [91]. In both MIs and MZIs, a laser beam is divided into two arms: a sensing arm and a reference arm. The sensing arm is exposed to the perturbations induced by ultrasound and later combined with the reference arm. Monitoring variations in the intensity at the interferometer output, acoustic signals can be detected. The recorded intensity variations are approximately proportional to acoustic perturbations over an extended dynamic range that depends on the respective interferometer and the applied read-out method. In MI setups 3.8, the acoustic sensing can be performed either directly in the beam path of the sensing arm or at a reflector installed in the same path. Also in the case of MZI setups (see Figure 3.9), the ultrasound source can interact with the sensing arm directly or with a reflector that is installed in the beam path. Most commonly though, setups are designed in a way that the beam path is traversing through

a defined volume which can be e.g. a water tank filled with the water being the acoustic coupling medium for the loss-free propagation of ultrasound signals. Both MIs and MZIs require a coupling medium when acoustic sensing is performed along the sensing arm. When acoustic sensing is performed at a reflector though, an acoustic coupling medium might not be necessary - especially if the interrogated sample is used as reflector [34, 92]. The second category of interferometric ultrasound detection is based on the frequency detection of Doppler shifted light, as seen in Figure 3.10 [93]. Here, the acoustic perturbation is detected at the reflector which can be e.g. the surface of a tissue from which a interrogating laser beam is reflected from. Contrary to MIs and MZIs, the Doppler shift of the interrogation beam is monitored, rather to measure its phase shift with an interferometric read-out mechanism that relies on a reference arm. The Doppler shift in turn can be detected by a separate optical interferometer acting as a wavelength meter. Doppler interferometry is particularly advantageous when the reflector is a rough surface that gives rise to a distorted wavefront exhibiting a speckle pattern. Interfering a distorted wavefront with itself such as in the MZI depicted in Figure 3.9, would generally result in a stronger interferometric visibility than interfering a distorted wavefront with the nearly planar wavefront of the reference arm in MIs as depicted in Figure 3.8.

3.4.3 Resonator Based Detectors

The third category of interferometric sensing mechanisms is depicted in 3.11. It is based on optical resonators and is - strictly speaking - another interferometric method. In this sensing approach, a read-out beam is trapped inside an optical resonator, confining light within a small volume. The optical resonator then acts as the sensing element

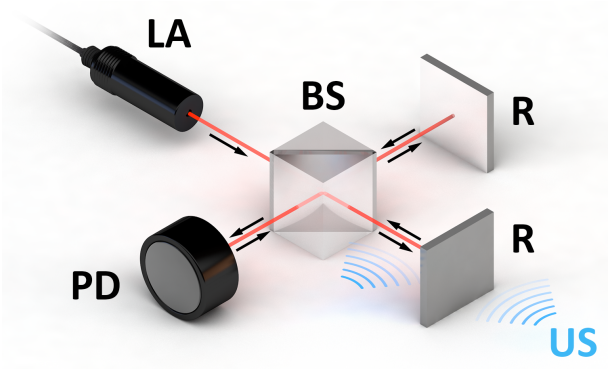

Figure 3.8: Michelson Interferometer. BS, beam splitter; D, detector; DM, demodulator; LA, laser; PD, photodiode; R, reflector; US, ultrasound.

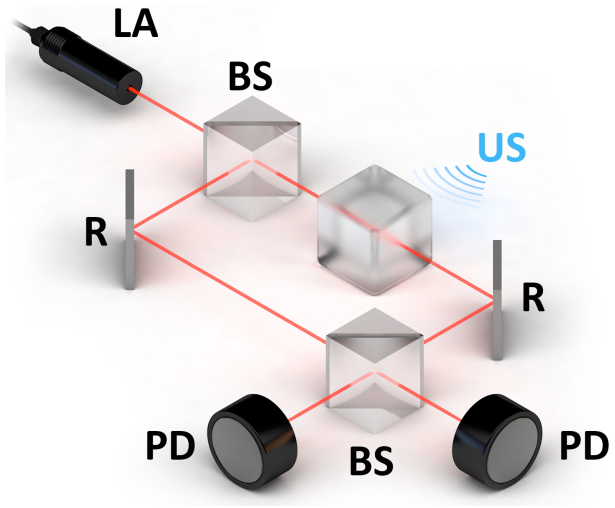

Figure 3.9: Mach Zehnder Interferometer. BS, beam splitter; D, detector; DM, demodulator; LA, laser; PD, photodiode; R, reflector; US, ultrasound.

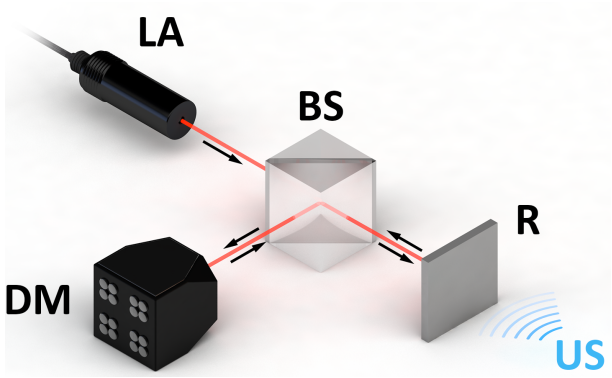

Figure 3.10: Doppler Interferometer. BS, beam splitter; DM, demodulator; LA, laser; R, reflector; US, ultrasound.

and is exposed to the investigated acoustic signals. A big advantage of this method is, that compared to two-beam interferometers as well as to Doppler interferometry, the interaction time of the acoustic signals and the read-out beam is increased. Another advantage of this method is the fact that only the light inside the resonator is used for ultrasound detection. This enables the design of highly miniaturized resonators down to the μm scale and as a consequence, the creation of very dense and miniaturized detector arrays.

The light confinement in optical resonators can best be explained by investigating the classic Fabry-Pérot (**FP**) interferometer [94]: In an ideal setup, a FP comprises two parallel and planar mirrors that are separated by a distance L. The volume between

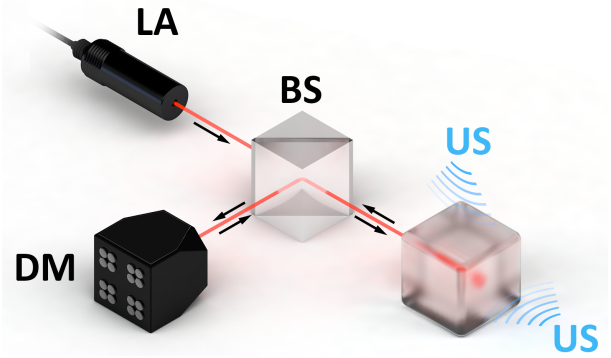

Figure 3.11: Optical Resonator. BS, beam splitter; DM, demodulator; LA, laser; US, ultrasound.

the mirrors is filled with a medium of known loss factor V, which takes into account the loss in light intensity of a light beam inside the medium. Light of a wavelength λ that is incident onto the FP and enters the medium through one of the mirrors, will be in turn partially reflected and transmitted by the two mirrors. During each reflection and transmission, light is transmitted through each mirror that gives rise to two key parameters of FPs: First, the light that leaves the FP along the direction of the initial incident beam and second, the light that leaves the FP in the opposite direction. The transmitted and reflected fields E_t and E_r are given by:

$$E_t = -E_0 t_1 t_2 v e^{[ikL]} \sum_{n=0}^{\infty} (v^2 r_1 r_2 e^{[i2kL]})^n \tag{3.2}$$

$$E_r = E_0 \left[r_1 - t_1^2 v^2 r_2 e^{[i2kL]} \sum_{n=0}^{\infty} (v^2 r_1 r_2 e^{[i2kL]})^n \right] \tag{3.3}$$

Here, v denotes the amplitude of the loss factor V, r_1 and r_2 denote the reflection and t_1 and t_2 the transmission coefficients, respectively. The intensities of E_t and E_r then are:

$$I_t = (1 - R_1)(1 - R_2)V \tag{3.4}$$

$$I_r = \left(\sqrt{R_1} - \sqrt{R_2} V \right)^2 + 4\sqrt{R_1 R_2} V \sin^2 (kL) \tag{3.5}$$

while the intensity of the incident light before entering the FP is given by:

$$I_0 = \left(1 - \sqrt{R_1 R_2} V \right)^2 + 4\sqrt{R_1 R_2} V \sin^2 (kL) \tag{3.6}$$

Here, the reflectivity is denoted by $R_i = |r_i|^2$, the loss factor by $V = |v|^2$ and the wave number by $k = \frac{2\pi}{\lambda}$. In the ideal case of no intensity loss inside the medium and two identical mirrors, $V = 1$ and $R_1 = R_2$, the ratio of the intensities I_t and I_r relative to the intensity of the incident light I_0 then reveals the transmission **T** and reflectance **R**:

$$T = \frac{(1-R)^2}{(1-R)^2 + 4R\sin^2(kL)} \tag{3.7}$$

$$R = \frac{4R\sin^2(kL)}{(1-R)^2 + 4R\sin^2(kL)} \tag{3.8}$$

Transmission [3.7] and reflectance [3.8] are plotted in figure Figure 3.12 for representative reflectivities of 0.3, 0.6 and 0.9. Here, the transmission maxima occur at $\sin(kL) = 0$, with

$$\lambda = \frac{2L}{n} \; with \; n = 1, 2, 3, .. \tag{3.9}$$

The distance $\Delta\nu = \frac{c}{2L}$ between the transmission maxima represents the free spectral range (**FSR**) and is a typical characterisation factor of FP resonators. As the FSR limits the applicable bandwidth of the interrogating laser beam of a given FP, large FSRs are normally advantageous. For example, a slab-shaped FP of 20 μm thickness has a FSR of 3.75 THz.

Another important parameter for the application of FPs as ultrasound detectors is the FWHM of the resonance peaks. In short, narrower FWHMs are desirable as they commonly offer a higher sensitivity towards acoustic signals. For a FP with given L, the FWHM is

$$\delta\nu = \left|\ln\sqrt{R_1 R_2}V\right| \frac{c}{2\pi L} \tag{3.10}$$

The quality factor **Q** (Q factor) is a measure for the relative linewidth and more generally for the performance of an optical resonator. Q is given by

$$Q = 2\pi\Delta\nu\tau \quad with \quad \tau = \frac{L}{c}\frac{1}{\left|\ln\sqrt{R_1 R_2}V\right|} = \frac{1}{2\pi\delta\nu} \tag{3.11}$$

where τ is the decay time that specifies the instance when $\frac{1}{e} \approx 0.37$ of the stored energy is left inside the resonator. The Q factors of different resonator designs are compared in table 3.4.

Figure 3.13 shows illustrations of the most common resonator geometries used in optoa-

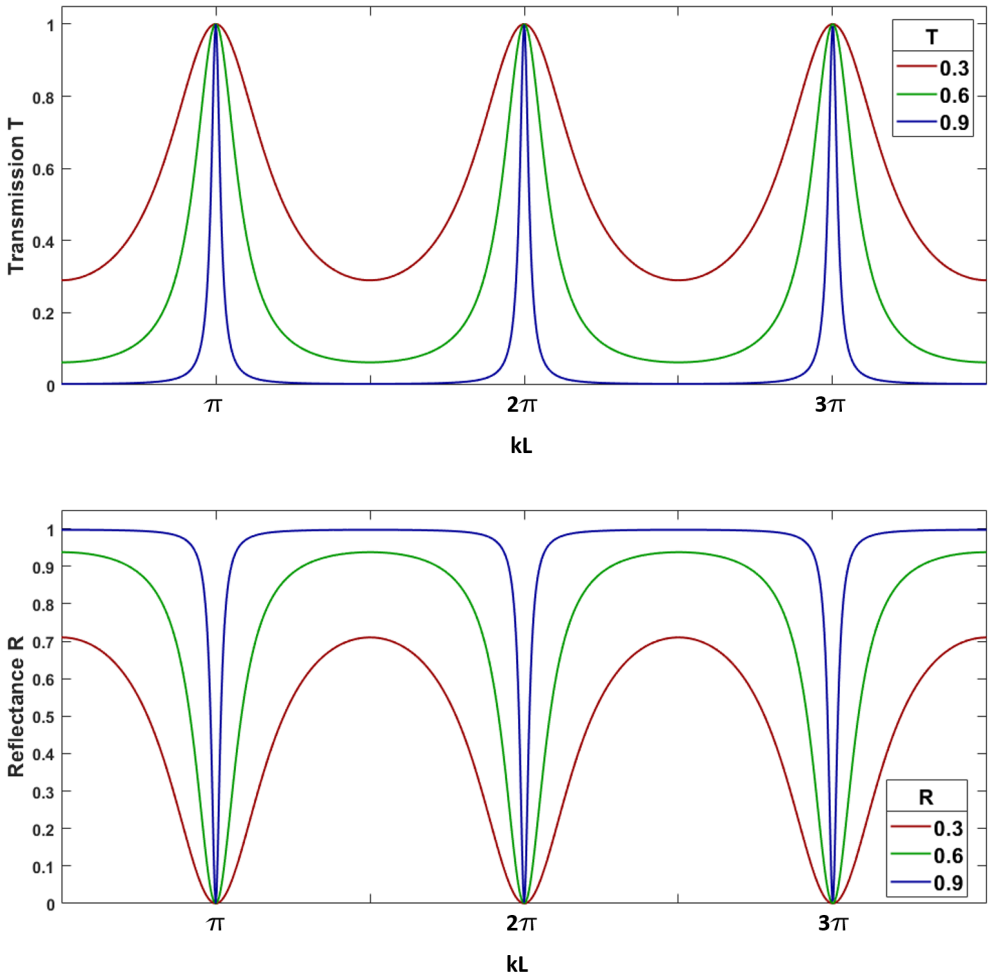

Figure 3.12: Transmission and reflectance for an ideal FP as function of phase.

coustic imaging: FPs, micro-ring resonators (**MRRs**) and π-phase shifted Bragg gratings (π-**BGs**).

In the case of classic FPs, the interrogation beam is trapped inside a volume between two parallel mirrors or reflecting surfaces (see Figure 3.13a). Typical FP geometries are thin optically transparent foils coated with reflective materials [37] and similar slabs manufactured on the tips of optical fibers [95]. While e.g. the read-out of a slab-shaped FPs with a focused interrogation beam allows to virtually create ultra-dense detector arrays, an inherent limitation to this FP geometry lays in the relatively weak light confinement inside the resonators due to the optical transmissibility of at least one of the reflecting surfaces. Typical Q factors of high quality and thin slab-shaped FPs are in the order of 10^3 (see Table 3.4). In the context of optoacoustic tomography, FPs with a

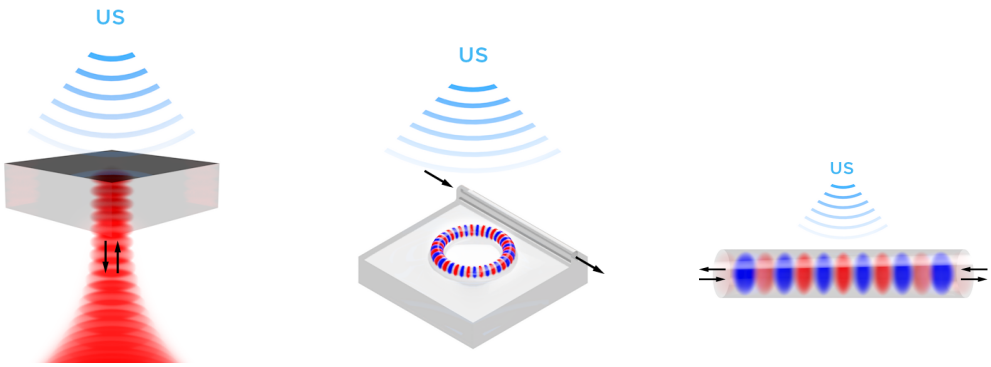

(a) Fabry-Pérot **(b)** Micro-ring **(c)** π-FBG

Figure 3.13: Common resonator designs demonstrated in optoacoustic imaging.

foil thickness of 38 μm have achieved sensitivites of 210 Pa at a measurement bandwidth of 20 MHz [96].

In MRRs, also known as optical ring resonators, the interrogation beam is coupled into a ring-shaped closed-loop optical waveguide (see Figure 3.13a). MRRs can be fabricated on transparent substrates and with ring diameters as small as 100 μm. These design parameters and the ability to direct an OR excitation beam into a sample through the substrate are highly advantageous for the application in optoacoustic microscopy. Polystyrene based MRRs have been reported with a Q factor in the order of 10^5, enabling sensitivities of up to 6.5 Pa and bandwidths of up to 140 MHz [65].

Optical resonators based on π-BGs are particularly interesting, as they offer light confinement at dimensions that are smaller than the actual physical dimensions of the distributed mirrors that are described by the BGs (see chapter 4). This extreme light confinement allows for Q factors at the order of 10^6 and in optoacoustic microscopy setups, sensitivities of 100 Pa at a bandwidth of 77 MHz were shown [24, 60]. This is especially noteworthy, as π-FBGs have a micron scale overall footprint and are therefore suitable for miniaturized and minimally invasive applications, such as in gastrointestinal and intravascular endoscopy (see subsection 1.2.1).

For resonators that are perfectly matched to the coupling medium such as water, bandwidth and acceptance angle are governed by the respective geometry as acoustic signals are averaged over the resonator volume [52]. For a slab based design, the central frequency is given by twice its thickness (see Equation 3.9) and its acceptance angle is governed by its width. For acoustic wavelengths that are much larger than twice the resonator width, an isotropical acceptance angle can be approximated. For increasing acoustic frequencies,

Table 3.4: Resonator-based ultrasound detectors.

	Bandwidth [MHz]	Size [μm]	Q factor	NEP $\left[\frac{mPa}{\sqrt{Hz}}\right]$	NEP × area $\left[\frac{mPamm^2}{\sqrt{Hz}}\right]$
Micro-ring [97,98]	350	1.4 × 20 × 20	1.4× 10^5	5.61	1.8×10^{-3}
Fabry-Pérot [99,100]	22.5	60 x 60 x 2000	N.R.	0.45	5.4 x 10^{-2}
π-FBG [24,60,62]	77	10 x 10 x 270	1.2 x 10^6	200	6.75 x 10^{-2}

(NEP, noise equivalent pressure; N.R., not reported)

the acceptance angle then decreases [65].

The sensitivity of optical resonators towards acoustic signals is determined by both the optical properties of the light confining region and the acoustic properties of the resonator material as well as by the interrogation method applied (see subsection 3.4.4). The NEP is then the product of the efficiency by which acoustic perturbations are converted to spectral shifts of the resonance and the smallest detectable resonance shift itself. For comparison, conversion efficiencies of the resonator designs depicted in Figure 3.13 are listed in Table 3.5.

Table 3.5: Resonator conversion efficiency in acoustic sensing.

Resonator design	Material	Conversion efficiency $[MPa^{-1}]$
Micro-ring [97,98]	Polystyrene	130 x 10^{-6}
Fabry-Pérot [99,100]	PET (Polyethylene terephthalate)	90 x 10^{-6}
π-FBG [24,60,62]	Silica	3.8 x 10^{-6}

When applying optical resonators as acoustic detector, one of the key parameters that define its sensitivity towards acoustic signals is the efficiency by which pressure variations are converted into optical resonance shifts [60]. As noted in [62], especially the optical

parameters of the cavity medium, such as its strain optical coefficient and compressibility, govern the ability of an optical resonator to detect sound. Therefore, fiber-based resonators have been demonstrated with materials that are e.g. doped (silica) or chosen for high strain optical coefficients (polymer waveguides).

3.4.4 Read-Out Mechanisms

Read-out mechanisms convert interferometer outputs such as phase or frequency shifts to voltage signals that can be electronically recorded e.g. by a digitizer.
Read-out in Doppler interferometry is commonly performed utilizing a cw-laser, where the Doppler frequency shift of the reflected beam is converted to a shift in optical intensity by a demodulator (see Figure 3.10). The demodulator can be any optical device with its read-out changing linearly to the spectral shift, such as a fast spectrometer or a Fabry-Pérot interferometer [101,102]. In the latter configuration, the resonance frequency of the Fabry-Pérot interferometer is tuned to the wavelength of the interrogation laser of the Doppler interferometer. Ultrasound induced frequency shifts on the reflector are then detectable as intensity variations at the output of the Fabry-Pérot interferometer. The most widespread interrogation approaches for two-beam interferometers and resonator-based interferometry are also based on cw-lasers. Here, a laser is tuned to the spectral section where intensity variations behave linearly. Depending on the spectral dynamic range of the respective interferometer, acoustic perturbations affecting the interferometric condition are then proportional to recorded power variations at the interferometer output. Additionally, the temporal variations of the recorded power read-out directly translate to the acoustic signal as it is averaged over the volume of the detector. In optical resonators, the geometry as well as the speed of sound in the resonator material ultimately determine the central frequency and bandwidth of the detector. On the other hand, it is the read-out system that determines the noise level of acoustic recordings as well as the overall detector robustness. Environmental mechanical vibrations and temperature shifts are one of the biggest challenges affecting the robustness and performance of interferometric ultrasound sensors and particularly that of optical resonators. The latter case is depicted in Figure 3.14, where external disturbances can shift the resonance spectrum away from the wavelength of the interrogation laser, limiting both sensitivity and dynamic range of the detector [103].
Feedback-controlled stabilisation methods can significantly reduce the effect of external disturbances [104], e.g. by stabilising undesired optical phase shifts. Unfortunately, such feedback methods have not been successfully demonstrated in noisy environments,

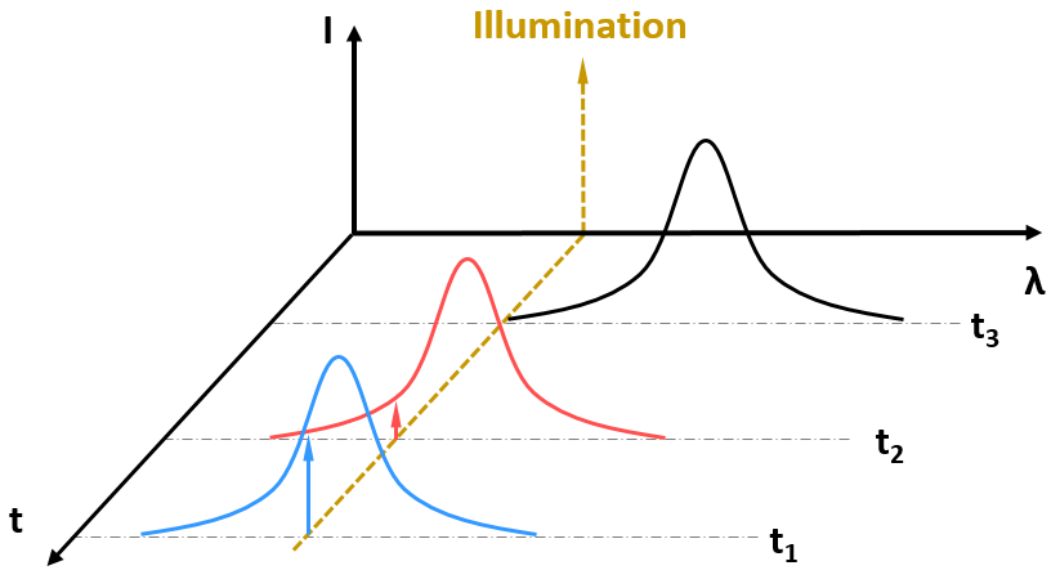

Figure 3.14: Resonator read-out with a tuneable cw-laser: (a) At time t_1, the interrogation laser is tuned to the wavelength λ_0 where resonance shifts behave approximately linear. At t_2, a spectral shift induced by ultrasound is monitored as a negative shift in intensity. At t_3, an external perturbation or a high amplitude acoustic signal induce a spectral shift that exceeds the dynamic range of the detector.

that are prevalent in clinical applications, yet. Another major disadvantage of cw-laser interrogation for resonators is the problematic scalability. In the context of optical detectors, scalability is synonymous to multiplexing and refers to the simultaneous read-out of multiple interferometric sensors, preferably by a single interrogation system. This scalability is vital for tomographic imaging applications, as it enables the creation of optical detector arrays without the need for scaling up complex and expensive components. In optoacoustic tomography, piezoelectric arrays have up to hundreds of individual detectors [2] and transferring this array design to optical resonators for example, every individual detector would then need to have its own interrogation laser and photodiode. So far, scalable cw-laser read-out is only possible for two-beam interferometers, where e.g. the individual interferometers have been tuned to the identical wavelength that in turn matches the wavelength of the interrogation laser [105]. Other approaches are based on frequency modulation techniques, such as heterodyne detection schemes [34] and frequency sweeping [106], where no optical feedback method is required, making two-beam interferometers robust compared to resonator based detectors. Figure 3.15 shows an alternative read-out method based on pulsed laser interrogation which has been recently

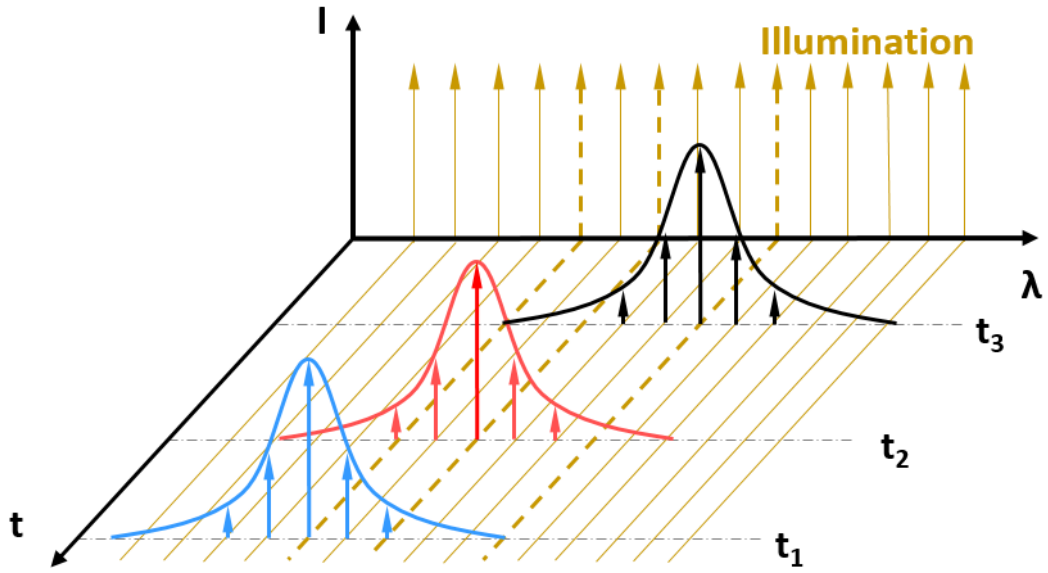

Figure 3.15: Resonator read-out with a pulsed laser: A broadband pulsed laser interrogates acoustically induced spectral resonance shifts in the resonators. A wavelength-meter or optical demodulator records the spectral shifts, enabling higher sensitivity and dynamic range. Multiple detectors with resonances within the range of the interrogation laser can read-out simultaneously via multiplexing.

developed for optical resonators [103]. Here, resonators are interrogated by optical pulses that have a significantly broader bandwidth than width of the resonance. The resonator then acts as a spectral filter, where light that exits the resonator adopts the spectral shape of the resonance. Similar to Doppler interferometry, an optical demodulator can then be used to record ultrasound-induced shifts in the resonance frequency.

Pulsed laser interrogation offers two advantages over cw-laser interrogation: Firstly, the susceptibility towards environmental noise is drastically decreased. Spectral shifts induced by temperature variations or mechanical vibrations can be filtered electronically by a high-pass filter after recording and the dynamic range is effectively only limited by the bandwidth of the applied laser pulses. Secondly, a multitude of resonators can be interrogated simultaneously, as long as the individual resonances do not overlap spectrally and are still within the bandwidth of the interrogating pulsed laser. Here, wavelength-division multiplexing techniques could be applied for the interrogation of multiple resonators via a single beam path or optical fiber [107].

As mentioned in subsection 3.4.3, the smallest detectable resonance shifts depend on the Q-factor of the resonator as well as on the noise properties of the read-out mechanism. For cw-laser interrogation, the optical signal and the noise sources have the following

interdependencies with the Q-factor Q, the laser power P and the laser linewidth $\Delta\lambda$:

$$sig \propto P \cdot Q \tag{3.12}$$

$$n_{ther} = const. \tag{3.13}$$

$$n_{shot} \propto \sqrt{P} \tag{3.14}$$

$$n_{freq} \propto P \cdot Q\sqrt{\Delta\lambda} \tag{3.15}$$

Here, sig, n_{ther}, n_{shot}, n_{freq} are the monitored signal, detector thermal noise, shot noise and frequency noise, respectively [108, 109]. The noise comparison shows that cw-laser interrogation is ultimately limited by frequency noise, meaning that at some point neither increasing the power P, nor increasing the Q-factor would improve the SNR. In order to approach such frequency noise limited SNR levels, sufficiently high laser powers and resonator Q-factors are required nevertheless.

3.5 Conclusion

In summary, advances in optoacoustic imaging increased the performance requirements for ultrasound detectors. Piezoelectric transducers, on which biomedical ultrasonography and conventional optoacoustic systems as well as the majority of NDT methods are based, are commonly opaque, large in dimension and narrowband. In contrast, the ideal detector for optoacoustic imaging is transparent to avoid interference with the excitation light, point-like to achieve a wide angular response and wideband to achieve a high imaging resolution. As a consequence, the interest has shifted away from classic detectors towards micromachined transducers and all-optical ultrasound detectors. Although micromachined transducers such as CMUTs and PMUTs have dramatically improved in performance over the past years, especially their relatively low bandwidths are not sufficient for optoacoustic tomography yet. In contrast, the miniaturization of interferometric detectors as well as their sensing subcomponents can be achieved without drawbacks in sensitivity and bandwidth. Moreover, this miniaturization as well as the transparent nature of e.g. silica based optical resonators might enable ultra-small optoacoustic sensors for minimally invasive applications such as intravascular endoscopy. Finally, novel pulsed laser read-out

methods have been demonstrated to significantly decrease environmental noise, paving the way towards intra-clinical study and application.
Nevertheless, a number of challenges remain to be solved for optical ultrasound detectors. One major hurdle is the simultaneous interrogation of multiple sensors that would allow to create detector arrays for tomographic applications. In this aspect, piezoelectric detector arrays are still unequalled. Also, the sensitivity of optical detectors needs to be further improved to be on par with large-area and focused piezoelectric elements. On the other hand, refractometric sensing methods that are based on indirect Schlieren-beam interrogation of a mirrored optoacoustic source (see Figure 3.7d) may allow real-time optoacoustic imaging without the need for detector arrays and computational image reconstruction in the future. In contrast to interferometric approaches, refractometric methods need to be dramatically improved in terms of sensitivity before they can be considered for high resolution optoacoustic imaging.
Based on the findings presented in this chapter, optical ultrasound detectors were found to have the biggest potential to serve the need for both broad bandwidth as well as sensitive detectors in optoacoustic imaging. In particular, the combination of micron-sized optical resonators and novel read-out schemes might enable optoacoustic sensing for challenging applications such as gastrointestinal or intravascular endoscopy (see section 1.2). The following chapters were therefore devoted to the application of optical fiber based π-BGs in optoacoustic microscopy (see chapter 4 and chapter 5) as well as the development of a novel optical resonator for the application in optoacoustic endoscopy (see chapter 6).

4 π-phase shifted Fiber Bragg Gratings in Optoacoustic Microscopy

4.1 Introduction

Piezoelectric ultrasound transducers are the gold standard in optoacoustic microscopy up to this day [37, 110], as piezoelectric sensors can be manufactured in acoustic focusing designs with relatively high sensitivity and bandwidth (see chapter 3). As a consequence, piezoelectric elements represent a well-established technology and complete off-the-shelf systems are readily available on the market.

Nevertheless, piezoelectric transducers exhibit a number of disadvantages for the application in optoacoustic microscopy. Firstly, for resolving fine absorbers down to the single μm level, ultrasound transducers would require a frequency response of up to 1.5 GHz. Here, the required element thickness of the piezoelectric element as well as the application of acoustic matching and backing materials onto the transducer leads into fabrication challenges [16, 53]. Secondly, the sensitivities necessary for optoacoustic microscopy are commonly achieved by focused ultrasound transducers that have focal spot sizes of few 10s of μm that require exact coalignment with the optical focus. Moreover, these focused transducers have working distances in the range of millimeters and below, imposing practical limitations on sample-handling [46, 60].

Optoacoustic microscopy has been successfully demonstrated with all-optical ultrasound detection, e.g. based on optical micro-ring resonators [65] as well as on beam deflectometry [81] (see chapter 3). While micro-rings are commonly in the order of below 100 μm in size, the substrate they are positioned on as well as the components necessary to couple the read-out laser into the resonator are commonly too bulky to be easily implemented into optoacoustic microscopes. Li et al. [65] took advantage of the transparent nature of the substrate to enable epi-illumination microscopy. With a sensitivity of around 7 Pa and a bandwidth of 140 MHz, such micro-rings appear to be a promising tool for optoacoustic microscopy. Yet, this approach requires an overall inverted microscopy

geometry that denies the application in off-the-shelf commercial microscopy systems. Moreover, the fragile nature of the micro-rings is a major hurdle for the translation into scaled up biomedical studies.
In turn, methods based on beam deflectometry (see subsection 3.4.1) do not depend on physical hardware in order to be employed close to the sample or the optical excitation setup. In the case of beam deflectometry, it is the inherently low bandwidth of less than 20 MHz that has yet prevented its widespread implementation.
An alternative optical sensing approach is presented in this chapter, where optoacoustic microscopy is demonstrated utilizing π-phase shifted FBGs ($\pi-$FBGs) as acoustic detectors. $\pi-$FBGs offer an alternative resonator based method for all-optical ultrasound detection with an ultrasmall footprint that allows for a straightforward implementation into a given microscope without affecting existing experimental frameworks such as light delivery or sample selection. While $\pi-$FBGs have already been validated to be suitable for the detection of ultrasound [62], the experiments in this chapter represent the first time that an optoacoustic microscopy setup based on $\pi-$FBG ultrasound detection was shown in an actual biomedical imaging framework. In the following, π-FBGs are successfully demonstrated in transmission-mode geometry, with a sensitivity sufficient for deep *in vivo* tissue imaging and with sensor form factors that would straightforwardly allow for subsequent implementation into optoacoustic endoscopy. The chapter is based on the experiments and findings published in [60, 111].

4.2 Materials and Methods

4.2.1 Experimental Setup

The optoacoustic microscope with transmission-mode geometry is schematically depicted in Figure 4.1 and the bulk of its components can be grouped into three sections:

1. Light generation and delivery for optoacoustic signal excitation.
2. An inverted microscope for sample alignment and brightfield microscopy imaging.
3. A read-out system that detects and records optoacoustic signals.

The optoacoustic excitation was supplied by a 515 nm passively Q-switched and diode pumped solid state (**DPSS**) laser with a fixed repetition rate of 1.2 kHz, a pulse energy of 570 μJ and a pulse width of 1.8 ns (Flare HP PQ Green 2 k-500; Innolight GmbH,

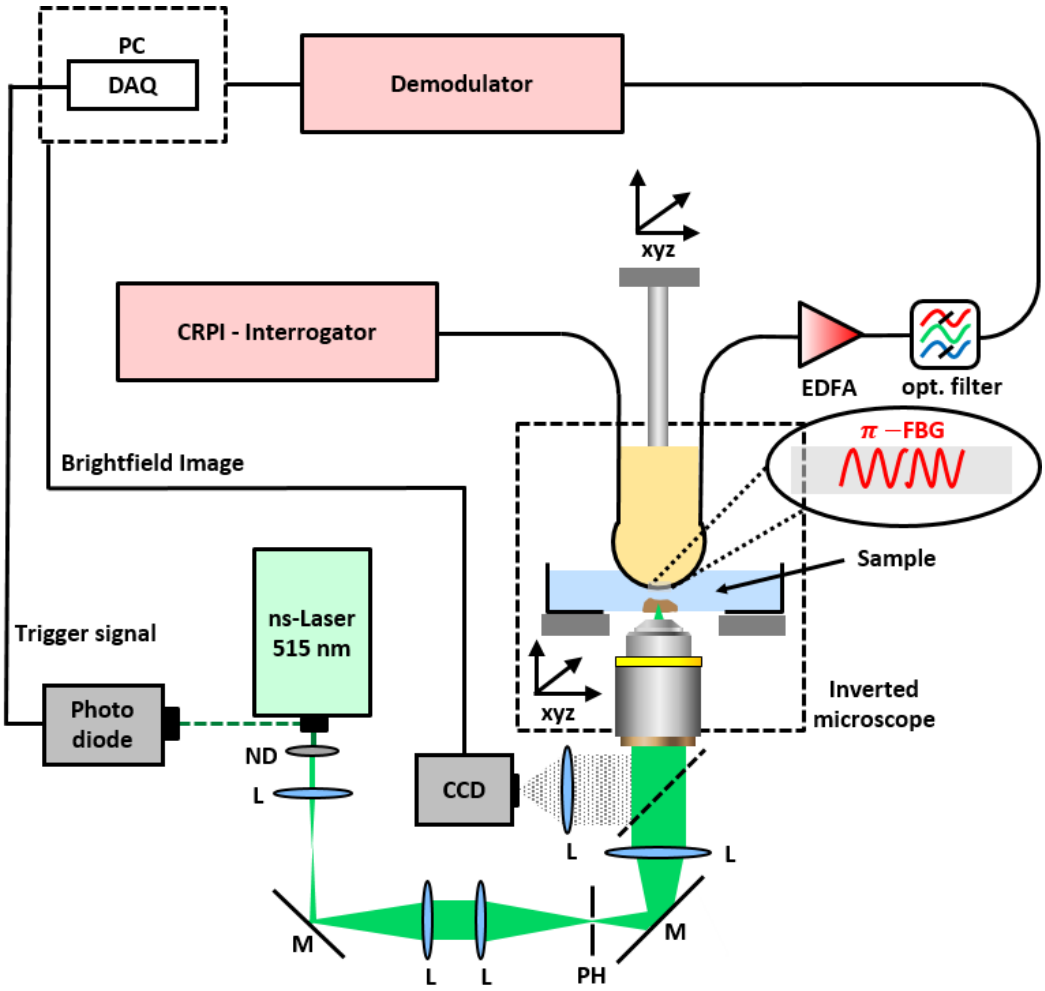

Figure 4.1: Schematic of a transmission-mode optoacoustic microscope based on a $\pi-$FBG resonator and CRPI read-out. CCD, charge-coupled device; DAQ, data acquisition card; EDFA, erbium-doped optical amplifier; ND, neutral density filter; L, lens; M, mirror; PH, pinhole; xyz, motorized translation stages.

Hannover, Germany). Stray light at the laser output was captured by a photo diode (DET 36A; Thorlabs, Newton, USA) and triggered data acquisition for optoacoustic imaging. The laser beam was attenuated by neutral density filters, resized and spatially cleaned by two telescopes with a 25 μm pinhole at the focal spot and guided to a customized inverted microscope (AxioObserver.D1; Zeiss, Jena, Germany) with a standard spinning-top set of 90 degree mirrors that allowed for on-the-fly transition between brightfield and optoacoustic microscopy. The diameter of the resized beam was set to around 15 mm as to overfill the back aperture of the microscope objective (PLN 10x; Olympus, Hamburg, Germany) and to approach a diffraction limited focal spot size. The objective had a

long working distance (**WD**) of 10.6 mm and a corresponding low numerical aperture (**NA**) of 0.25. The theoretical spatial resolution of the setup can be determined with the equations given in subsection 3.4.3. The lateral resolution is then governed by the applied objective and achieved $\approx 2.2\ \mu m$. The axial resolution was determined after bandwidth characterization of the $\pi-$FBG and estimated to be around 11 μm.

The inverted microscope allowed for brightfield microscopy with integrated image acquisition by an embedded CCD camera (AxioCam ICc1; Zeiss, Jena, Germany). Due to limitations in the space above the sample holder introduced by an additional xyz-set of translational stages, the off-the-shelf illumination for brightfield microscopy was replaced by an extractable white light LED installed atop the sample plane as needed. The focal plane of the objective was arranged to match various sample planes, e.g. samples placed on thin microscopy slides ($\sim$ 1 mm thickness), standardised microscopy cover slips (170 μm thickness) or common glass bottom Petri dishes (170 μm thickness). The respective sample holders were custom-made and mounted onto an xyz-set of integrated high-precision piezoelectric linear stages with a minimum step size of 0.1 μm (xy-stage: MLS203-2, z-stage: ZMZS500-E; Thorlabs, Newton, USA). Samples were fixed either by water-proof tape or embedded inside a volume of agar and restrained by an optically transparent and 20 μm thick polyethylene foil. Acoustic attenuation by the foil was found to be negligible at the investigated frequencies. For acoustic coupling with the ultrasound detector, the sample was then covered with water droplets or - in the case of Petri dishes - filled with 8 - 10 ml of distilled water.

The acoustic detector is depicted in Figure 4.2 and ultrasound sensing was performed by a $\pi-$FBG (TeraXion Inc., Quebec, Canada) that was mounted on a custom-made 3D-printed holder. Magnetic fiber clamps (T711/M-250; Thorlabs, Newton, USA) were fitted flush into the holder flanks and kept the fiber positioned at the center of an embedded aperture. This aperture prevented acoustic reflections at the holder surface that would have otherwise perturbed the $\pi-$FBG and caused parasitic signals. The diameter of the holder was chosen to be smaller than the diameter of the respective water-tank or Petri dish in order to allow for precise lateral alignment of the $\pi-$FBG relative to the optical focus in the sample as well as to locate it as close as possible to the sample. The axial and lateral alignment of the $\pi-$FBG and its holder was performed by an xyz-set of linear stages (xy-stage: PI M-683, z-stage: PI-M-501; Physik Instrumente, Karlsruhe, Germany) that were mounted independently of the inverted microscope and atop the sample holder. The optical interrogation and corresponding demodulation systems were installed on separate optical tables away from the microscopy setup in order

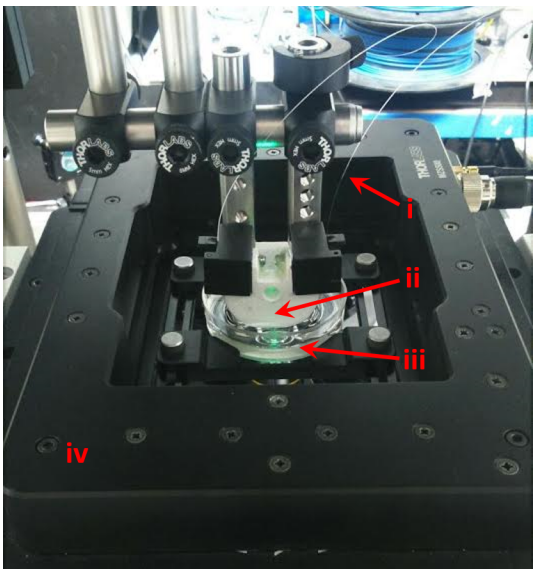

Figure 4.2: Photograph of the $\pi-$FBG installed atop an inverted microscope in transmission-mode geometry: i) optical fiber link; ii) 3D printed $\pi-$FBG mount; iii) Petri dish and sample mount; iv) motorized xyz translation stage.

to avoid electromagnetic interference between the DPSS driver, the interrogation laser, the adjacent optical amplifiers as well as the employed high bandwidth photodiodes. The interrogation and demodulation systems are discussed in more detail in section 4.3.

4.2.2 Data Acquisition and Image Processing

The demodulator converted spectral shifts to a voltage readout that was in turn recorded by a 12-bit high speed data acquisition card (**DAQ**) (1.0 GS/s GAGE CS121G2; DynamicSignals, Lockport, USA) upon a trigger signal coming from the excitation laser. When performing OAM imaging, the motorized xyz-translation stages moved a given sample through the focal spot of the optical excitation beam. Depending on the relevant measurement, the sample was moved along a line (1D) or in a raster-pattern (2D) with an adjustable resolution and step size. The laser triggering, individual stage movements as well as signal acquisition were performed by custom MATLAB scripts and the subsequent image processing was executed by MATLAB and ImageJ. For smooth appearance and enhanced contrast, images were additionally processed with de-speckle and Gaussian blur.

For 2D microscopy imaging, the sample was scanned over the xy plane in level of the optical focus and time-resolved ultrasound signals (A-scans) were recorded at each step.

These signals were then averaged on demand and filtered by a high-pass frequency filter for noise reduction, typically starting above 5 MHz. It is relevant to note that EM noise was initially induced in the feedback controller of the read-out system as well as in the coaxial wiring between the photodiode and the DAQ card. Through selective shielding and iterative tests, the DPSS excitation laser as well as the high-voltage drivers of the xyz-stages were identified as main sources for the EM noise and relevant components were shielded accordingly.
An exemplary scan for optoacoustic signal recording is shown in Figure 4.3.

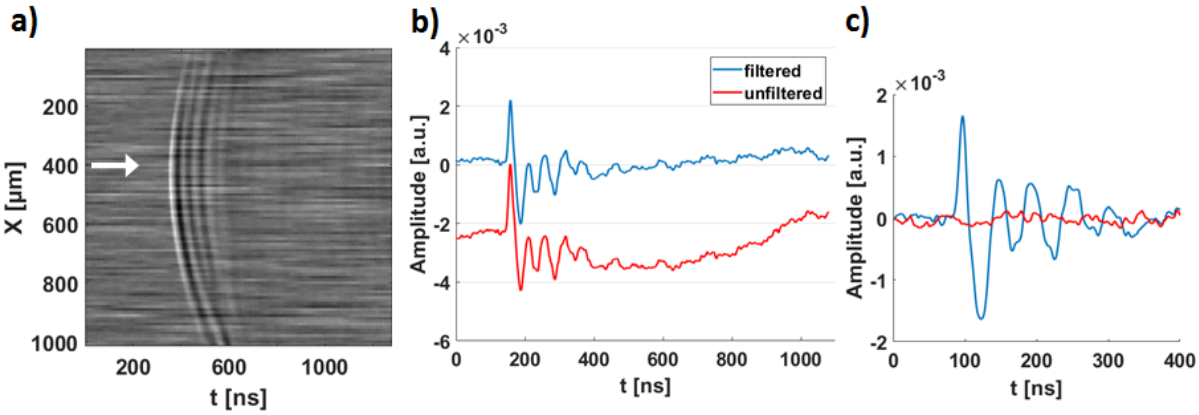

Figure 4.3: Data acquisition and signal processing: (a) Unfiltered B-scan of an optoacoustic point source acquired perpendicular to the cylindrical axis of the π-FBG. (b) Unfiltered (red) and filtered (blue) A-scan of the signal indicated by a white arrow in (a). (c) Close-up of the acoustic signal (blue) and a corresponding noise recording (red) for SNR analysis.

Here, optoacoustic signals were generated by directing the focused beam onto a strongly absorbing black acrylic paint phantom and the π−FBG was scanned above the focal spot along the x-axis and perpendicular to its cylindrical geometry. The continuous scan along the x-axis (B-scan) is shown in Figure 4.3a, where the recorded signals are not frequency filtered yet. Note that already these projections reveal important information about the imaging procedure, such as the distance between the detector and the absorber as well as the existence of artefacts, such as acoustic reflections or geometry-induced ringing in the acoustic detector. The latter will be discussed in more detail in section 4.6. The white arrow indicates the exemplarily chosen A-scan that is depicted in Figure 4.3b. Here, the original signal is depicted in red and the signal with an applied bandpass filter between 5 MHz and 100 MHz is depicted in blue, respectively. Figure 4.3c shows a frequency filtered close-up of the same acoustic signal in blue and a corresponding noise recording in red. While further analysis revealed a SNR of 16.5 dB for this recording, it is important

to note that such a relatively high SNR was only achieved under ideal circumstances, such as a highly absorbing source, an illumination with light intensities exceeding the ANSI limit (see section 8.1) as well as a close proximity to the sensing π-FBG.

4.3 Optical Read-Out

In the presented optoacoustic microscopy setup, a $\pi-$FBG was applied for the detection of ultrasound signals. As noted in chapter 3, the unique feature of $\pi-$FBGs is their ultra-narrow transmission resonance as seen in the recorded spectrum depicted in Figure 4.4.

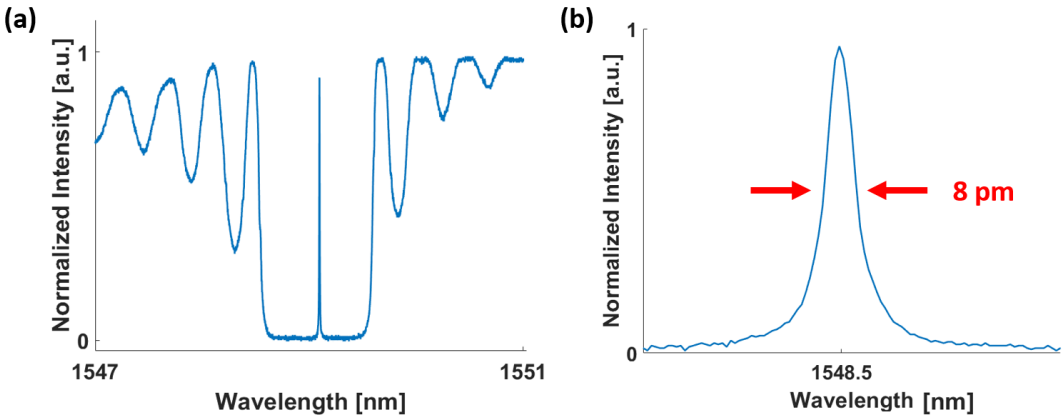

Figure 4.4: $\pi-$FBG transmission spectra: (a) Transmission spectrum of the $\pi-$FBG spanning the complete bandgap. (b) Close-up of the resonance notch with a central frequency of 1548.5 nm and a resonance width of 8 pm at the FWHM.

Here, the broad shoulders of the bandgap are seen with oscillating reflectance on either side of the centered resonance notch. In particular, the resonance spectrum depends on the grating period Γ, the grating length L of the π-phase shifted grating, the refractive index n of the optical fiber housing the Bragg grating as well as on the coupling coefficient κ. The corresponding reflection and transmission spectra as well as the amplitude of the optical field within the grating have been calculated and simulated in [112], but are not relevant for the actual application as ultrasound detector. In contrast, the slope of the resonance - and therefore its FWHM - is a hallmark for the sensitivity of π-FBGs towards acoustic perturbations. The FWHM can be deduced from the reflection spectrum and for $\kappa L \ll 1$, it is given by [62]:

$$\Delta k = 4\kappa \, \exp(-\kappa \, L) \tag{4.1}$$

The spectral characterization of the $\pi-$FBG was performed with a separate setup as

shown in Figure 4.5. Here, a tuneable cw-laser (INTUN TL1550-B; Thorlabs, Newton, USA) was installed with a tuning range in the C-Band of about 1520 nm to 1630 nm and a maximum power output of 20 mW. The laser interrogated the $\pi-$FBG via an in-line fiber setting, where the cw-laser was coupled to the $\pi-$FBG through a fiber isolator to avoid reflactions and back scatter into the laser and was subsequently coupled to switchable gain photodiode, set to 150 MHz bandwidth (balanced amplified photo detector, PDB450C; Thorlabs, Newton, USA). The cw-laser was then successively tuned through a spectrum ranging from 1547 nm to 1551 nm and the transmitted intensity was digitized and recorded by a data acquisition interface (NI SCB-68; National Instruments, Austin, USA).

With an overall grating length of 2.38 mm, the $\pi-$FBG displayed a bandgap span of 1.38 nm and a resonance width of around 1 GHz, corresponding to 8 pm at the FWHM. The central frequency of the resonance notch was determined at 1548.5 nm wavelength and the recorded spectrum as well as a close-up of the characteristic resonance-notch are shown in Figure 4.4.

For the application in optoacoustic microscopy, the optical interrogation system for the $\pi-$FBG was realized in a transmission-mode setting. Here, the setup consisted out of a pulsed laser and an adjacent Fabry-Pérot interferometer for coherence restoration as well as an Mach-Zehnder interferometer for frequency demodulation. The concept of pulsed interferometry interrogation (**PI**) is depicted in Figure 4.6a, where an ultra-fast femtosecond laser (TC-1550 M-comb; Menlo Systems GmbH, Martinsried, Germany) in the C-Band with a central wavelength of 1550 nm and a repetition rate of 250 MHz was applied. The comb structure of the mode-locked fs-laser has a broad spectral width in the frequency domain and hence allows for a higher dynamic range of a resonator based acoustic detector than when applying a common cw-laser interrogation method. Parallel to the setup, a 1 % observation output of the fs-laser was connected to a photodiode for constant power monitoring (not depicted in Figure 4.6a). The main 99 % output was spectrally filtered by a passive narrow bandpass filter of 0.4 nm bandwidth, then amplified by an erbium-doped optical (fiber) amplifier (**EDFA**) and subsequently filtered

Figure 4.5: Transmission-mode spectral characterization setup for $\pi-$FBGs.

by another 0.4 nm bandpass filter. The two filters were applied for the reduction of noise due to amplified spontaneous emission (**ASE**) of the fs-laser and the optical amplifier in the C-Band.

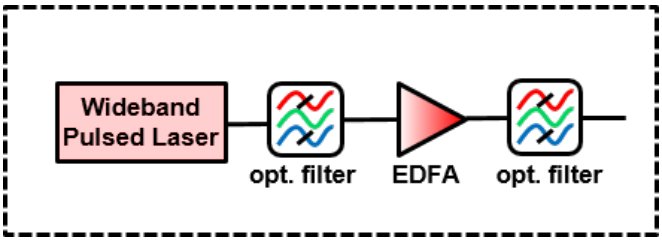

(a) Pulse interferometry (PI) interrogation.

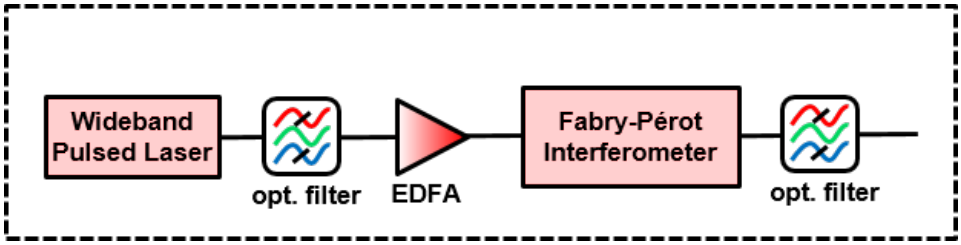

(b) Coherence restored pulsed interferometry (CRPI) interrogation with implemented FP interferometer.

Figure 4.6: Interrogation layouts for $\pi-$FBG resonators. EDFA, erbium-doped optical amplifier.

Coherence restored pulsed interferometry (**CRPI**) is depicted in Figure 4.6b and is based on the identical setup of fs-laser, optical amplifier and bandpass filters as the PI system. However, a free-beam FP interferometer (custom made optical frequency synthesizer; Menlo Systems) was added to the setup directly after the amplification by the EDFA. This resonator acted as an additional spectral filter for the rejection of ASE noise and has been labeled as coherence restoring filter (**CRF**) by Rosenthal et al. [24]. The FP had a narrow transmission spectrum that - depending on the cavity length of the FP - may partially or fully coincide with the comb structure of the pulsed fs-laser. ASE noise that accompanies the comb-structure of the fs-laser and which occurs in the spectrum between the individual combs is then filtered out by the FP. Here, the FP had a FSR of 1 GHz, corresponding to a repetition rate of 1 GHz of the pulsed laser at the FP output. Drifts in the spectrum that were inevitably induced in the Hz and kHz-regime by environmental vibrations or temperature shifts, were tackled by a wideband feedback circuit and an embedded piezoelectric element which adjusted the FSR of the FP accordingly [104].
In the following experiments, interrogation was solely performed by the CRPI and further discussion about pulsed interferometry, CRF noise reduction as well as about the

applied feedback circuit can be found in chapter 3 and references [17, 24, 103, 104, 113], respectively. In the optoacoustic microscopy setup, the combined CRPI source (as depicted in Figure 4.6b) then interrogated the $\pi-$FBG and lead to the adjacent optical read-out system as illustrated in Figure 4.7. Here, the spectrally shifted interrogation pulses were amplified by another EDFA and spectral noise was filtered by a narrow bandwidth spectral filter of 0.4 nm width. In order to translate the spectral shifts into intensity shifts and therefore into voltage signals that could be observed and recorded, the signal was coupled into an active demodulation scheme. The applied demodulator or wavelength-meter was a fiber-based Mach-Zehnder interferometer with its two optical outputs coupled into a balanced photodiode (PDB450C; Thorlabs) [24]. Perturbations in the voltage read-out of the balanced photodiode then corresponded to ultrasound-induced perturbations of the resonance condition of the $\pi-$FBG and were recorded by a data acquisition card as described in subsection 4.2.2.

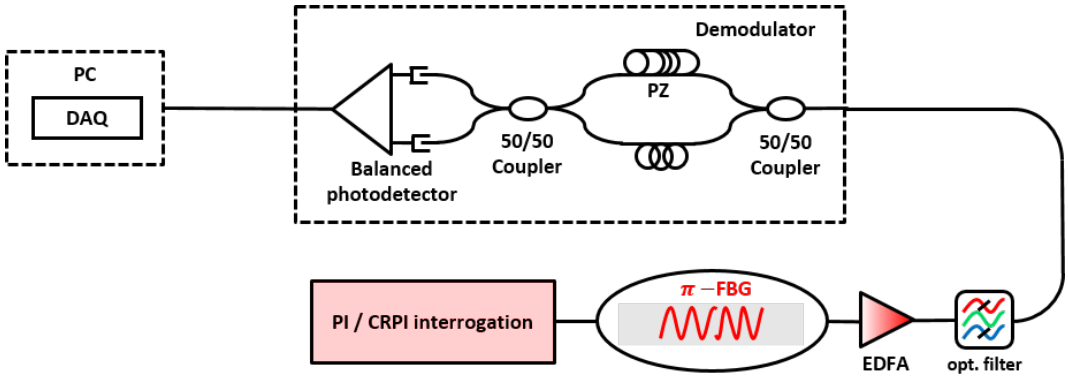

Figure 4.7: Transmission-mode $\pi-$FBG read-out and spectral demodulation. DAQ, data acquisition card; EDFA, erbium-doped optical amplifier; PZ, piezoelectric fiber-stretcher.

4.4 System Characterization

4.4.1 Sensitivity

In general, the sensitivity of the optical resonator was determined by the ability of the $\pi-$FBG to convert ultrasound-induced mechanical vibrations into spectral shifts. In the context of the introduced optoacoustic microscope, this corresponds to the ability of the combined $\pi-$FBG and CRPI system to record optoacoustic signals e.g. from concentrations of optical absorbers such as hemoglobin in micro-vasculature of the dermal

vascular-plexus. The sensitivity of the combined $\pi-$FBG and CRPI system corresponds to 0.1 kPa in terms of NEP (see chapter 3) and was first demonstrated by Rosenthal et al. [24]. In order to demonstrate the sensitivity field of the $\pi-$FBG, it was scanned across a fixed optoacoustic source, which was provided by the optoacoustic microscopy system focusing onto a thin layer of black varnish. The signals recorded for the line scans across the source are depicted in Figure 4.8, with the $\pi-$FBG installed in a way as to be oriented in parallel or perpendicular to the stage movements, respectively. Here, the scans allowed to correct for askew mounting of the sensor holder and confirmed the effective length of around 300 μm of the detector [103] (see Table 3.4). The combination of Figure 4.8a and Figure 4.8b shows, how an orthographic set of line scans allowed to correct for spatial offsets between the $\pi-$FBG and the focus of the optoacoustic microscope. In particular, the y-scan accentuated the cylindrical nature of the detector, with acoustic signals traversing for a longer time through the coupling medium to reach the center of the $\pi-$FBG than the signals in the x-scan. In the latter, acoustic signals affected the resonance condition of the BG throughout its length.

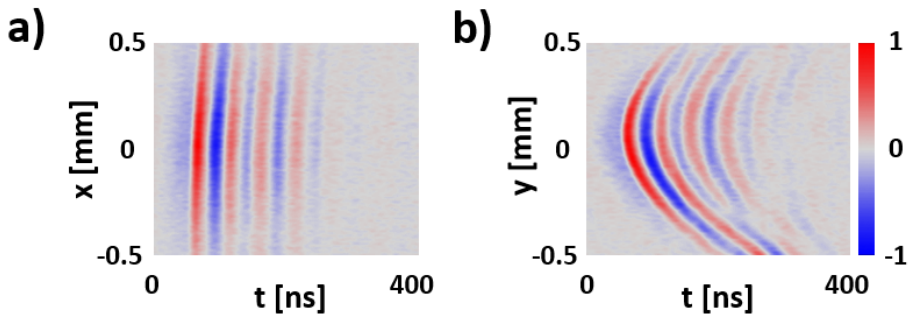

Figure 4.8: Optoacoustic signals from line scans across a steady point source: a) $\pi-$FBG scanned in parallel to its geometrical axis. b) $\pi-$FBG scanned perpendicular to its geometrical axis.

4.4.2 Frequency Response

The bandwidth of the system was determined by utilizing a well-established phantom as optical absorber: A 10 μm black polystyrene sphere (Polybead; Polysciences, Warrington, USA) was embedded in an agar matrix and optoacoustically excited with the 515 nm laser as described in subsection 4.2.1. Due to its ultra-small size, optoacoustic signals from the sphere have a broad frequency content spanning more than 300 MHz (see chapter 2), which exceeded the frequency response of the $\pi-$FBG by far and thus allowed to get a precise measure of the detector bandwidth. For the measurement, the sphere was scanned

through the optical focus of the microscope objective with a step size of 0.5 μm and the recorded time-resolved signals were plotted in a MIP as depicted in Figure 4.9a. The size of the sphere as imaged in this MIP corresponds well to the convolution of the sphere size and the focal spot diameter that defines the resolution. An acoustic signal in the time domain of a point at the center of the sphere is depicted in Figure 4.9b. The Fourier transform of this acoustic signal then revealed the frequency response of the $\pi-$FBG and is shown in Figure 4.9c. Here, the peak sensitivity is reached for acoustic signals with a central frequency of around 20 MHz. The overall frequency response can be segmented into two separate bands following the common -6 dB convention, with the first band between 7 MHz and 27 MHz and the second band between 62 MHz and 77 MHz.

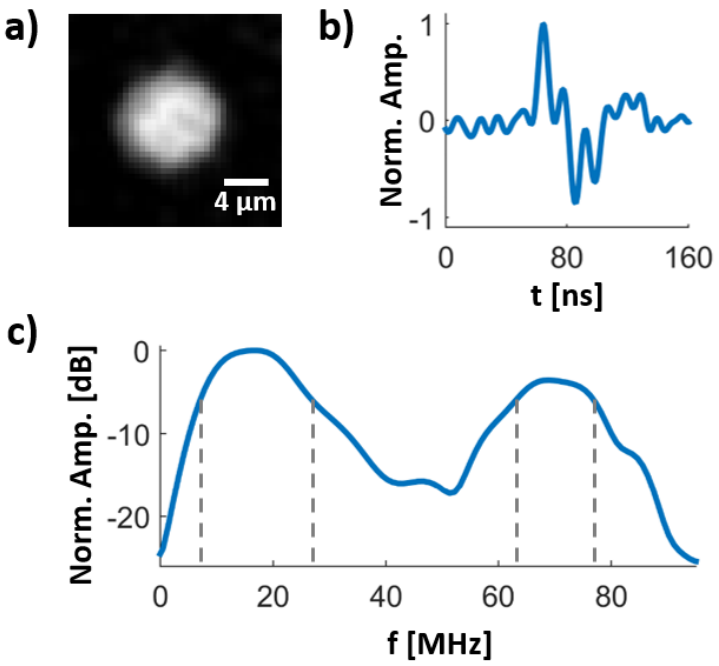

Figure 4.9: Bandwidth characterization of the $\pi-$FBG: (a) MIP of a 10 μm polystyrene micro-sphere. (b) Optoacoustic signal selected from a central scanning point of the sphere. (c) Bandwidth of the CRPI system width two separate bands at -6 dB indicated by dashed lines (7-27 MHz and 62-77 MHz).

The separation of the frequency response into two bands is caused by the fiber-based cylindrical geometry of the $\pi-$FBG. Acoustic signals traversing through the resonator with wavelengths corresponding to resonant frequencies of the fiber-diameter lead to this cancellation. Accordingly, also the mismatch in acoustic impedances leads to a frequency-dependent reflection of the impinging acoustic signals. Both phenomena have been discussed and illustrated in more detail by Veres et al. [114].

4.4.3 Spatial Resolution

The lateral resolution of the setup is governed by the focusing ability of the employed microscopy objective and the divergence of the collimated laser beam that was coupled into it. By proper adjustment and fine tuning of the beam collimation over a distance of around 3 meters before coupling it into the microscope, the divergence was negligible. For the microscope objective with 10x magnification and a NA of 0.25, the optical focus was then found to be around 2.2 μm. The axial resolution of a microscopy setup is determined by the bandwidth of the applied ultrasound detector (compare subsection 3.4.3). Accordingly, the axial resolution for the $\pi-$FBG system was found to be in the order of 11 μm, considering a bandwidth spanning over both bands of the frequency response. As hinted in subsection 3.4.3, this is around six times smaller than the optical depth-of-focus of around 60 μm (see Equation 2.19) of the microscope objective. The axial resolution was therefore found to be governed by the bandwidth of the system as expected (see chapter 3).

4.5 Experiments and Results

The idea to first apply the π-FBG in an optoacoustic microscopy setup was based on the assumption that the technical parameters in microscopy - such as optical working distance and fluence - are similar to the ones achievable in other applications such as microvascular endoscopy. Moreover, the implementation allowed for a direct comparison between the performance of the $\pi-$FBG and highly sophisticated piezoelectric ultrasound transducers that are commonly applied in transmission-mode optoacoustic microscopy setups with acoustic focusing [46].

4.5.1 Phantom Experiments

Phantoms made from tinted surgical sutures are well established in optoacoustic imaging because of their well-defined diameter and strong optical absorption. For the $\pi-$FBG setup, a suture phantom was created with sutures of 10 μm, 20 μm and 30 μm in diameter (Dafilon Polyamide; B. Braun, Melsungen, Germany). The sutures were attached to the bottom of a glass-bottom Petri dish by adhesive tape and adjusted in the form of a triangle. The scanning step size was set to 5 μm, the FOV to 500 μm x 500 μm and the pulse energy of the excitation laser to around 15 nJ. In a first measurement, the phantom was scanned by the $\pi-$FBG as described above and in the second measurement,

a spherically focused piezoelectric transducer was applied, with a bandwidth of 100 MHz, 78 MHz central frequency and a working distance of 1.8 mm (Sonaxis; Besancon, France). In the case of the piezoelectric transducer, a low-noise electrical amplifier with a gain of 63 dB was applied (AU 1291; Miteq, New York, USA). The recorded MIPs are depicted in Figure 4.10a and Figure 4.10b, respectively.

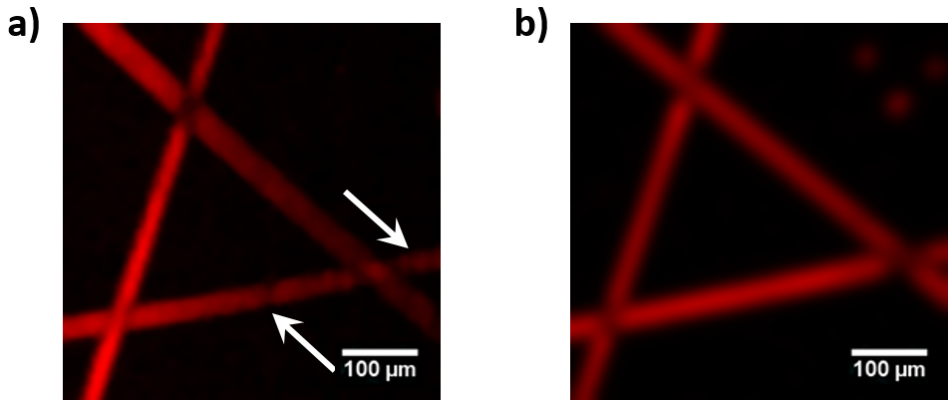

Figure 4.10: Optoacoustic microscopy images of a suture phantom: (a) MIP recorded by the $\pi-$FBG. (b) MIP recorded with a spherically focused piezoelectric ultrasound transducer. Surgical sutures with respective diameters of 10 μm, 20 μm and 30 μm. White arrows indicate inconsistencies in the $\pi-$FBG scan.

This initial direct comparison already revealed a promising performance of the $\pi-$FBG despite of continuing decline in sensitivity throughout the scan. It was found that stray light of the excitation laser heated the $\pi-$FBG and its holder, leading to fluctuations in resonance and a decrease in its dynamic range. Representative positions in the MIP at which the dynamic range as well as the resulting system SNR were diminished, are marked by white arrows in Figure 4.10a. Note that the scans were performed vertically - along the y-axis - as reflected by the linear shape of the inconsistencies. To avoid such noise in the succeeding experiments, the 3D-printed sensor holder was redesigned and equipped with an enlarged aperture atop the $\pi-$FBG in order to avoid thermal fluctuations by scattered light in its immediate surroundings.

4.5.2 Ex vivo experiments

In transmission-mode microscopy geometry, optoacoustic imaging needs to be performed on thin samples, such as inorganic suture phantoms or dermal *ex vivo* and *in vivo* samples [115]. In the case of thin tissue samples, where hemoglobin in red blood cells acts as optical absorber, mouse ears are a common experimental subject due to its delicate

vasculature branching out over an area of around 1 cm^2 as well as due to inherent vessel diameters ranging between single micrometers and hundreds of micrometers.

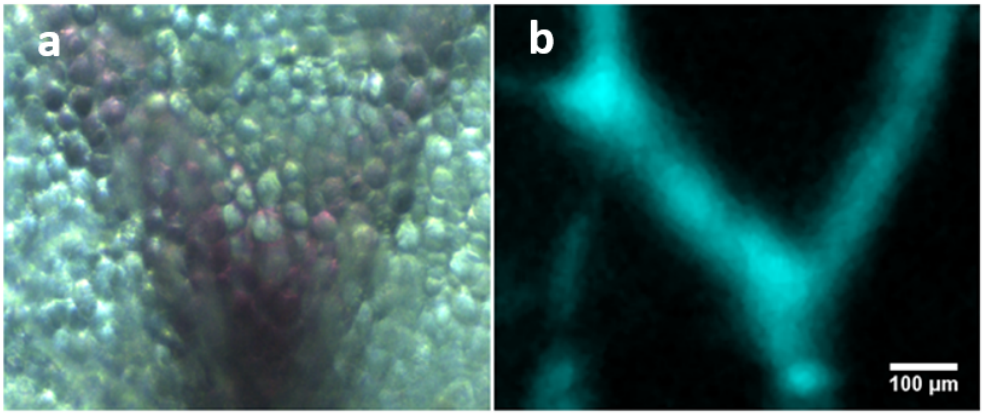

Figure 4.11: Optoacoustic microscopy image of an *ex vivo* mouse ear: Bright-field microscopy image (a) and optoacoustic MIP (b) of an excised mouse ear indicating subcutaneous vasculature and supplementary contrast.

For the first *ex vivo* experiments, mouse ears were excised from depilated nude mouse strain immediately after sacrifice and fixated onto a 60 mm glass-bottom Petri dish with thin PE-foil. Acoustic coupling was provided by centrifuged ultrasound gel between sample and PE-foil as well as by deionized water in the Petri dish for coupling with the $\pi-$FBG. The scanning step size was set to 5 μm, the FOV to 700 μm x 500 μm and the pulse energy of the excitation laser to around 15 nJ. The brightfield image as well as the optoacoustic MIP are depicted in Figure 4.11 and a Y-shaped vascular branch can be seen in either image. In contrast to the brightfield image though, the optoacoustic image reveals smaller vasculature in the bottom left side of the MIP, demonstrating the complementary contrast of this imaging modality. While the bright-field image is sharp and reveals the superficial dermal structure, the foci of the two imaging modalities were not fully coaligned and the MIP was recorded with the excitation beam slightly out of focus, leading to an overall diffuse optoacoustic image. To correct for this, the foci were realigned for the following experiments by slightly decreasing the divergence of the excitation laser before entering the objective.

For the following experiment, the mice ears were prepared as described above and additionally cauterised after excision in order to prevent blood and lymph from draining off. The scanning step size was set to 5 μm, the FOV to 600 μm x 600 μm and the pulse energy of the excitation laser to around 100 nJ. The raise in pulse energy was necessary to penetrate the tissue at a depth of around 100 μm with the realigned focus. Figure 4.12a

shows the MIP without post-processing along with its corresponding color map. The bright-field image is depicted in Figure 4.12b and sporadically reveals vasculature that was not obscured by tissue. Vessels with diameters of 10 μm to 20 μm are only revealed in the optoacoustic MIP in Figure 4.12c though, where a coherent structure between overlapping arteries and veins can be seen. These parts are indiscernible in the bright-field image and again highlight the complementary contrast of this hybrid imaging method. The side-view MIP of the identical volume of scans is depicted in Figure 4.12d, revealing a levelled vasculature at the center of the mouse ear over a thickness of around 50 μm. The bottom of the Petri dish was oriented on the right side of the image, confirming that the ear was fixated evenly onto its surface. The overall thickness of the volume over which the MIPs were recorded was 140 μm, defined by windowing the optoacoustic signals in the time domain, correspondingly.

Zebrafish are another well-established *ex vivo* sample for photoacoustic imaging due to the prominent dark melanocytes in their tissue [37, 116]. These melanocytes absorb very strongly, especially in the range of 515 nm as applied in the experiment. After sacrifice, zebrafish larvae with overall lengths ranging from 1 mm to 1.5 mm were mounted on Petri dishes in a similar way as the mice ears. For image acquisition, the step and the FOV were set to 5 μm and 600 μm x 600 μm, respectively. The laser pulse energy was decreased to around 16 nJ, due to the strong optical absorbency of melanocytes in the applied wavelength (see Figure 2.4). Figure 4.13a shows the resulting MIP recorded at the center of a zebrafish larva without post-processing. The bright-field image is depicted in Figure 4.13b with the zebrafrish torso discernible in the top left as well as the torso transitioning towards the larva tail. Note that the dotted lines correspond to the sidelines on either side of the larva as well as to its dorsal line. Figure 4.13c then shows the MIP recorded from the same area of the larva, revealing a strong structural conformity to the bright-field image. Moreover, the lower sideline appears slightly diffuse as it has been excited at an out-of-focus depth. The side-view MIP of the identical volume is depicted in Figure 4.13d, revealing an overall thickness of the larva of more than 150 μm in the upper part of the image. Additionally, the top right section of the image reveals the dotted sideline of the larva atop the glass bottom. Consequently, the blurred opposing sideline was out of focus and located closer to the $\pi-$FBG with the excitation laser focusing through the body of the zebrafish. The overall thickness of the volume was again windowed to around 140 μm.

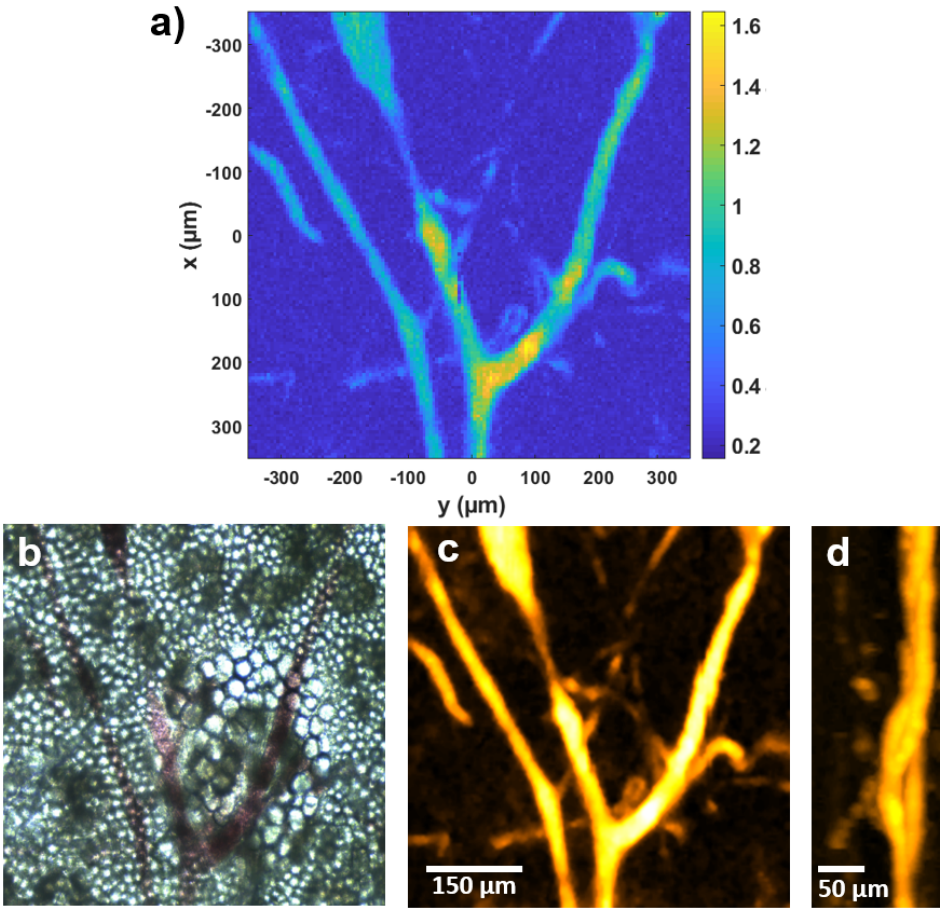

Figure 4.12: Advanced optoacoustic microscopy image of an *ex vivo* mouse ear: (a) Optoacoustic top-view MIP of the mouse ear revealing paired and branched arterial and venous vasculature with diameters ranging from 10 μm to 100 μm. (b) Bright-field microscopy image and (c) optoacoustic top-view MIP of the sample with parts of the vasculature only discernible in the optoacoustic image. (d) Optoacoustic side-view MIP of the sample over a thickness of around 140 μm.

4.6 Conclusion and Discussion

The parameters defining the performance of an all-optical ultrasound detector have been discussed in section 3.1 and it was shown that especially in the framework of optical resolution optoacoustic microscopy, the combination of sensitivity and bandwidth are of particular importance. Here, micron sized absorbers create acoustic signals with a central frequency in the range of 100s of MHz and even for ultrasound detectors with a sensitivity (in terms of NEP) in the range of single Pa, this sensitivity is of no avail if the frequency response of the respective detector is in the range of few MHz. With a sensitivity of around 100 Pa, the $\pi-$FBG is not as sensitive as e.g. micro-ring based optical resonators

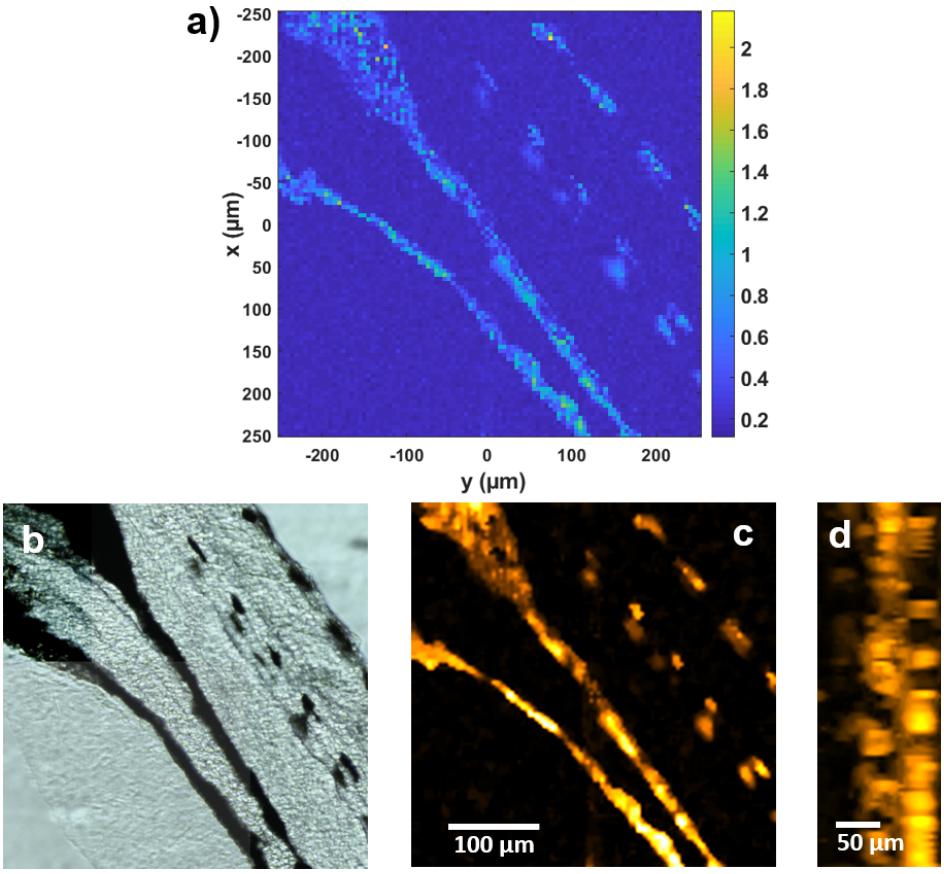

Figure 4.13: Optoacoustic microscopy image of an *ex vivo* zebrafish larva: (a) Optoacoustic top-view MIP of the sample recorded at the trunk of the larva with dotted sidelines and dorsal line. (b) Bright-field microscopy image and (c) optoacoustic top-view MIP of the zebrafish revealing a high structural conformity between the two modalities. (d) Optoacoustic side-view MIP of the sample over a thickness of around 140 μm.

and focused piezoelectric transducers that have sensitivities in the scale of single Pa. On the other hand, the sensitivity of the $\pi-$FBG exceeded that of a piezoelectric detector of a similar size by far. A 15 MHz ultrasound transducer for intravascular imaging (IVUS 15 MHz; Boston scientific, Boston, USA) was tested for comparison and only showed a sensitivity of 1.8 kPa at 16 MHz bandwidth [60]. Consequently, the $\pi-$FBG exhibits a sensitivity that is 18 times higher than that of the IVUS, although its effective detector size is 5.3 times smaller.

The experiments also showed that the sensitivity of the $\pi-$FBG was achieved over a broad frequency response. Here, the bandwidth of the system depended on various factors as described in chapter 3 [60]: For instance, the Nyquist frequency of the interrogating

laser pulses corresponded to a theoretical bandwidth of 500 MHz at the output of the CRF (FP) resonator. Additionally, the electronic bandwidth of the read-out system was governed by the 1.0 GS/s DAQ-card as well as by the response of the employed balanced photodiode with a Nyquist frequency of 75 MHz. Correspondingly, the first band (7 to 27 MHz) represents the pure mechanical response to ultrasound signals of the $\pi-$FBG and the second band (62 MHz to 77 MHz) was affected by the bandwidth restriction of the balanced photodiode, effectively limiting the overall frequency response of the system. This factor was considered in subsequent experimental setups, where balanced photodiodes with ultra-high bandwidths of up to 1.5 GHz were employed. Analysing the frequency response further, it became apparent that the M-shaped bandwidth was created by destructive interference of the acoustic waves inside the fiber, cancelling the respective acoustic frequencies centered at around 45 MHz with another descent at its multiple at around 90 MHz. Here, the speed of sound in fused silica (quartz) is around 5570 $\frac{m}{s}$ [117], corresponding to a wavelength of around 123 μm, which is in good agreement with the diameter of the fiber cladding of 125 μm of the fibers applied for $\pi-$FBG manufacture (PM SMF-28; Corning Inc., New York, USA).

In conclusion, the demonstrated optoacoustic microscope showed biological samples recorded with a $\pi-$FBG for the first time ever and demonstrated optoacoustic images of a quality that is on par with current state-of-the-art systems based on other detector technologies [9, 118]. Despite being less sensitive than other optical sensors, its ultra-small footprint and side-looking geometry is highly attractive for intravascular and gastrointestinal endoscopic imaging modalities. As will be shown in more detail in chapter 5, the small footprint also enables new detection geometries, allowing for a transition towards optoacoustic reflection-mode microscopy. To advance the system further, a number of aspects need to be improved. A major aspect is the acoustic impedance mismatch between water and the silica based detector that might be mitigated by polymer waveguides to avoid coupling losses. Another aspect is the complexity of the interrogation system, allowing to read out only one resonator at a time. Here, a solid multiplexing approach needs to be implemented, e.g. based on frequency-division multiplexing, in order to compete with prevalent multi-element piezoelectric sensor arrays.

5 Multimodal Epi-Illumination Optoacoustic Microscopy

5.1 Introduction

Optoacoustic microscopy has a number of challenging demands on the performance of the applied ultrasound detectors as well as on the geometry of the setup. Here, detector sensitivity as well as frequency response need to match the nature of weak optoacoustic signals originating from micron-sized absorbers, preferably while not affecting other existing imaging modalities in a given microscopy setup, such as classic fluorescence or multiphoton microscopy. Another key challenge in crammed and sophisticated hardware environments is to implement optoacoustic imaging as an additional modality and to simultaneously excite and monitor optoacoustic signals in a micron-sized voxel. Hence, optoacoustic microscopy systems are commonly designed in a transmission-mode geometry, where light delivery and acoustic monitoring are performed from separate sides of the sample [31, 40, 46]. Note that also the concept and application of π-FBGs in optoacoustic microscopy was first demonstrated in transmission-mode, as discussed accordingly in chapter 4.

However, this design geometry limits imaging mostly to *ex vivo* specimen with a thickness not exceeding hundreds of μm, such as excised tissue samples [60, 118], pathological samples [119] or the well-established zebrafish larvae [31, 46]. As the sample needs to be in close proximity to both the illuminating microscope objective as well as to the ultrasound detector in order to grant the application of high NA objectives and to avoid the attenuation of high acoustic frequencies in the coupling medium, transmission-mode geometries might seem favourable. As discussed in chapter 3, established piezoelectric ultrasound transducers also need to be enlarged to achieve high sensitivities, rendering their footprint too big to be straightforwardly implemented into existing microscopes. Hence, focused piezoelectric ultrasound transducers are commonly mounted in the optical axis of the microscopy objective atop the sample and are then positioned by a set of xyz-

translational stages in order to coalign the respective optical and acoustic foci [118, 119]. This additional and necessary bulk of components denies the combination with other microscopy modalities, such as multiphoton microscopy, where a photo-multiplier tube is commonly mounted in lieu of the ultrasound sensor. Moreover, acoustic detectors installed in transmission-mode need the samples to be embedded inside an acoustic coupling medium such as a water tank. These restrictions are not portable for standard microscopes and thus for many applications, such as cellular imaging in the life sciences as well as histopathological imaging in clinical applications. Moreover, piezoelectric elements that are employed in close proximity to the sample might be affected by light scatter or light reflected from the sample, leading to a thermoelastic expansion in the highly absorbing piezoelectric material, the acoustic matching layers or in the adjacent transducer housing. The recording of these parasitic signals then causes noise, amplitude offsets and ultimately artefacts in the process of optoacoustic imaging.

A workaround for epi-illumination (also referred to as reflection-mode) optoacoustic microscopy has been demonstrated based on optically transparent but acoustically reflecting elements, e.g. steering and projecting the acoustic signals onto a piezoelectric ultrasound transducer that is installed at a distance and perpendicular to the optical beam path [56, 120] in an inverted-microscope geometry. Yet, this approach has not found a widespread application, as it suffers from reduced bandwidths and acoustic signal attenuation. Additionally, the shortage of space in the setup remains, as the challenging footprint of the piezoelectric transducer remains untouched. Another approach for reflection-mode geometries has been demonstrated by all-optical ultrasound detection, taking advantage of miniaturized detector geometries, high sensitivities as well as broad frequency responses. Here, especially the use of detectors based on optically transparent resonators comes to mind when hypothesizing about multimodal microscopy of thick biological specimen in reflection-mode. Ultimately, these geometries are only limited by photon dispersion in tissue in terms of imaging depth and exposure limitations for the excitation light penetrating the sampled region (see section 8.1). A prominent example for transparent resonator based ultrasound detection in optoacoustic microscopy are optical micro-rings [65] that were discussed in chapter 3. Transparent polymeric micro-rings have been shown with sensitivities of up to 6.8 Pa, allowing optoacoustic microscopy of single red blood cells [121]. On the other hand, micro-rings exhibit a very high bandwidth gradient and have been shown with FOVs limited to around 100 μm x 100 μm. While this FOV is sufficient for high resolution applications of spatially confined samples such as red blood cells, the study of bigger morphological structures, such as complex vascular

networks, requires much wider FOVs or excessive sample positioning. Another challenge that thwarts the widespread application of optical ultrasound detection in the biomedical imaging community is its operational applicability. Recent read-out methods, such as pulsed interferometry and coherence restored pulsed interferometry (see chapter 3 and chapter 4), have been demonstrated to achieve sensitivities on a par with advanced piezoelectric detectors. While these methods represent the most advanced read-out for optical resonators [17], these systems are highly cost intensive and require skilled operators at the same time.

A novel approach addressing these challenges is presented in this chapter: The suggested detector combines an acoustic reflector with a π-FBG based ultrasound detector, enabling multimodal epi-illumination microscopy in off-the-shelf optical microscopes. The combined sensor-head can be mounted onto standard microscopy objectives and may be adapted to suit objectives with varying numerical apertures and working distances. The robust detector design allows for cw-laser read-out, cutting the overall system cost by a factor of 10. Here, the subsequent loss in sensitivity was successfully mitigated by the employed acoustic reflector. This elliptically shaped cavity effectively amplifies and focuses the acoustic signal onto an embedded π-FBG sensor. The combined sensor-head was thin enough to employ microscopy objectives with a working distance of 5 mm and was virtually transparent to the focused illumination beam passing through it.

The sensor-head was implemented into an existing multi-modal microscopy system and demonstrated the feasibility of this add-on optoacoustic modality without affecting other existing imaging modalities for the first time. In the presented setup, the sensor-head allowed to straightforwardly combine optoacoustic microscopy e.g. with well established modalities such as fluorescence imaging, Second Harmonic Generation (**SHG**) and Third Harmonic Generation (**THG**). So far, such combinations have only been demonstrated utilizing piezoelectric transducers [9, 31, 46] in transmission-mode geometries. In this chapter, the detector is characterized in terms of sensitivity as well as bandwidth and its overall performance is demonstrated by in-vivo images of mouse-ear and mouse abdomen. The findings presented in this chapter have been published in [35] and [122].

5.2 Materials and Methods

5.2.1 Experimental Setup

The experimental setup and working principle of the epi-illumination optical and optoacoustic microscope is depicted in Figure 5.1. The setup can be divided into four key components:

1. Light delivery for optoacoustic signal excitation.
2. Light delivery and detection for fluorescence and SHG microscopy.
3. An inverted microscope for sample alignment and optical microscopy.
4. A sensor-head and read-out system for the detection and recording of optoacoustic signals.

The light delivery for optoacoustic signal generation was provided by a 532 nm pulsed DPSS laser (SPOT-10-100-532; Elforlight Ltd, Daventry, UK) with an adjustable repetition rate between single shot and 50 kHz, a maximum pulse energy of 10 μJ, a maximum pulse duration of 1.8 ns and a near-Gaussian beam quality with $M^2 < 1.1$. For non-linear fluorescence imaging such as SHG and THG, a 1043 nm femtosecond laser (YBIX; Time-Bandwidth, Zurich, Switzerland) with a repetition rate of 84.4 MHz, a pulse duration of 170 fs and an output power of 2.8 W was employed. The two optical beams were individually resized by telescopes and spatially filtered by pinholes installed at the focal spots of the respective telescope. In order to adjust the fluence for different samples, each beam could be attenuated by neutral density filters installed along the respective beam path. The two beams were combined by a dichroic mirror and directed onto a xy-set of galvanometric mirrors (6215H; Cambridge Technology, Bedford, USA) installed inside another telescope for beam magnification. The beam then entered the inverted microscope with its diameter adjusted to fully fill the back aperture of the microscope objective in order to achieve near-ideal and diffraction limited optical focusing. Focused by a 10x objective (PLN 10X; Olympus, Hamburg, Germany) with a NA of 0.25 and a working distance of 10.6 mm, the combined and focused optical beam then passed the attached sensor-head with the optical foci coinciding at a distance adjustable between 100 μm and 500 μm above the sensor-head and well inside a given sample. The design of the sensor head is illustrated in Figure 5.2 and discussed in more detail in subsection 5.2.2. For SHG imaging, the fluorescent signals were collected by the microscope objective and traversed back along the incoming beam path. Here, the fluorescence signals were filtered

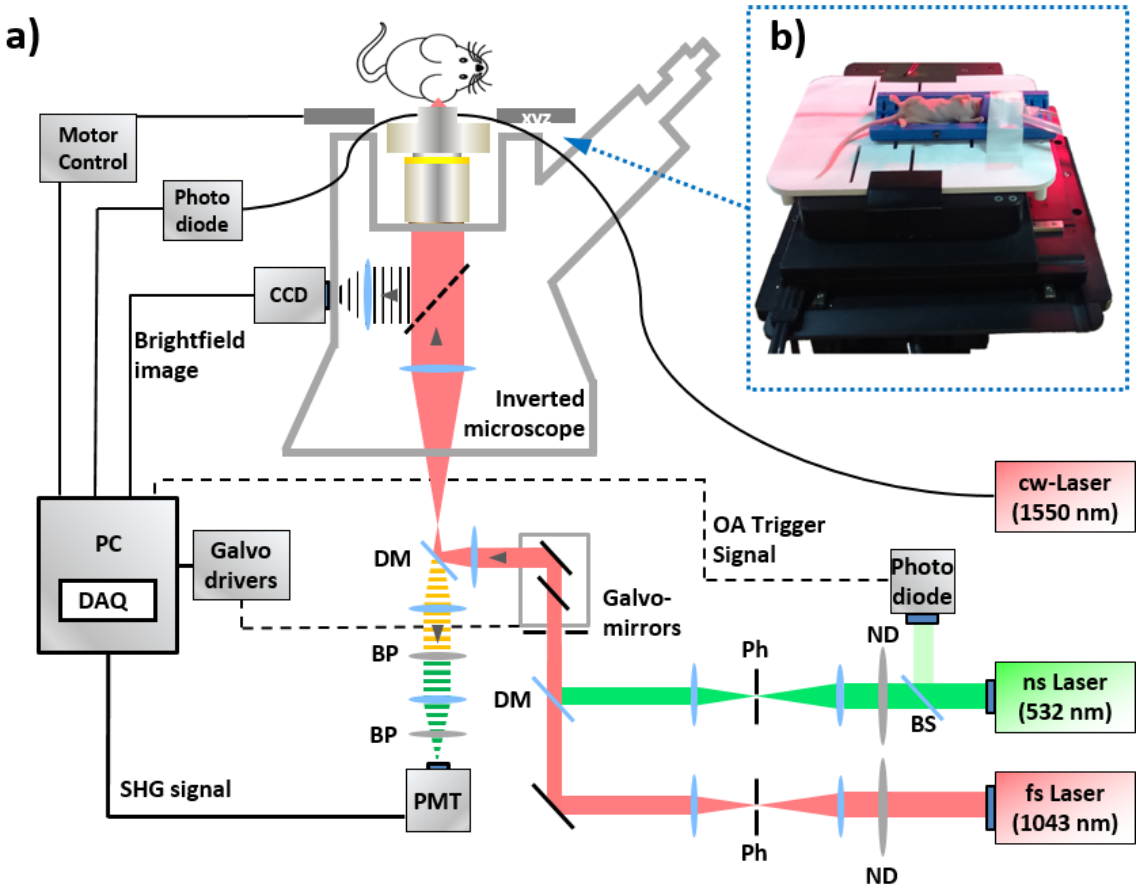

Figure 5.1: Schematic of the multi-modal epi-illumination microscope: (a) An inverted off-the-shelf microscope with implemented optoacoustic microscopy and SHG imaging modalities. The optoacoustic sensor-head is mounted atop the standard microscopy objective and read-out by a C-Band cw-laser. The 532 nm optoacoustic excitation beam is superimposed with the 1043 nm multiphoton excitation and scanned through a given sample by a set of galvanometric mirrors. (b) An anaesthetized mouse on a 3D-printed platform mounted atop a set of xyz stages. BP, bandpass filter; BS, beam splitter; DAQ, data acquisition card; DM, dichroic mirror; ND, neutral density filter; OA, optoacoustic; PH, pinhole; PMT, photomultiplier tube; xyz, motorized xyz-translational stages.

by a dichroic mirror installed prior to the galvanometric mirrors and then directed through a bandpass filter for spectral noise removal. Eventually, the filtered beam was slightly focused and lead into a photomultiplier tube (**PMT**) (PMT H9305-03; Hamamatsu Photonics, Hamamatsu, Japan).
Sample alignment was performed by a set of xyz-stages (xy-stage: MLS203-2 / z-stage: ZMZ500-E; Thorlabs, Newton, USA) with a minimum step size of 100 nm. The stages were mounted atop the inverted microscope and were equipped with an interchangeable set of 3D-printed sample holders, each customized for a particular specimen such as *in vivo* mice or *ex vivo* samples prepared on standard Petri dishes and microscopy slides. The sample holder for *in vivo* mice experiments is depicted in Figure 5.1b and allowed to adjust ambient temperature by an infra-red lamp as well as the installation of an anaesthetic supply unit. The aperture embedded inside the sample holder was covered with a thin layer of PE-foil that allowed to apply water or centrifuged ultrasound gel for acoustic coupling between the sample and the sensor head.

5.2.2 Hybrid Sensor-Head

At first glance, the implementation of transparent optical resonators as ultrasound detectors seems to be a straightforward approach of optoacoustic microscopy. Yet, most of the demonstrated detectors do not achieve the necessary performance, nor can they be integrated into given microscopes. This is caused either by a fragile sensor design, such as the case for optical micro-rings [97], or by an inherent hard-to-handle sensor geometry that would require major revision of the existing hardware, such as the case for slab shaped resonators [123]. An alternative resonator design is based on optical fiber based π-FBGs, which were shown with a relatively low NEP of around 100 Pa and a wide frequency response spanning over two bands. The latter corresponded to fractional bandwidths of 100 % and 21 % at frequencies of around 20 and 70 MHz, respectively (compare chapter 4). While these parameters were achieved in combination with superior but complex CRPI read-out, the interrogation by a cw-laser would decrease overall detector costs and simplify its usability in the life-sciences, hence possibly enabling a widespread application of the optoacoustic modality. Yet, the loss in sensitivity due to a simplified interrogation system needed to be compensated for. In response to these intertwined challenges, a combination of a π-FBG sensor and amplifying acoustic cavity was devised: The idea was based on the inherent advantage that π-FBGs can be manufactured with diameters ranging between 80 μm to 250 μm, depending on the respective cladding and coating thicknesses. Taking advantage of this ultra-small sensor

footprint, an ellipsoidally shaped acoustic cavity could be installed between a given microscope objective and the sample plane, amplifying acoustic signals and directing them onto the sensor. Yet, this principle is only feasible if both the cavity as well as the ultrasound sensor do not interfere with the optical beam path of the microscope.
The suggested sensor-head is depicted in Figure 5.2a and is based on an acoustic cavity, an embedded π-FBG as well as on a housing sleeve that clamps the amplifying acoustic reflector onto a given microscope objective:
The acoustic cavity is illustrated in Figure 5.2b and its fundamental geometry was based on an ellipsoid, manufactured with a major axis of 9.6 mm and a minor axis of 8.2 mm in length, respectively. Here, the two geometrical foci of the ellipsoid were key for the sensor-head design, as acoustic waves originating at one of the foci are collected by the cavity, reflected off the cavity wall and subsequently focused onto the second acosutic focus of the ellipsoid. In order to maximise the acoustic reflection at the interface between the coupling medium inside the cavity (e.g. water) with the acoustic impedance Z_C and the cavity wall (e.g. hardened steel) with the acoustic impedance Z_W, the reflection coefficient R was maximised via [4]:

$$R = \left(\frac{Z_W - Z_C}{Z_C + Z_W} \right)^2 \tag{5.1}$$

Consequently, the acoustic cavity was CNC carved out of hardened stainless steel with an acoustic impedance of around 47 Mrayl, which is 31 times higher than that of water. For comparison, the acoustic impedance of glass is around 13 Mrayl and plastics such as ABS and PVC commonly have impedances between 2 Mrayl and 3 Mrayl (see reference [124] for detailed derivation and testing of acoustic impedances). In the case of the acoustic cavity, the theoretical reflection coefficients at the interface between the cavity wall and the water are 0.91 and 1, corresponding to a minimum and maximum incident angle of acoustic waves of 0° degrees and 31.3° degrees, respecitvely [125].
The amplification A of the acoustic cavity can be estimated by the overall surface area of the ellipsoid and the ratio of the solid angles of the ellipsoidal cavity Ω_{Cav}, of the beam aperture Ω_{Ape} as well as of the π-FBG Ω_{FBG}, via [126]:

$$A = \sqrt{\frac{\Omega_{Cav} - \Omega_{Ape}}{\Omega_{FBG}}} \tag{5.2}$$

The theoretical amplitude amplification of an acoustic signal by the acoustic cavity then had a factor of 14. Note that this amplification does not consider frequency dependent attenuation, as the acoustic waves that traverse through the cavity - and which are

subsequently focused onto the detector - have a longer distance to traverse than the acoustic waves hitting the π-FBG directly (compare chapter 3). As an analogy, the acoustic cavity can be viewed as a low-pass frequency filter that is applied onto acoustic signals collected by the sensor-head. Consequently, the effective acoustic amplification by the cavity as well as the frequency response of the detector were, a priori, belittled in comparison to the theoretical expectation.

In the actual implementation, the upper part of the cavity (facing the sample, see Figure 5.1 and Figure 5.2) housed the aperture that ended in a flat rim. Following the design described above, the cavity was tilted along the major axis by 12 degrees relative to the vertical axis of the objective, in order to separate the optical beam path from the position of the π-FBG ultrasound detector. The latter was positioned at the inner acoustic focus of the cavity. Two 250 μm bores on either side of the cavity, on an axis perpendicular to the optical axis, allowed the optical fiber to be guided through the cavity. During the insertion process, the transmission-mode π-FBG had to be adjourned and subsequentally fusion-splied. The 300 μm effective sensing length [62] of the π-FBG was then positioned centrally at the acoustic focus inside the cavity and the bores sealed with silicone. The π-FBG is depicted in Figure 5.2c, where a faint white horizontal line above the aperture at the bottom of the cavity reveals the optical fiber with the embedded π-FBG. The second geometrical focus of the ellipsoid was placed outside the cavity, around 400 μm above the rim of the sensor-head and coincided with the optical foci of both the multi-photon as well as of the optoacoustic excitation beam. Normally, the sensitivity field in terms of detection angle of a cylindrical ultrasound detector, such as a fiber based FP, can be estimated as radially symmetric along the cylindrical axis. In the case of the presented π-FBGs though, the gratings were inscribed into polarization maintaining fibers, where the polarization inside the fiber introduced an angular dependent sensitivity towards acoustic waves [114]. As a consequence, and although the complete surface of the cavity did contribute to acoustic signal detection, the π-FBG was rotated around its axis in approximately 5° steps in order to optimize SNR. In this context, small areas at the cavity wall that where acoustically shadowed by the optical fiber as well as reflection limitations at very shallow angles relative to the fiber axis also affected the effective radial sensitivity of the π-FBG but were neglected, i.e. when calculating the theoretical amplitude amplification.

The distance between sensor-head and absorber was selected as the favourite depth to study sub-dermal vasculature in mouse models and could be adapted to different heights for other samples. Governing factors for penetration depth were the working distance

of the applied microscope objective as well as the resulting maximum height of the sensor-head and embedded acoustic cavity with a final height of around 6 mm.

In order to grant acoustic coupling between the sample, the cavity and the π-FBG, the cavity was filled with pure distilled water and covered by thin polyethylene foil of 10 μm thickness. A thin layer of vacuumized and centrifuged ultrasound gel was then applied atop the foil to provide acoustic coupling between the sample and the cavity. A close-up of the sensor-head with the cavity filled with distilled water and covered by foil is shown in the appendix (section 8.3). The bottom of the cavity was sealed by a circularly trimmed microscopy cover slip with a thickness of 170 μm (corresponding to the # 1.5 standard), which was additionally sealed atop the bottom of the acoustic cavity by a highly fluid UV cureable epoxy resin. As discussed above, an aperture was integrated at the bottom of the acoustic cavity to allow for the optical beam path to traverse through the sensor-head (see Figure 5.2).

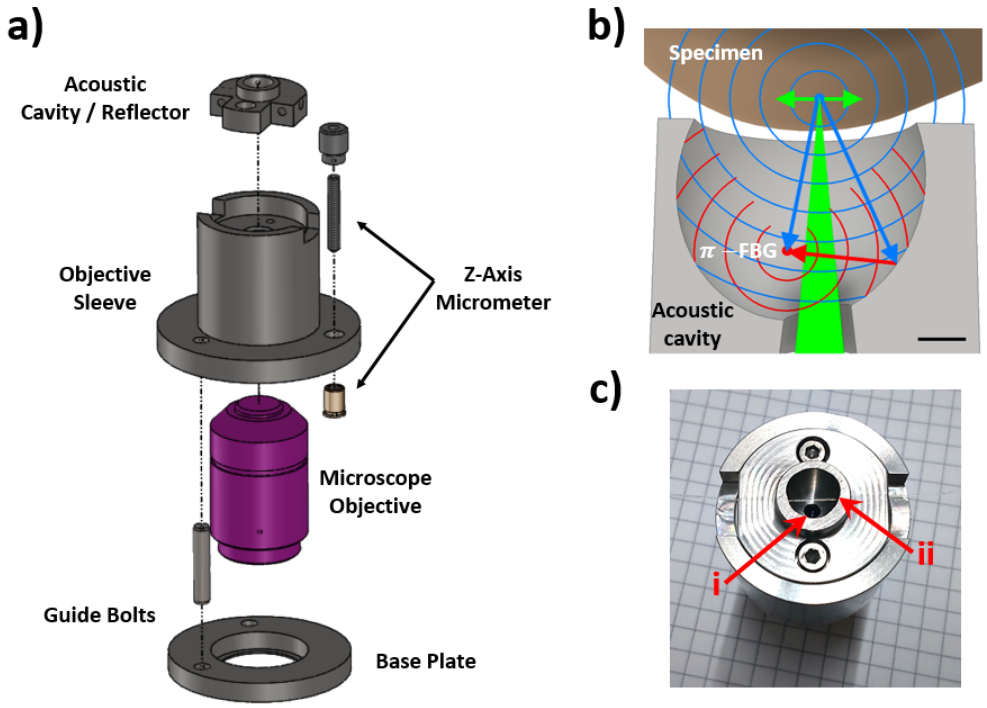

Figure 5.2: Schematic and working principle of the π-FBG sensor-head: (a) Exploded assembly drawing of the sensor-head components and the microscope objective. (b) Cross-sectional view of the ellipsoidal acoustic cavity. Optoacoustic signals excited at the optical focus (blue circles) are reflected off the cavity wall (red circles) and focused onto the π-FBG. Scale bar, 1.5 mm. (c) Topview photograph of the sensor-head: i) Aperture for optoacoustic and multi-photon excitation beams. ii) Optical fiber with embedded π-FBG sensor.

The housing sleeve is depicted in Figure 5.2a and comprised a sleeve for the microscope objective that allowed to adjust and fix the acoustic cavity above the objective along the z-axis as well as a baseplate attached to the base of the microscope objective, which lead to a bolted flange connection. Note that the baseplate was designed with a thickness of only 0.5 mm as well as with an L-shaped shoring rim. Hence, it did not interfere with the screw joint of the existing microscope and allowed to implement the sensor-head in any microscope with a revolving objective mount. In detail, two guide bolts (for simplicity, only one bolt is depicted in Figure 5.2a) were fused onto the base plate and allowed vertical movement within highly precise guiding grooves embedded inside the rim of the objective sleeve. The two guiding bolts and the implemented micrometer as virtual third bolt were arranged in 120° intervals and allowed for μm-precision alignment of the acoustic cavity along the z-axis and relative to the objective. This way, the acoustic focus of the cavity as well as the optical foci of the excitation and multiphoton beams could be individually aligned along a common axis.
Note that the sensor-head was not connected to the 3D-printed sample holder, but was rather placed in the center of a 2 cm x 2 cm wide aperture embedded at the base of the sample holder. Similar to the cover of the acoustic cavity, the aperture in the sample holder was sealed by thin ($\leq 15\ \mu m$) PE-foil and wetted by a drop of water or centrifuged ultrasound gel for acoustic coupling. An exemplary close-up of the installed sensor-head in a standard revolving objective mount in parallel to another microscope objective is shown in the appendix in section 8.3.

5.2.3 Image Acquisition

For the detection of optoacoustic signals, a custom-made π-FBG (Teraxion, Quebec, Canada) was installed inside the sensor head and read out by a tunable cw-laser (INTUN TL1550-B; Thorlabs) with 20 mW power in the C-Band. The π-FBG was interrogated in transmission mode similar to the way depicted in Figure 4.5. Analogous to the approach described in subsection 3.4.4, the cw-laser was tuned to match the spectral position of the FWHM of the π-FBG resonance and ultrasound-induced variations in the intensity of the transmitted light were recorded by a high speed photodiode (PDB450C; Thorlabs). The optoacoustic as well as the fluorescence signals were recorded by a 12 bit DAQ card (ADQ412, 2 GHz bandwidth; SP Devices, Linkoeping, Sweden) and the time trigger for optoacoustic signal recording was provided by a photodiode (DETA36A; Thorlabs) sensing stray-light at the laser output.
OAM imaging was then performed in a similar manner to chapter 4 with the addition that

the Matlab script allowed to adjust step size, FOV and averaging of optoacoustic signals per scanned point via directing the galvanometric mirrors. Moreover, the adjustable repetition rate of the illuminating DPSS laser was adapted to the scanning speed of the galvanometric mirrors in order to allow for fast scanning on the one hand and the compliance with maximum allowed fluence per scanned point on the other hand (see appendix, subsection 8.1.2).

The FOV for the optoacoustic as well as the SHG modality was governed by the maximum deflection of the galvanometric mirrors in interplay with the filling of the back aperture of the microscope objective. In practice, the galvanometric mirrors covered a maximum area of around 630 μm x 630 μm. When wider FOVs were imaged, such as the case when investigating wide vascular networks in mouse ear samples, the xy-translational stage of the sample holder was moved iteratively through an xy-pattern. The images recorded at each position were then stitched together in a post-recording process by the help of the image processing software ImageJ (v1.50; Wayne Rasband) and its Fiji distribution [127].

5.3 System Characterization

In order to compare the performance of the suggested detector to prevalent sensors from the literature and to those presented in chapter 3, the sensitivity, bandwidth, sensitivity field as well as the spatial resolution of the hybrid sensor-head were determined and are presented in this section. Note that the multi-modal capability as well as the applicability of the suggested sensor-head were key aspects of the system and all characterization experiments were therefore performed in the identical experimental setup with the same optical layout. In addition, the optoacoustic as well as the SHG and brightlight imaging modalities were coaligned before conducting the respective experiments.

5.3.1 Sensitivity and Bandwidth

Figure 5.2b demonstrates the working principle of the cavity and how ultrasound originating at the virtual outer acoustic focus of the ellipsoid was collected and projected onto the focus inside the acoustic cavity, where the actual detection of ultrasound was performed by the π-FBG. This is particularly important to point out, as acoustic signals collected by the sensor-head reach the π-FBG twice: Any acoustic wave originating at the outer geometrical focus of the ellipsoid will enter the cavity and directly hit the π-FBG (blue arrow), leading to a first acoustic signal recording. A second acoustic signal will be recorded after the acoustic waves were reflected off the cavity wall, simultaneously focused by the ellipsoidal shape of the cavity and then hit the detector (red arrow) with a time delay corresponding to the additional distance traversed. This effect of two separately recorded acoustic signals is demonstrated in Figure 5.3a, where two corresponding signals from a suture phantom (similar to the one described in subsection 4.5.1) are shown. Here, the first peak (i) depicts the acoustic signal that was directly recorded by the π-FBG and the second peak (ii) depicts the acoustic signal that was amplified by the acoustic cavity. The difference in arrival time of the two signals corresponds to the 3 μs duration between the two peaks in Figure 5.3a, which is in good agreement to the theoretical value of an acoustic wave with a central frequency of 20 MHz traversing a distance of 4.5 mm at a rounded speed of 1500 $\frac{m}{s}$ in water. The ratio of these two signals yielded the effective acoustic amplification of a factor of around 5. The actual sensitivity of the sensor-head then follows when comparing the amplification to the performance of a plain π-FBG. Here, a previous sensitivity measurement [62] of identical π-FBGs with a cw-laser read-out was demonstrated to have a sensitivity of around 440 Pa in terms of NEP. Taking the amplification by the acoustic cavity into account, the sensitivity of the

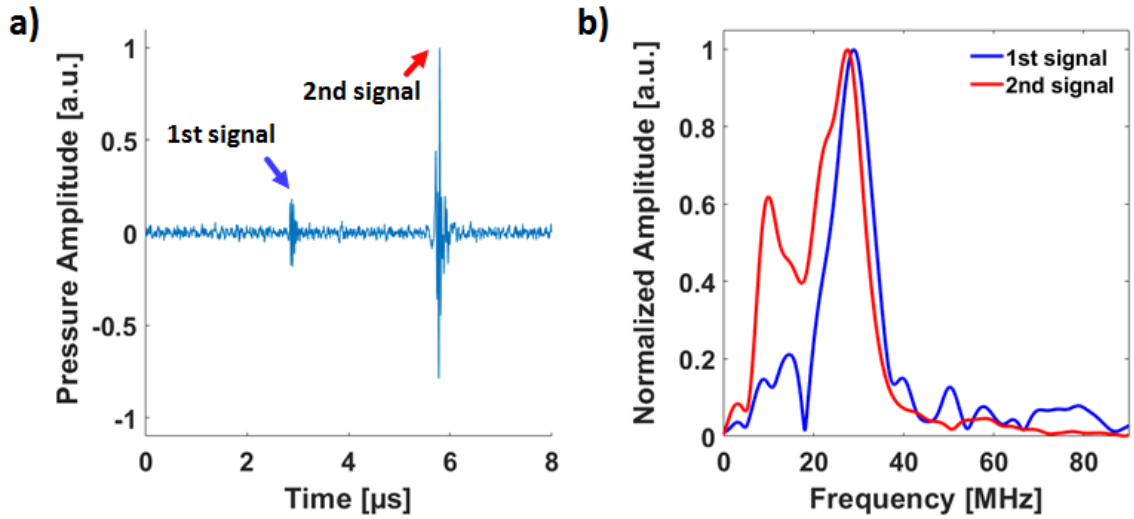

Figure 5.3: Characterization of the π-FBG sensor-head: (a) Optoacoustic signal recorded from a polystyrene suture in the time domain with the indicated 1st and 2nd peaks corresponding to the signal recorded directly at the π-FBG and the signal amplified by the acoustic cavity, respectively. (b) Frequency response of the sensor-head for the acoustic signals displayed in (a), indicating a spectrum slightly shifted towards lower frequencies with respect to the reflected and amplified signal.

combined sensor-head could be estimated to a NEP of around 88 Pa.

For a meaningful bandwidth analysis of the sensor-head, it is also interesting to look at both recordings of the sensor-head. Here, the frequency response was individually examined by a Fourier-analysis of the recorded time-domain signals for both acoustic peaks. The first and the second acoustic signal were windowed and FFTs applied separately. The resulting bandwidths for the direct and the indirect acoustic signal are shown in Figure 5.3b, with the bandwidths of the direct and the indirect signal depicted in blue and red colour, respectively. While the peak response is located at around 28 MHz for both signals, it is apparent that the indirect signals underwent an attenuation for frequencies of around 40 MHz and beyond. This is in agreement with the frequency dependent attenuation of acoustic waves as predicted in subsection 5.2.2. The total bandwidth of the sensor-head then corresponds to the frequency response towards the sought-after amplified second signal and was found to be around 30 MHz.

5.3.2 Sensitivity Field

For the hybrid implementation of optoacoustic microscopy with imaging modalities such as multiphoton microscopy or confocal microscopy, it is vital to have an acoustic sensor

that covers a reasonably sized FOV. The implementation of galvanometric mirrors in an epi-illumination geometry also requires a sensor with a sensitivity field wide enough to detect acoustic signals originating at each point of the scanned area. In the case of the demonstrated setup, the FOV was therefore foremost governed by the area scanned by the galvanometric mirrors, which had a size of around 630 μm x 630 μm. On the other hand, the size of the maximum achievable FOV was also confined by the outer acoustic focus of the sensor-head. Here, the effective size of the acoustic focus depended on the frequency content of the detected signals, the quality of the ellipsoidal shape as well as on the surface roughness of the acoustic reflector. Due to this multitude of parameters affecting the latter, the combined sensitivity field - as governed by the galvanometric mirrors and the acoustic focus - was determined experimentally. In the related experiment, a suture-phantom was imaged that consisted out of a vertical and a horizontal black polystyrene suture of around 19 μm diameter (Dafilon Polyamide; B. Braun Melsungen AG, Melsungen, Germany). A bright-field microscopy image of the suture cross is shown in Figure 5.4a. The corresponding MIPs of the first and the second recorded acoustic signals are depicted in Figure 5.4b and Figure 5.4c. Here, the suture cross images were reconstructed based on the direct (1st signal without amplification) and the indirect (2nd signal with amplification) acoustic signals as recorded by the π-FBG, respectively.

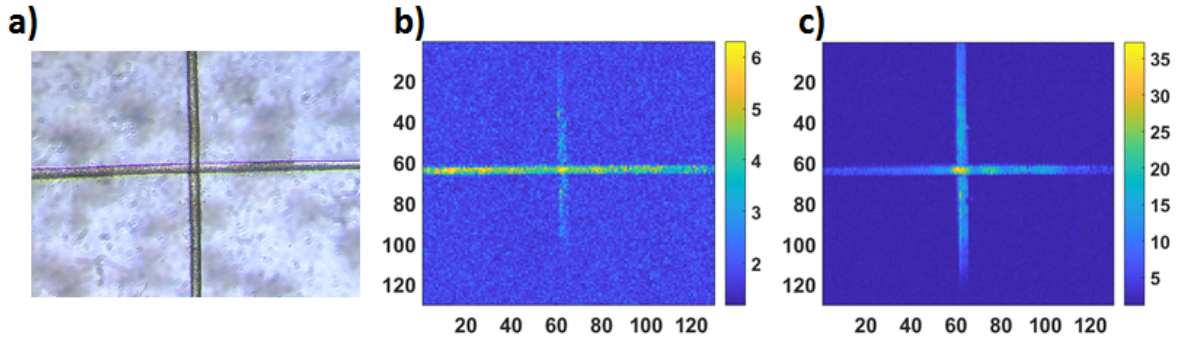

Figure 5.4: Sensitivity field of the sensor-head: (a) Bright-field microscopy image of 10 μm diameter black polystyrene sutures arranged in a vertical cross. (b) MIP of the optoacoustic signals recorded directly by the π-FBG and (c) recorded by the π-FBG after amplification, corresponding to the 1st and 2nd signal depicted in Figure 5.3, respectively. MIPs recorded with 130 x 130 pixels at $\sim$ 4.84 μm step size.

The SNR analysis revealed an acoustic signal amplification of a factor of around 5 in analogy to subsection 5.3.1 and as observable as improved image contrast when comparing Figure 5.4b and Figure 5.4c. Moreover, the sutures are visualized over the complete

FOV of 630 μm x 630 μm as governed by the optical beam deflection. In analogy to other ultrasound detectors, the detection angle of the combined sensor-head was then deduced relative to the optical axis and found to be around 76.5°. The resolution of both MIPs was set to 130 x 130 pixels with a step-size (pixel-size) of around 4.84 μm. Image reconstruction was performed over 30 averages, yielding an overall SNR of 39.8 (corresponding to $\approx$ 32 dB) for averaged images and a SNR of 7.3 (corresponding to $\approx$ 17 dB) without averaging, respectively (assuming that for constant random noise, averaging increases SNR by the square root of the number of averages).

5.3.3 Spatial Resolution

In optoacoustic microscopy, the spatial resolution is generally governed by the specifications of the focusing optics as deduced in chapter 2. Hence, the theoretical axial resolution of the sensor-head was deduced from its bandwidth. Based on the upper frequency limit of 40 MHz and when applying the method demonstrated in [110], the axial resolution could be approximated to around 37 μm. The lateral resolution can generally be determined by the NA of the applied microscope objective (see chapter 4), but needs to be addressed differently for the suggested sensor-head, as the optoacoustic excitation as well as the multi-photon beam traversed through the sensor-head and consequently underwent optical refraction in the coupling medium as well as in the terminating PE-foils. In order to examine the effect of these impairments onto the optical beam path, the lateral resolution was determined experimentally.
In transmission-mode setups, the only experimentally feasible method to measure the lateral resolution of a system is to image objects of a well-defined size. In the case of the suggested epi-illumination geometry though, a different approach can be applied, where line scans or a small image of a sharp-edged object are utilized. In the case of the suggested sensor-head, the facet of a 0.8 mm x 3 mm sized silicon block (silicon-on-isolator) was imaged (IMEC, Leven, Belgium), where the facet as well as the front-side of the block were polished to optical grade with a surface roughness of approximately $R_a \leq 20$ nm. A bright-field microscopy image of the corner of the silicon block is shown in Figure 5.5a, with a black square marking the imaged area. For imaging, the block was mounted onto a 3D-printed sample holder with its facet facing the sensor-head. This sample holder allowed sample translation along the z-axis independent from the position of the sensor-head which in turn allowed to iteratively perform single point scans along the z-axis and thus to position the facet exactly in the focal plane of the optoacoustic excitation beam. The MIP of the framed area is depicted in Figure 5.5b and was obtained

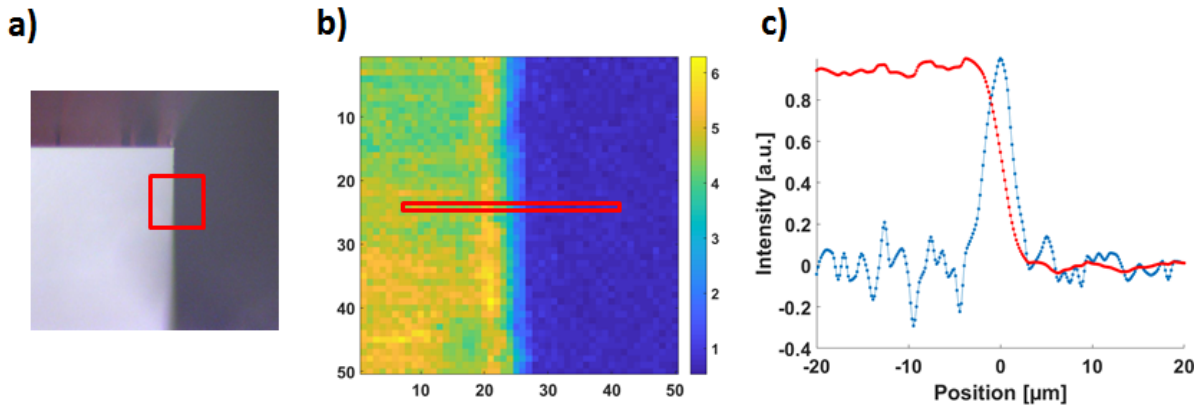

Figure 5.5: Resolution characterization of the sensor-head: (a) Bright-field microscopy image of the silicon-on-isolator block, with the polished facet in the bottom left and the scanned area marked by a red frame. (b) MIP of the facet recorded across the edge and with an overall size of 32 μm x 32 μm. (c) Edge spread function and corresponding line spread function of the signals indicated in (b), revealing a lateral resolution of 3.7 μm.

with an overall size of 50 x 50 pixels and a step size of 0.63 μm.

In the MIP in Figure 5.5b, the red frame marks the signals for the edge-spread function plotted as red line in Figure 5.5c, where the corresponding line-spread function is plotted in blue. The optical resolution of the system then corresponds to the FWHM of the line-spread function and was found to be around 3.7 μm. While the theoretical lateral resolution as given by the microscopy objective can be estimated to around 2.6 μm, these values are still in reasonable agreement, given non-perfect edges of the silicon block as well as optical diffraction and diffusion along the beam path. It is also important to note that this resolution only applies to the optoacoustic modality, as optical obstructions in the cavity affected purely optical imaging modalities such as SHG microscopy a second time, as the photons emitted in the sample traverse the acoustic cavity and are collected by the microscope objective. Due to a lack of standardized samples suitable for multiphoton microscopy, the resolution of the SHG imaging modality was not determined in this work.

5.4 Experiments and Results

5.4.1 Optoacoustic Microscopy of Mouse Ear Models

Mouse models are among the most commonly applied biological specimen for optoacoustic microscopy, in particular due to the existing vascular density in the flat and highly

accessible mouse ear. Close-up photographs of the mouse pinna are depicted in Figure 5.7 and show the additional advantage of nude mouse models that no further dominant optical absorbers are prevalent, such as cutaneous pigment melanin in dermal tissue as well as melanin in hair and hair follicles (compare optical absorption coefficients in Figure 2.4).

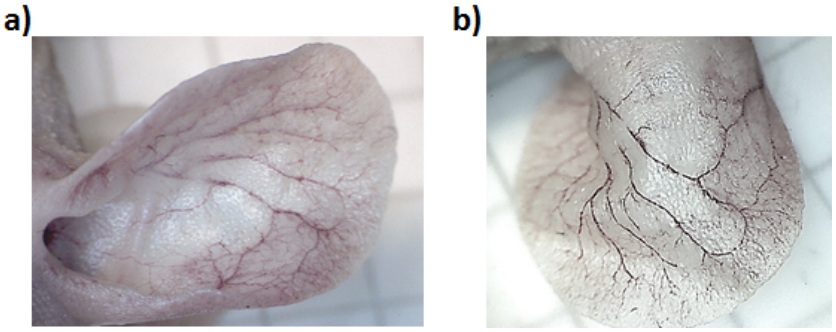

Figure 5.6: Close-up photographs of mouse ear models: (a) Inner and (b) outer mouse ear pinna *ex vivo* of female Nude-1 Foxn1 mice without perturbing optical absorbers such as cutaneous pigment melanin or pigmentation in hair and hair follicles.

These advantages are key factors when imaging with optoacoustic transmission-mode setups and mouse ear models have therefore been demonstrated repeatedly in the literature [46,57,60,79,120,128]. As the suggested sensor-head allows setup geometries in reflection-mode, it was not strictly necessary to perform experiments on identical samples. Nevertheless and in order to allow for image quality comparison with approaches from the literature, such as piezoelectric and other optical detectors, initial *in vivo* images were also acquired from a mouse ear model.

Experiments were performed with female Nude-1 Foxn1 mice that were aged between 10 and 12 weeks (Harlan Laboratories Bioservice GmbH, Walsrode, Germany). During imaging, the mice were positioned onto a 3D printed holder without fixation as seen in the inlet of Figure 5.1. Here, the skin ROI was centered on the aperture and the skin-foil interface was wetted by a drop of centrifuged ultrasound gel. The mouse torso and head were positioned sideways upon the holder, which allowed to easily locate the ear on the aperture and to fixate the ear by the viscosity of the applied ultrasound gel. Mice anaesthesia was performed by a custom-built breather covering the mouse nose and applying 1.8 % isoflurane via a commercial evaporator. The mouse body temperature was monitored throughout the experiments and an infrared lamp was mounted next to the microscope setup to maintain the natural body temperature.

A 6 x 6 tile set of optoaocustic MIPs for separate FOVs was stitched together and is

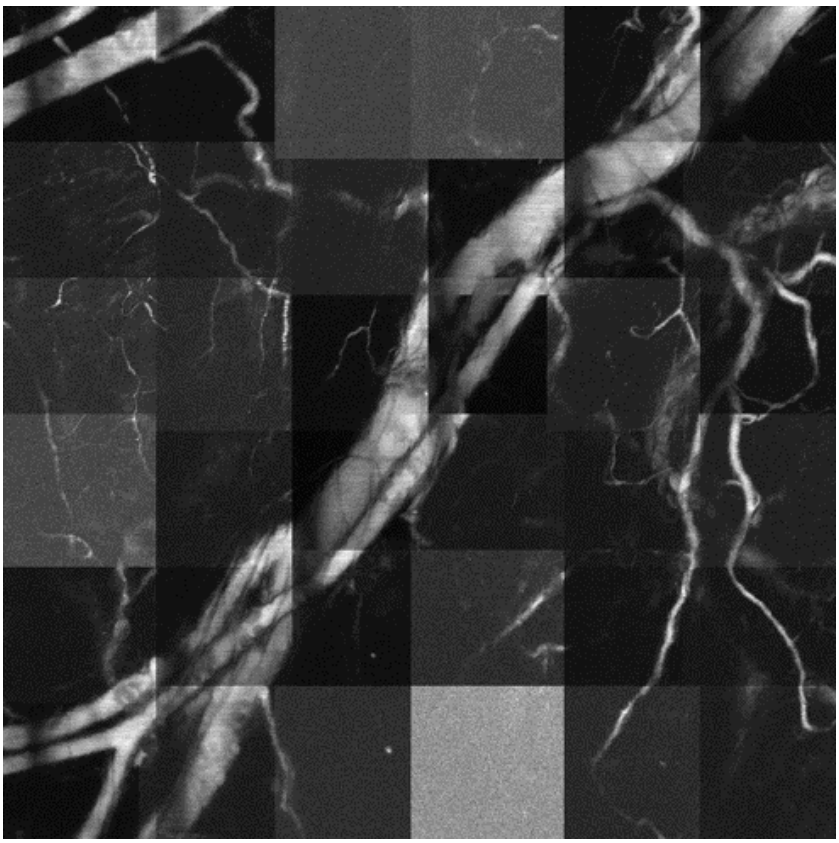

Figure 5.7: Optoacoustic microscopy image of an *in vivo* mouse ear: 36 individual MIPs were recorded with galvanometric mirror scans and stitched together with an overlap of up to 60 μm. Different respective SNR levels indicate tissue sections with varying maximum optical absorption contrast. Average tile size: 170 x 170 pixels with 2.4 μm step size. Overall stitched image size, 2 mm x 2 mm.

depicted in Figure 5.7 with an overall size of 2 mm x 2 mm. In order to avoid distortions at the image edges and to improve the super-positioning quality of the stitching algorithm, a relatively large overlap of 60 μm was appointed into each direction of each axis per FOV. The individual image acquisition was performed by scans with the galvanometric mirrors covering 170 x 170 pixels with a respective step size of 2.4 μm, yielding an effective size of 408 μm. At a repetition rate of 25 kHz and when averaging 100 samples for SNR improvement, a single FOV scan lasted 116 s, yielding a theoretical overall image acquisition time of around 70 minutes. It is relevant to note that the duration of these scans may be a limiting factor for the overall dimension of the acquired images. In order to prevent extensive alterations in the blood circulation and to not overextend the mouse anaesthesia, measurements could be performed in separate sessions.

Figure 5.8 revealed an entangled artery and vein pair of approximately 50 μm and 150

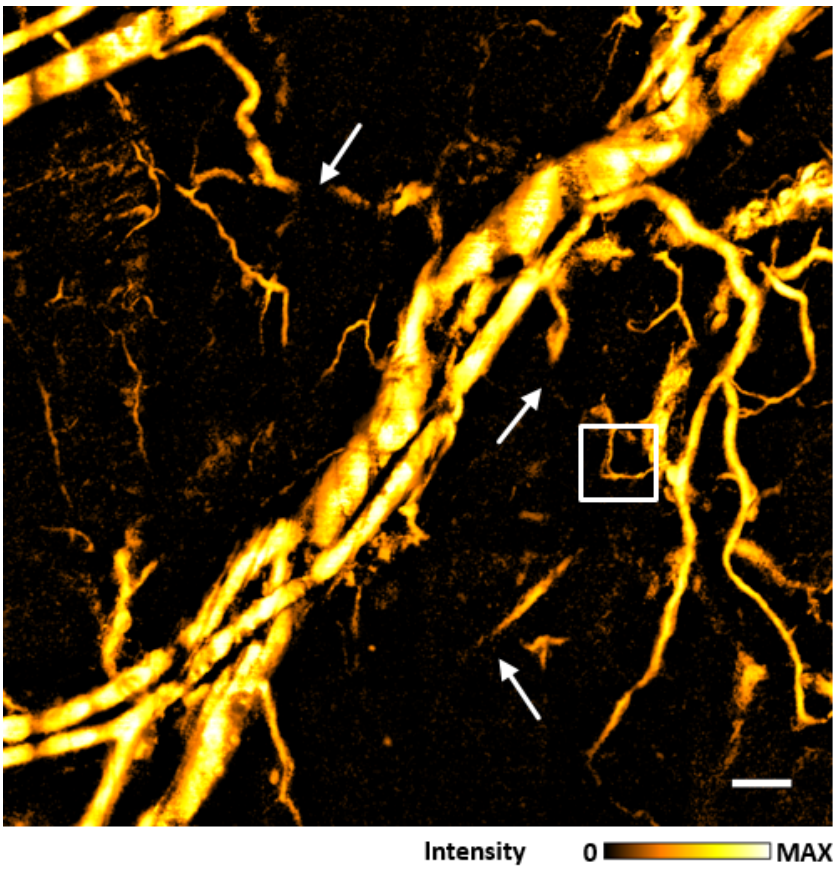

Figure 5.8: Processed optoacoustic microscopy image of an *in vivo* mouse ear: The stitched optoacoustic microscopy MIP depicted in Figure 5.7 after co-registration and image processing. The image reveals a continuous entangled artery and vein pair with a complex vascular network and vessel diameters ranging between around 6 μm and 150 μm. White arrows: locations with vasculature leading into and out of the image plane. White box: ROI of microvasculature as highlighted in Figure 5.9. Scale bar, 150 μm.

μm diameter, respectively, along with complex and ramifying vascular networks. The upper right corner of the MIP is facing towards the mouse head and the bottom left corner is facing towards the rim of the mouse ear. Exemplary areas with vasculature continuing vertically to the image plane or where vessels apparently discontinued are marked by white arrows. Interestingly, mouse ears commonly have overall thicknesses of around 0.2 - 0.3 mm with most of the vasculature and microvasculature branching out along one plane along its center. As the epidermis is rather thin in the mouse ear, measuring no more than 10 - 15 μm in adult mice [129], it makes the vasculature even more accessible for imaging. Hence, the observation of vasculature dropping in and out

of the thin imaging plane underlined the relatively high axial resolution of the setup of few tens of μm. Furthermore, the *in vivo* images demonstrated the capability of the suggested sensor to image smallest vasculature at depths of more than 100 μm in tissue.

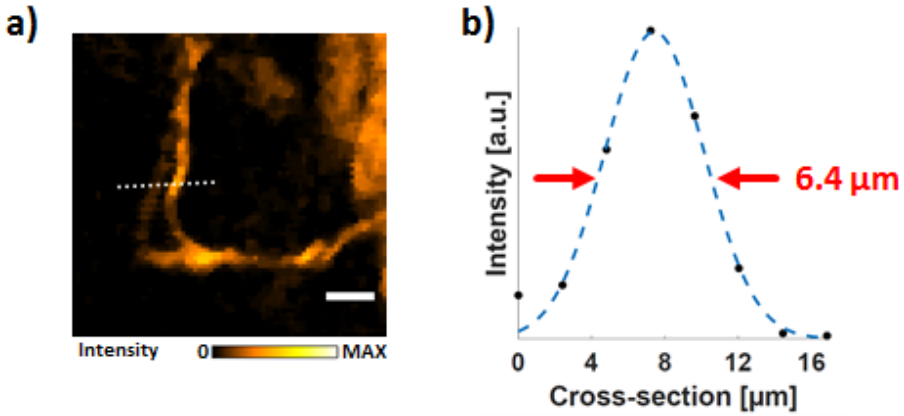

Figure 5.9: Vascular analysis of an *in vivo* mouse ear: (a) Close-up of the ROI indicated by the white box in Figure 5.8. Scale bar, 30 μm. (b) A Gaussian fit to the cross-section over the micro-vasculature indicated by a dotted line in (a) reveals a vessel diameter of around 6.4 μm.

In order to analyze the diameter of the smallest vessels that were successfully imaged with the sensor-head, multiple ROIs with comparably small individual vasculature were examined. Exemplarily, the ROI of 180 μm x 180 μm as marked by the white square in Figure 5.7 was separately examined and the according MIP is depicted in Figure 5.9a, with the target vessel marked by a white dotted line. The optoacoustic signals recorded in a scan perpendicular to the vessel orientation are plotted in Figure 5.9b along with a Gaussian fit of $R^2 = 0.986$ and the respective FWHM revealing a vessel diameter of 6.4 μm. Vascular diameters of these ultra-small dimensions suggest that the recorded optical absorption contrast of the vessels is provided by single red blood cells traversing inside them. Hence, discontinuities of such microvasculature are likely to represent a period in time, where no red blood cell passed through the corresponding vessel during the snapshot of image acquisition.

5.4.2 Multi-Modal Microscopy of Mouse Abdomen Models

A key advantage of the suggested multi-modal sensor-head was to allow for reflection-mode optoacoustic microscopy, i.e. by demonstrating *in vivo* imaging of thick tissue samples such as the well established mouse model. The lower rear abdomen of living mice was imaged for this purpose and a typical ROI is shown in Figure 5.10 at a wild-type

mouse model. Here, vasculature of more than 100 μm in diameter seems to be easily accessible at first glance, but the visible vessels are embedded in the adipose tissue well below the dermis. Hence, the actual experiments on mouse abdomen were performed on female Nude-1 Foxn1 mice that were aged between 10 and 12 weeks (Harlan Laboratories Bioserve GmbH). Mouse handling, preparation of the sample holder as well as the actual optoacoustic microscopy imaging and image processing were performed in analogy to subsection 5.4.1.

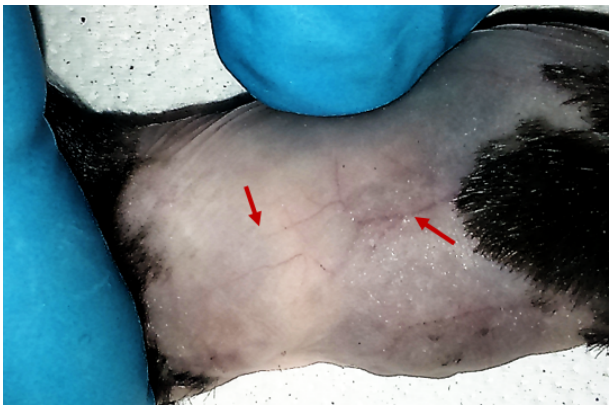

Figure 5.10: Abdominal vasculature in a wild-type mouse model: Sub-dermal blood vessels with estimated diameters of ≥ 100 μm, indicated by red arrows.

Figure 5.11 shows the optoacoustic image of mouse dermis at the lower rear abdomen, spanning an area of 1.8 mm x 2.2 mm. The overall image was stitched together by 35 individual MIPs (arranged in the order of 5 x 7 tiles) and an overlap of 42 μm was applied. In contrast to experiments in the mouse ear, optoacoustic excitation induced signals originating deeper inside the mouse skin. Hence, the recorded signals were divided into two time-intervals and overlayed in the image, with signals originating in the dermal region of around 300 μm depth color-coded in red-hot color map and signals originating 200 μm deeper color-coded in green, respectively.

A complex network of vasculature is discernible, with micro-vasculature branching in and out of a number of deeper arteries and veins that run vertical to the image plane. Consequently, and in comparison to the mouse ear depicted in Figure 5.7, more vessels are fading in and out of the focal plane. As for the absorbers deeper inside tissue, coarse structures are observable that partially coincide with the superficial vascular network. Yet, these structures are a minimum of 200 μm away from the focal plane and therefore appear blurry and diffuse. It is interesting to note that in contrast to the mouse ear, no major vessels with diameters of 100 μm or more are visible, as in the mouse torso, it is commonly vasculature sized 50 μm or less that branches within the lower adipose tissue

and then runs into the upper dermal layers.

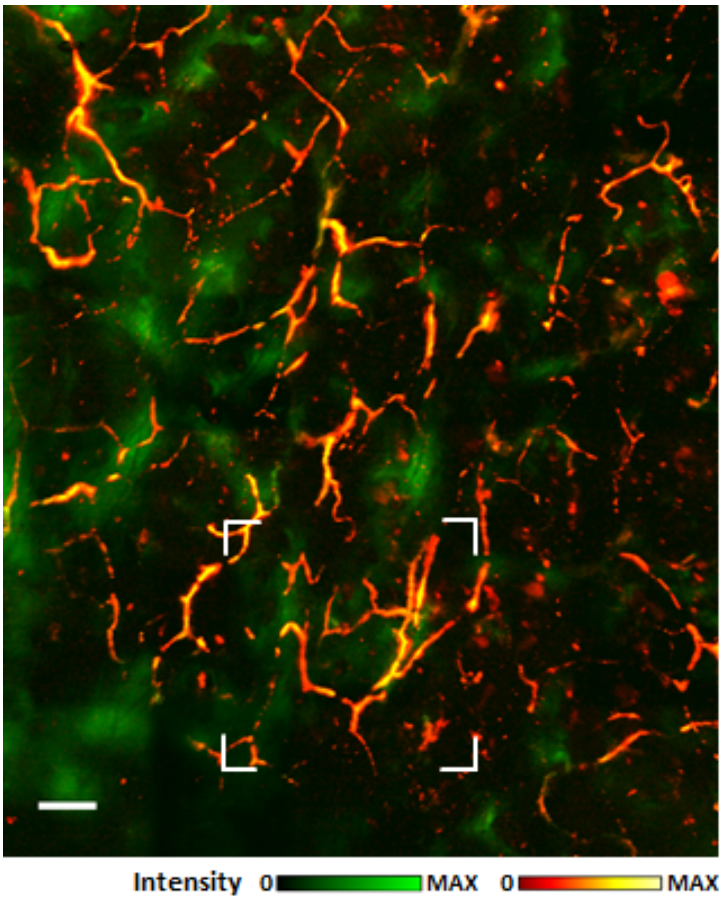

Figure 5.11: Processed optoacoustic microscopy image of the rear lower mouse abdomen *in vivo*: Stitched optoacoustic microscopy image revealing a complex 3D-network of micro-vasculature with an overall FOV of 1.8 mm x 2.2 mm, gathered by 35 individual tiles. Red-hot color-map corresponds to signals originating at around 300 μm depth, green color-map corresponds to signals at around 500 μm depth. White box: ROI selected for SHG microscopy as highlighted in Figure 5.12. Scale bar, 150 μm.

In order to demonstrate the multi-modal capability of the sensor-head, SHG imaging was performed on the ROI as indicated in Figure 5.11. An optoacoustic image of the ROI with a superficial vascular network (at 300 μm depth) is depicted in Figure 5.12a, corresponding to an area of 630 μm x 630 μm. The corresponding SHG image of the same ROI is depicted in Figure 5.12b, where well-defined collagen structures are discernible, including individual bulges and pairs of bulges at the interface between the dermis and the epidermis. These openings in the otherwise closed collagen layer indicate the position of hair follicles as well as of sebaceous glands adjacent to the hair follicles. Note that

the bulges are also visible with optical absorption contrast in optoacoustic imaging in wild-type mice as seen in section 8.3. The overlay of the optoacoustic and the SHG image is shown in Figure 5.12c, where the optoacoustic signals were color-coded in blue for better contrast. The hybrid image reveals successful co-localization of the complementary contrast methods.

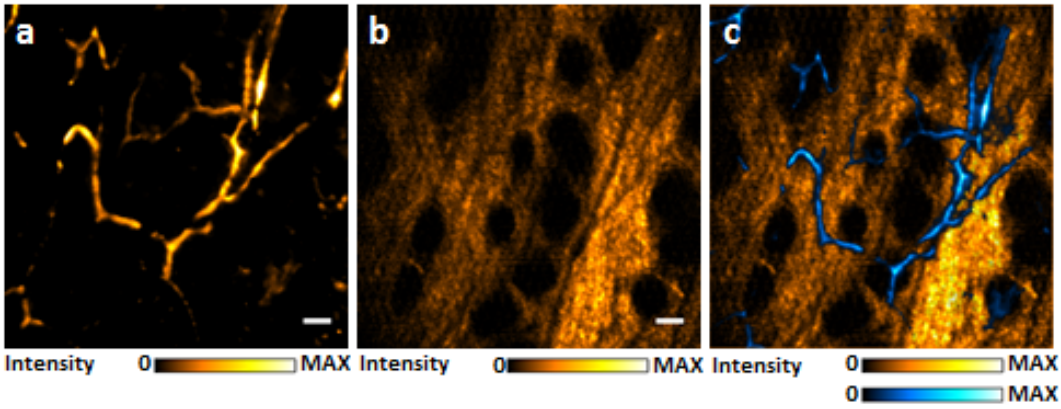

Figure 5.12: Combined optoacoustic and second-harmonic generation microscopy: (a) Higher-magnification optoacoustic image of superficial dermal vasculature as indicated in the ROI in Figure 5.12c. Scale bar, 50 μm. (b) SHG image of the ROI indicated in (a), revealing collagen structures and embedded bulges indicating hair follicles and adjacent sebaceous glands. Scale bar, 50 μm. (c) Overlay of images (a) and (b), with optoacoustic signals color-coded in blue, indicating complementary contrast of the imaging modalities.

A key advantage of optoacoustic microscopy compared to other imaging modalities is its superior imaging depth. While the sensor-head was designed with a pre-determined depth of the focal plane between around 300 μm and 400 μm, depending on the thickness of the coupling media, fine adjustment of imaging depth could be performed by levelling the translational stage of the sample-holder relative to the sensor head. Figure 5.13 shows two optoacoustic images, again taken of the ROI as indicated in Figure 5.12a. Here, Figure 5.13a was imaged at a depth of around 100 μm above the vertical plane of Figure 5.13b. The two MIPs reveal a clear change in imaging depth, with vasculature on the left side of the ROI fading out of the image plane and vasculature on the right side of the ROI becoming discernible and less blurry, respectively. However, the sample also moved laterally in between the scans, as indicated by the movement of a vascular junction which is highlighted by a white arrow in Figure 5.13a and Figure 5.13b, respectively. Here, the relative movement corresponded to a lateral shift of around minus 30 μm along the x-axis and around minus 55 μm along the y-axis. This lateral movement of the sample was induced by the weight of the mouse pushing onto the PE-foil and the

successive bending of the foil at the aperture of the sample-holder. This effect was not detectable when imaging mouse ears or suture samples, where sample weight was negligible. However, in the case of mouse ear imaging (see section 8.3), a bending of the sample was observed along the same axis, corresponding to the longer side of the rectangular aperture in the sample-holder.

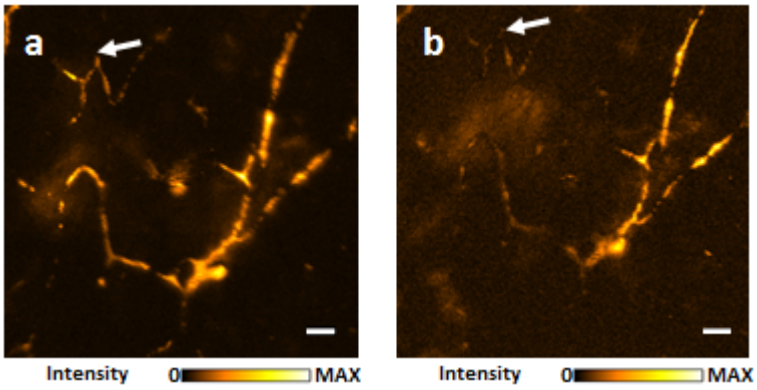

Figure 5.13: Consistency of the sensor-head performance at different image depths: Optoacoustic microscopy images from the ROI indicated in Figure 5.13, with image (a) recorded at a depth of 100 μm above image (b). White arrows: lateral position of an exemplary vascular junction shifting unintentionally. Scale bar, 50 μm.

5.5 Conclusion and Discussion

The sensor-head discussed in this chapter was successfully demonstrated as a novel approach for all-optical ultrasound detection and enabled reflection-mode optoacoustic microscopy. In the context of biomedical microscopy applications, the sensor-head allowed for the simultaneous implementation of the optoacoustic modality alongside existing imaging modalities - such as multi-photon microscopy - into existing and readily available off-the-shelf microscopes.

The fundamental concept of the sensor-head was based on a π-FBG embedded inside an ellipsoidal acoustic cavity whose acoustic amplification enhanced its sensitivity. Hence, the π-FBG did not necessarily rely on a cost-intensive and complex interrogation setup such as the CRPI method that was introduced in chapter 4. While the theoretical acoustic amplification yielded a factor of 14, the effective amplification had a factor of around 5. Here, surface imperfections originating in technical limitations in the prototype-like manufacturing process, losses at the solid/fluid interface that affected both amplitude

and phase of reflected acoustic waves as well as the attenuation of high frequencies during the passage through the acoustic cavity contributed to this deprivation. In future experiments, the sensitivity of the acoustic cavity may be straightforwardly improved by employing π-FBGs fashioned inside polymer fibers or thin-clad fiber geometries [114, 130] as well as by employing π-FBGs written into polymer slabs [131, 132] for improved acoustic coupling. Furthermore, the bandwidth could be improved by decreasing the size of the ellipsoid and therefore the frequency dependent attenuation of traversing acoustic signals. Nevertheless, the sensor-head achieved a sensitivity of 88 Pa, which was five times higher than that of a plain π-FBG interrogated by a cw-laser and even slightly more sensitive (factor 1.13) than a π-FBG interrogated by a CRPI system as described in section 4.3 [24, 60, 103].

An approach to further improve the sensitivity of the sensor-head lays within the π-FBG: Increasing the overall grating length [62] or increasing its coupling ceofficient [133] would increase its Q-factor and therefore its sensitivity. As downside, this approach would require a cw-laser with an ultra-narrow linewidth and would hence introduce additional challenges, such as the need for feedback circuits that continuously tune the laser to the FWHM of the resonance. Next to the actual sensor sensitivity, the dynamic range of a given ultrasound sensor may also limit its applicability and was therefore investigated. Here, it proved advantageous that the signal amplification by the acoustic cavity did not amplify the optical noise inherent to interrogation-system, as e.g. a downstream optical or an electrical amplifier would have done. Moreover, π-FBGs exhibit a linear response to acoustic pressure of up to 0.75 MPa [62] and therefore even optoacoustic signals amplified by the acoustic cavity, typically in the range of few tens of Pa times the amplification factor of 5 (see section 8.1), were well within the dynamic range of the overall sensor-head. If the dynamic range was exceeded, e.g. in a tomographic application with a wider acoustic pressure range, PI or CRPI interrogation methods could still be applied, with the dual advantage of improved sensitivity and extended dynamic range [60, 103]. Following this line of thought, the suggested sensor-head could reach sensitivities exceeding 20 Pa (NEP) when combined with CRPI. However, the complexity and limited cost-effectiveness of the CRPI system might again impede a broad applicability of the sensor-head.

Comparing the sensor-head to other all-optical ultrasound detectors for reflection-mode microscopy, optical micro-rings currently offer the only alternative in terms of sensitivity and bandwidth (see chapter 3). Yet, micro-rings are highly limited in their detection angle, with the suggested sensor-head exhibiting a FOV around 40 times wider than

that of micro-rings. Moreover, micro-rings are commonly manufactured atop of carrier substrates and are consequently rather fragile regarding e.g. physical contact to biological specimen as well as the coupling medium itself.

A number of biomedical imaging applications might benefit from the presented sensor design, as it allows for a comparatively easy implementation into existing microscopy setups with reflection-mode geometries. The latter is of particular importance, as anatomic and functional analysis often relies on μm precision imaging within bulky samples. Exemplarily, only blood vessels sized 100 μm and more can be currently monitored with in-depth imaging of high-resolution pulse-echo ultrasound transducers. Furthermore, there are no established technologies for the monitoring of structural and functional behaviour of smaller blood vessels *in vivo* and without the application of contrast agents [134].

The sensor-head also highlighted the non-invasive nature of optoacoustic imaging, as no contrast agents were administered and the applied laser fluence was kept below 15 $\frac{mJ}{cm^2}$ when imaging *in vivo* at depths exceeding 50 μm. Hence the laser fluence was well below the ANSI standard for maximum permitted laser fluence of 20 $\frac{mJ}{cm^2}$. These sensing capabilities might be utilized in the field of non-invasive pathophysiological hypertension studies, where structural alterations in the lumen/diameter ratio of micro-vasculature are investigated [135]. Another possible application might be the study on structural alterations of micro-vessels, such as abnormal angiogenesis and pathological vascularisation, which have been proposed as hallmarks of a range of neoplasia [136].

In summary, the suggested sensor-head was demonstrated to examine and image delicate vascular structures both in thin (mouse ear) and thick (mouse abdomen) samples, without the limitations formerly applied by the use of piezoelectric ultrasound detectors. The system imaged microvasculature and capillaries as small a 6 μm at a depth of 300 μm. In combination with hybrid SHG imaging of surrounding collagen layers, its great potential for applications in both biomedical research as well as in actual clinical applications could be demonstrated.

6 Asymmetric Etalons

6.1 Introduction

Two applications were demonstrated in chapter 4 and chapter 5, where optical ultrasound detection based on $\pi-$FBGs had fundamental advantages over the implementation of piezoelectric ultrasound detectors as well as over most other prevalent optical sensing approaches. In these studies, ultrasound detection was performed at bandwidths between 10 and 30 MHz at central frequencies of up to 70 MHz and with sensitivities of up to 100 Pa (NEP). This performance was demonstrated to be sufficient to sense micron-sized optical absorbers in tissue. Moreover, the ultra-small footprint of the fiber based resonators allowed to implement the optoacoustic imaging modality into existing microscopy setups, leading to multi-modal imaging of thick specimen in reflection-mode geometries.
However, there are a number of aspects about $\pi-$FBGs that prevent their widespread application as ultrasound detectors, in particular in applications related to optoacoustic tomography. Here, the cylindrical resonator geometry with effective sensing dimensions of around 100 μm in diameter and 300 μm in length [24, 62] results in a suboptimal sensitivity field as opposed to a point-like ultrasound detector in an ideal scenario for tomographic image reconstruction (see discussion in subsection 2.3.1) [14, 39], leaving $\pi-$FBGs inept for high-resolution tomography. Moreover, the optical fibers that house the $\pi-$FBGs have minimum bending radii of around 20 mm to 30 mm, depending on the cladding diameter applied. While favourable for certain side-looking applications, such as optoacoustic endoscopy, this geometrical constraint makes fiber-based resonators not suitable for creating compact and dense 2D or 3D sensor arrays that expedite tomographic image acquisition. Another drawback of the cylindrical geometry becomes apparent when investigating the frequency response of $\pi-$FBGs as presented in chapter 4 and Figure 4.9, where the bandwidth had two separate bands of around 7 MHz to 27 MHz and 62 MHz to 77 MHz, respectively. Without destructive interference of the acoustic waves within the silica fiber [60, 114], the frequency response would have a more persistent shape, possibly exceeding its cut-off at around 80 MHz.

In order to convert the specifications of both point-like sensing geometry and extended frequency response into enhanced optoacoustic imaging, a sensor was devised with the following four aspects in mind:

1. The sensor should be based on a $\pi-$FBG resonator, thus transferring existing features, such as the superior light confinement and the resulting high Q-factor as well as the ultra-small footprint into the novel design [62].

2. The sensor should be designed in a way to allow for acoustic waves to interact with the resonator along its optical axis (corresponding to the fiber axis in the case of a $\pi-$FBG) rather than perpendicular to it, analogous to the operating principle of FPs installed on fiber tips [61, 137].

3. The sensor should be able to be driven by the same interrogation and read-out systems as applied for the $\pi-$FBG (see chapter 4), e.g. allowing to apply shot-noise limited interrogation as well as multiplexing approaches via PI and CRPI interrogation [60, 103].

4. The sensor should exhibit a bandwidth of more than 100 MHz, exceeding that of common piezoelectric transducers as well as that of most prevalent optical ultrasound detectors. This might be facilitated e.g. by further reducing the effective sensing size of the optical cavity, which is ultimately also governed by the length of the Bragg gratings applied (e.g. 300 μm effective sensing length and 2 mm overall grating length [62]).

Following these requirements, a novel optical resonator was derived and manufactured in a number of iterations. The central approach was to utilize a π-FBG and to replace one of the Bragg gratings that constitutes one of the distributed optical reflectors by a non-distributed reflector, e.g. a plain mirror surface attached to the fiber facet. The fundamental design is depicted in Figure 6.1 in an optical fiber embodiment and in comparison to the composition and geometry of a π-FBG.
In the π-FBG illustrated in Figure 6.1a, the waveguide volume along the optical axis of the fiber core corresponds to the π-phase shifted region at the center of the optical resonator. For the novel sensor geometry, the right side of the π-FBG was then replaced by a reflecting element installed directly adjacent to the fiber facet, as depicted in yellow in Figure 6.1b. Light entering the optical cavity through the Bragg grating, will then be trapped in the optical resonator constituted by the Bragg grating on the left side and

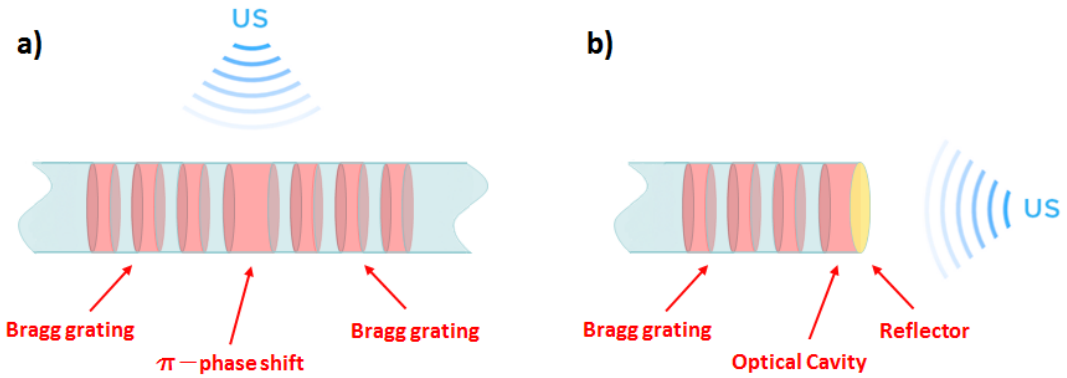

Figure 6.1: Schematic of the fiber-based AsE concept: (a) π-FBG with ultrasound perturbing the fiber perpendicular to the optical axis of the resonator. (b) AsE design, with the resonator formed by a Bragg grating on the left side and a reflector on the right side of the optical cavity, respectively. The AsE design allows to detect ultrasound perturbations along the optical axis of the resonator.

the reflector introduced on the fiber facet on the right side. Inspired by its asymmetric structure, the novel optical resonator was named Asymmetric Etalon (**AsE**).
A number of different approaches are conceivable when manufacturing an AsE sensor, in particular depending on the type of waveguide applied. In the following chapter, AsE manufacture is illustrated based on Bragg gratings in standard optical fibers and the sensor is then characterized in terms of sensitivity, bandwidth and detection angle.

6.2 Materials and Methods

6.2.1 Demonstrator Manufacture

The fiber-based AsE sensor was based on commercial transmission-mode π-FBGs (TeraXion, Quebec, Canada), whose physical dimensions introduced a number of challenges when investigating means of how to manufacture the AsE sensors. These commercial π-FBGs were based on a single-mode and polarisation maintaining SMF-28 fiber with a core diameter of 10.5 μm, a cladding diameter of 125 μm and an acrylic coating diameter of around 245 μm. The fibers were connectorized with standard FC/APC connectors at the arbitrary input and output side. For Bragg grating inscription with high-intensity UV light and phase mask [138], the π-FBGs had to be uncoated over the desired length to allow close contact with the phase mask. In order to protect the base cladding after inscription, the inscribed area was then recoated with a UV-cured polymer resin, introducing a slightly enlarged coating diameter of around 280 μm.

Transitioning these dimensions to the manufacture of an AsE sensor, the process required the fibers to be cleaved at a position close enough to the center of the π-FBG to allow for the removal of the excess fiber on the respective side of the phase shift, opposite from the remaining Bragg grating. Additionally, a clean fiber cleave required to remove the polymer coating from the recoated area covering the grating length. Hence, the fiber facet would have been particularly fragile without its protection coating during the extended polishing, rendering a polish of the bare fiber non-viable. A solution was conceived by installing the uncoated fiber into a ceramic ferule prior to polishing. Such ferules are typically employed when connectorizing optical FC/PC fibers and are commercially available at different core diameters and lengths. In order to cope for the enlarged coating diameter of the recoated fiber, a multimode ferule with an inner diameter of 300 μm was chosen for the first iterations, with the cleaved fiber adhered inside by the low-viscosity epoxy. The ceramic ferules were then installed into a custom-made polishing disc and the facet of the ferule and fiber could then be polished with nm precision by standardized optical fiber polishing and lapping supplies (diamond laminated polishing and lapping papers, with grit sizes between 20 nm and 30 μm). Here, the initial polishing processes were performed iteratively, slowly approaching the position of the phase-shift along the fiber core.

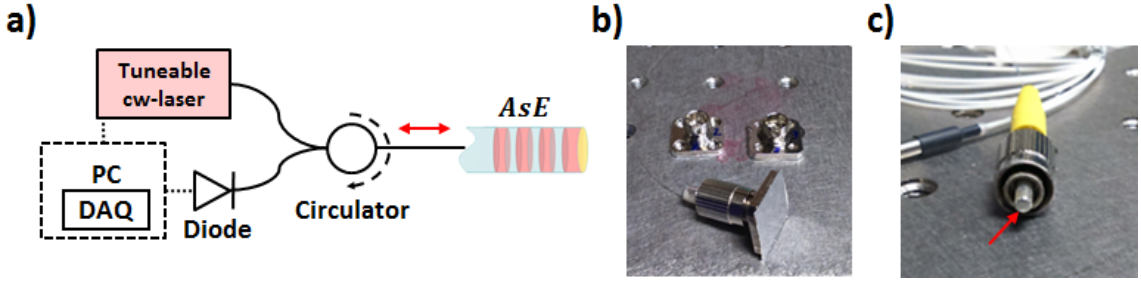

Figure 6.2: AsE read-out and demonstrator design: (a) A tuneable cw-laser in the C-band was applied to interrogate the AsE during manufacture, utilizing a circulator for the read-out of the reflected spectrum. (b) Customized fiber coupling frame with an attached Al-foil as reflector. (c) Chemically deposited Ag-layer atop the facet of AsE and ceramic ferule (indicated by red arrow).

The spectrum of the fiber was continuously read-out throughout the polishing process, which allowed to observe the decomposition of the Bragg grating on the one hand and to observe the polishing progress on the other hand. Here, the reflection read-out is depicted in Figure 6.2a and was performed with a cw-laser (INTUN TL1550-B; Thorlabs, Newton, USA) and a high bandwidth photodiode (30 kHz - 1.6 GHz PDB480C-AC; Thorlabs, Newton, USA). During this process, the reflecting surface of the AsE was introduced

by an Aluminium foil installed onto the metallic frame of a customized fiber coupler, as depicted in Figure 6.2b, allowing to safely introduce the AsE relative to the reflector along its ceramic cylinder. For a better optical coupling, the coupler was filled with index matching fluid suitable for optical fiber connections.
After final polishing of the combined fiber and ferule facet to an optical grade (optical-flat) exceeding around $\frac{\lambda}{10}$, a reflection layer was deposited chemically onto the ceramic ferule using a silver nitrate reaction. This process was performed without removing the AsE from the ferule and the resulting reflective layer on the facet is depicted in Figure 6.2c.

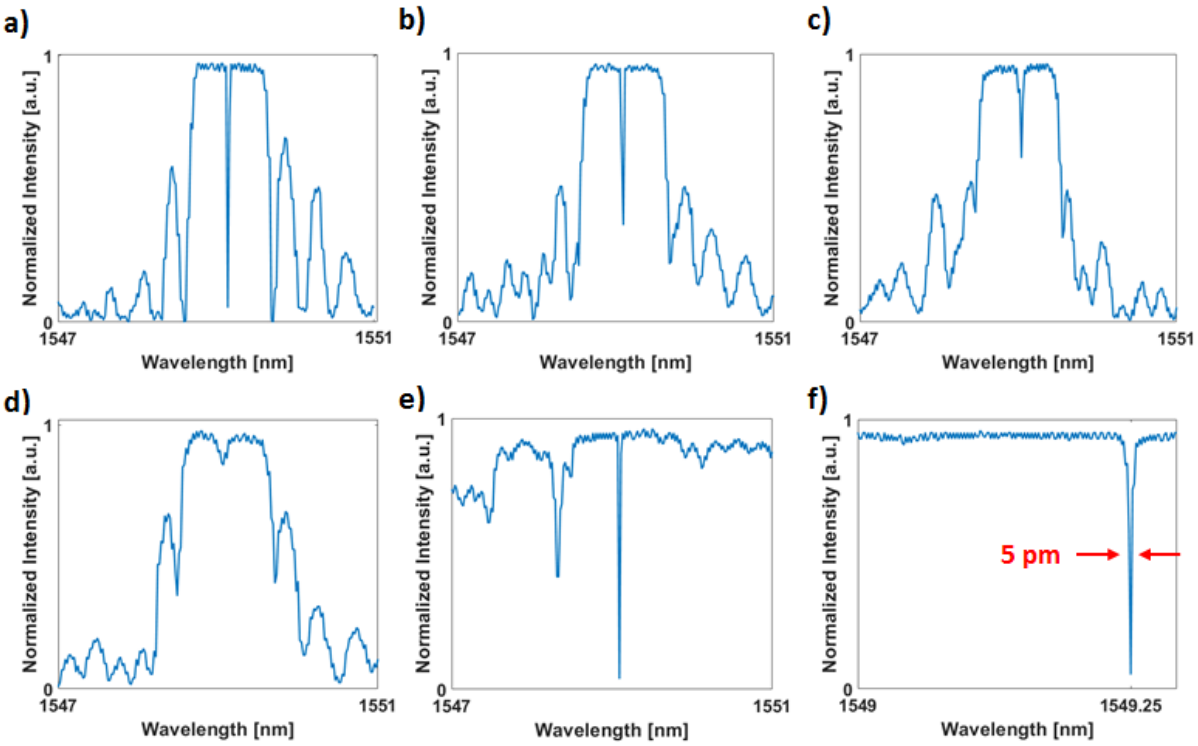

Figure 6.3: Evolution of AsE spectra during manufacture: (a) Original π-FBG spectrum before fiber polish. (b)-(d) Resonance reduction during the polishing process. (e) Application of a broad-bandwidth reflector leads to a resonance and fading of the characteristic band-gap. (f) Spectral close-up of the new resonance notch, revealing a FWHM of around 5 pm at a central wavelength of 1549.25 nm.

Before polishing, the initial resonance notch of the π-FBG is depicted in Figure 6.3a and was located at 1549.13 nm with a transmission at the resonance of 93.4 %. The fiber was then polished and the reflection spectrum was iteratively recorded during the process. Figure 6.3b to Figure 6.3d reveal the decomposition of the Bragg grating and in particular of the resonance. The shortening of the Bragg grating also affected the side lobes adjacent to the characteristic band-gap of π-FBGs.

Figure 6.3e was recorded with the polished fiber facet introduced to the Al-foil as depicted in Figure 6.2. Here, the band-gap is mostly gone, due to a broad-bandwidth reflection at the Al-foil. Furthermore, a new resonance notch reappeared in the spectrum, with a reflection intensity in the same order as the one of the initial π-FBG. Figure 6.3f then shows the result after the final polishing step, with a close-up of the spectrum depicting the central resonance positioned at 1549.25 nm as well as revealing a notch FWHM of 5 pm.
Throughout the experiments in this chapter, the manufacturing process was iteratively improved. By designing a polishing device that allowed to handle the delicate fibers, AsE sensors could be manufactured without the need of a protecting ceramic sleeve. Furthermore, the reflection layer was applied professionally by sputter deposition atop the 125 μm fiber facet, with a bonding layer of titanium of around 5 nm thickness and an adjacent reflection layer of gold of around 200 nm thickness (Ara-Coatings GmbH, Erlangen, Germany). Besides the alterations within the manufacturing process, the overall fiber based AsE design (including i.e. the AsE spectra) was consistent for the characterization and experiments presented in this work.

6.2.2 Experimental Setup

The proposed AsE design corresponds to the outline of a classic FP cavity, which allowed to transfer prevalent setup designs to the new sensor. The experimental setup of the AsE characterization is depicted in Figure 6.4 and in analogy to subsection 4.2.1, the overall system can be divided into three sections:

1. Light delivery and beam adjustment for optoacoustic signal excitation.
2. An inverted microscope for high-precision sample and sensor alignment.
3. The AsE sensor and its read-out system for the recording of optoacoustic signals.

Optoacoustic excitation was performed by a passively Q-switched 515 nm pulsed DPSS laser with a repetition rate adjustable between single shot and 2 kHz, a maximum pulse energy of 1 mJ and a pulse width of 0.9 ns (Wedge HB532 2W; Bright Solutions SRL, Pavia, Italy). For the sake of acquisition speed, the pulse rate was usually kept at 2 kHz. Stray light at the laser output was captured by a photo diode (DET 36A; Thorlabs, Newton, USA) and utilized for signal triggering. Depending on the respective sample, the laser beam was then attenuated by neutral density filters, resized and collimated by a

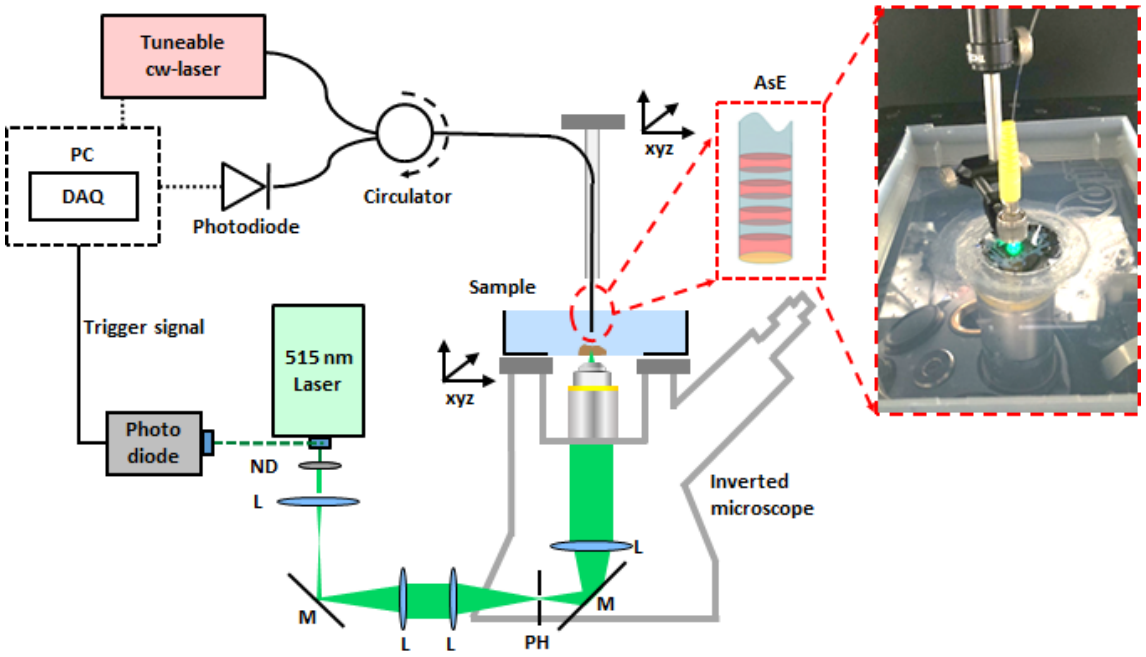

Figure 6.4: Schematic of the AsE-sensor characterization setup: Optoacoustic signal excitation performed by a 2 kHz 532 nm laser. AsE read-out based on cw-laser interrogation via an optical circulator. Inlet: AsE installed atop the illuminated sample and focal plane, protected by a FC/PC fiber connector. AsE, ultrasound sensor; DAQ, data acquisition card; L, lens; M, mirror; ND, neutral density filter; PH, pinhole.

set of telescopes and guided through a 20 μm pinhole for spatial filtering. The collimated beam was then guided into a 10x microscope objective (PLN 10x; Olympus, Hamburg, Germany) with a NA of 0.25 and a WD of 10.6 mm. In analogy to the experiments demonstrated in chapter 4 and subsection 5.2.2, the lateral resolution was governed by the optical properties of the setup and corresponded to a lateral resolution of $\approx$ 2.2 μm. In contrast, the axial resolution was estimated to exceed 5 μm following the AsE bandwidth discussed later in this chapter.

The objective was installed inside a customized inverted microscope (Diaphot Inverted Tissue Culture Microscope; Nikon, Tokyo, Japan), where all original optical components and translational stages were cored. As the microscope was not intended for brightfield microscopy, also the trans-illumination was removed and an xyz-set of translational stages (MTS25-Z8 assembly; Thorlabs) was installed for AsE positioning. Sample positioning was performed by high-precision piezoelectric linear stages with a minimum step size of 100 nm (xy-stage: MLS203-2, z-stage: ZMZS500-E; Thorlabs), which were attached to the microscope by a solid adaptor of cnc-carved aluminium. Depending on the respective

samples, custom made 3D-printed or cnc-carved water tanks and sample holders were installed inside the aperture of the lower set of xyz translational stages. The focal/imaging plane could be adjusted accordingly by positioning the objective along a lateral leeway of 20 mm.

In contrast to the implementation of the π-FBG in chapter 4, samples studied by AsE were usually directly restrained onto transparent 170 μm cover slips by tape and instead of a water bath, it was sufficient to apply a few droplets of deionized water between the fiber facet and the sample for acoustic coupling.

The detection of optoacoustic signals was performed in a similar manner to the sensor read-out described in chapter 5. A tuneable cw-laser (INTUN TL1550-B; Thorlabs) with a maximum power of 20 mW was used to interrogate the AsE in reflection mode by tuning the laser towards the spectral position of the FWHM of the AsE resonance. Due to the narrow resonance of the AsE sensor, it is relevant to note that the spectral linewidth of the cw-laser was 150 kHz and that the minimum spectral tuning step size corresponded to 0.2 pm. Reflection from the AsE was then separated from the interrogating illumination by an optical circulator and forwarded towards an ultra-high speed InGaAs photodiode (PDB480C-AC; Thorlabs) with a bandwidth of 1.6 GHz. Commonly, the cw-laser was driven at powers between 3 dBm (around 2 mW) and 9 dBm (around 8 mW) in order not to saturate the photodiodes. Optoacoustic signals were then recorded by a variety of DAQ cards with various sampling rates, ranging from 500 MHz (ADQ412; SP Devices, Linkoeping, Sweden) to 1.5 GHz (GaGe EON Express; Dynamic Systems, Lockport, USA). Data acquisition and processing was performed by a Matlab script, which was applied for sample and sensor alignment as well.

6.3 Etalon Characterization

6.3.1 Sensitivity and Reception Angle

As in any FP type interferometer employed for the detection of ultrasound signals, AsE sensitivity towards acoustic signals was governed by the capacity of the sensor to convert acoustically induced pressure variations into corresponding spectral shifts. For sensor characterization, optoacoustic signals were generated by focusing the excitation laser onto a strip of 125 μm thick black rubber tape (polyvinyl chloride) and position the AsE at a distance of 0.5 mm atop of the focal spot. Signals were then recorded with 100 fold averaging and perpendicular line scans across the focal spot over 400 μm distance

are depicted in Figure 6.5a and Figure 6.5b, respectively. Note that in contrast to the B-scans of the π-FBG (Figure 4.8), the scans are symmetrical in both axis due to the forward-looking and symmetric nature of the AsE. Moreover, the steep signal incline relative to the focal spot emphasizes the small footprint of the AsE fiber facet, in particular compared to the flat response of the π-FBG when scanned in parallel to the fiber axis as depicted in Figure 4.8a.

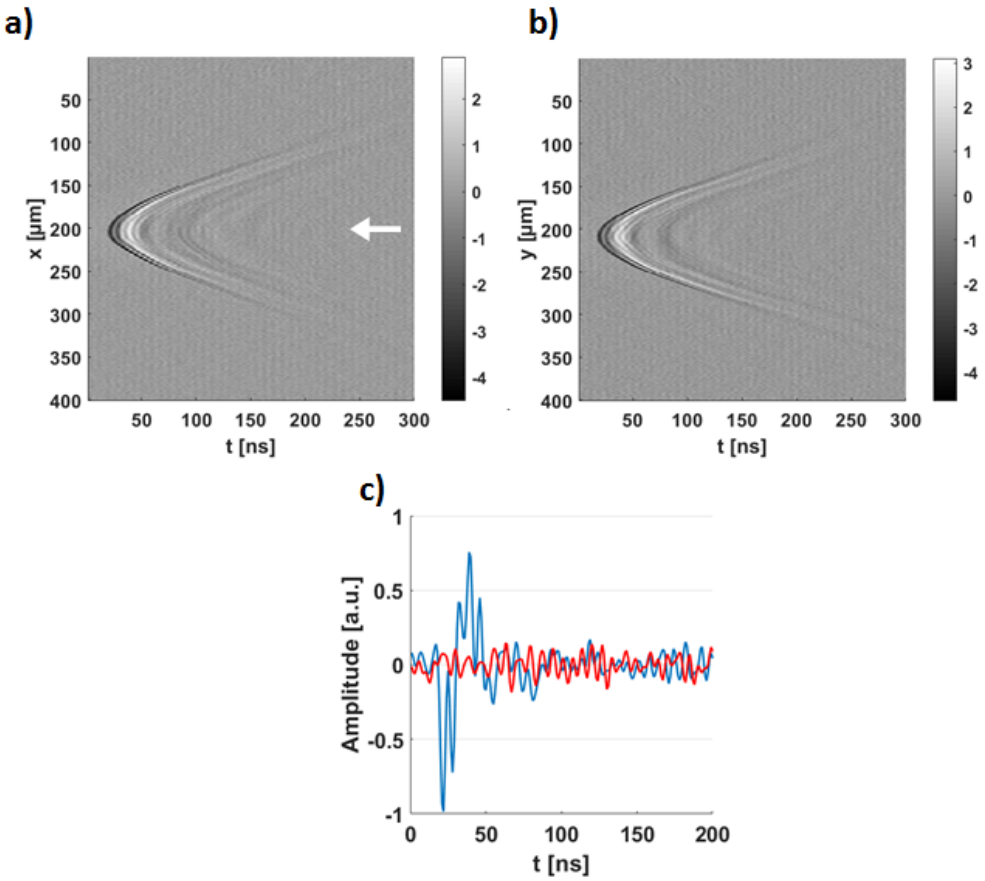

Figure 6.5: AsE - optoacoustic sensing in time domain: (a) and (b) perpendicular unfiltered B-scans across an optoacoustic point source underline the ultra-small AsE footprint. (c) Close-up of the filtered acoustic signal (blue) and corresponding noise recording (red) of the signal indicated by a white arrow in (a).

Figure 6.5c depicts a close-up of the A-scan recorded at the point indicated by a white arrow in Figure 6.5a. A bandpass filter between 5 MHz and 200 MHz was applied onto the acoustic signal and its corresponding noise recording. Signal analysis revealed a SNR of around 9.5 dB, mainly governed by the relatively weak power of the excitation laser of around 800 nJ pulse energy to avoid thermal damage on the thin absorber.
The actual AsE sensitivity was determined by the calibration with the help of a VDF

hydrophone (0.5 mm needle hydrophone; Precision Acoustics Ltd, Dorchester, UK) along an optoacoustic source constituted by a 50 μm black polystyrene microsphere (Polybead; Polysciences, Warrington, USA) that was embedded inside an agar matrix and illuminated by diffused laser light with a pulse energy in the order of 10 μJ. The AsE and the hydrophone were then positioned at a distance of 725 μm atop the microsphere and acoustic signals were recorded without averaging and subsequent signal analysis revealed a sensitivity in terms of NEP of around 50 Pa.

The reception angle of a given sensor is crucial for signal acquisition in tomographic applications [49] as well as for applications where resolution is determined by a scanned optical focus [29, 40] and the reception angle therefore defines the maximum achievable ROI. In the case of the AsE, the reception angle was determined by the help of an acoustic point source constituted by 125 μm thick PVC tape as described above. With an optical focus of around 2.2 μm, the acoustic source was scanned from atop by xy-scanning it over 1.6 mm x 1.6 mm with the AsE positioned at a distance of 0.5 mm and with a step size of 25 μm. The resulting sensitivity map of the AsE is depicted in Figure 6.6a and in analogy to the B-scan, the symmetrical nature of the sensor became apparent. A 1D scan across the center of the acoustic source with identical step size along a distance of 6 mm was then performed and is depicted in Figure 6.6b. Here, the individual amplitude is depicted as red dots and the smoothed fit is depicted in blue. Calculating the averaged angle over which the amplitude remains above -6 dB then revealed the overall reception angle of around 80°.

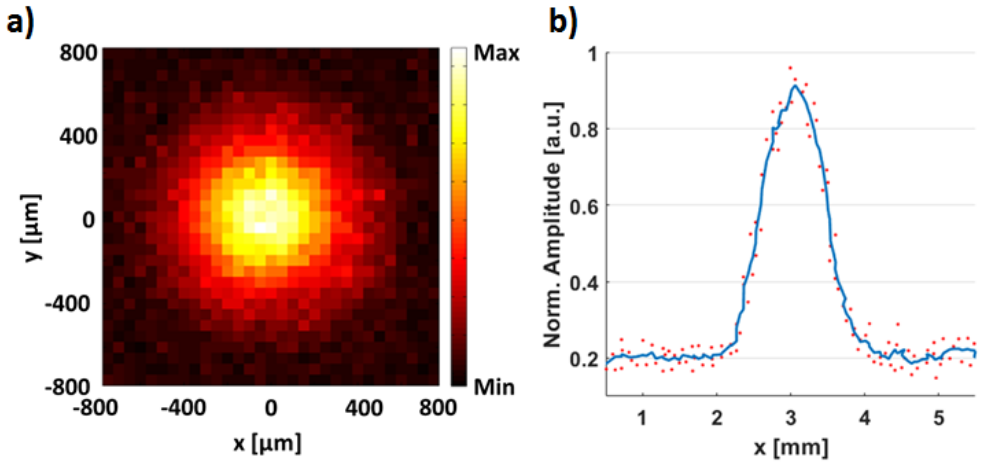

Figure 6.6: AsE sensitivity field and reception angle: (a) AsE scanned across a stationary acoustic point-source at a distance of 0.5 mm and a step size of 25 μm. (b) AsE line scan across the center of the acoustic source depicted in (a), with individual recorded amplitudes in red and the smoothed fit in blue. Step size, 25 μm.

6.3.2 Frequency Response

A major aim of the AsE principle was to achieve a high frequency response with a central frequency high enough to differentiate absorbers sized 10 μm and below in tomographic applications. Hence it was vital to increase the frequency response and bandwidth compared to π-FBGs as well as investigating e.g. acoustic resonances inside the AsE that might arise in analogy to the response depicted in Figure 4.9, where the bandwidth was separated into two distinct bands.
For AsE bandwidth characterization, a custom absorber was created by sputter deposition onto a microscopy cover slip with a thickness of 170 μm (# 1.5 norm), with a bonding layer of titanium of around 5 nm thickness and an adjacent layer of gold of around 200 nm thickness (Ara-Coatings GmbH, Erlangen, Germany). This phantom was then illuminated by the optoacoustic microscopy setup, in a way similar to the illumination of the rubber band in subsection 6.3.1 with a pulse energy of around 10 nJ, and the Ase was positioned centrally atop the source at a distance of around 300 μm. Acoustic matching was performed by a water drop. The acoustic signal was then averaged 10.000 times and the corresponding Fourier transform is depicted in Figure 6.7.

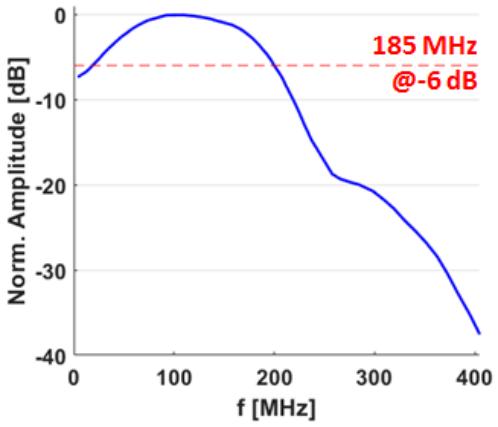

Figure 6.7: Bandwidth characterization of the AsE: AsE frequency response towards a broadband acoustic point source revealing peak sensitivity towards signals around 103 MHz and an overall bandwidth of 185 MHz at -6 dB.

The frequency response shows a peak sensitivity towards acoustic signals of 103 MHz and indicated an overall bandwidth of around 185 MHz at -6 dB spanning from 15 MHz up to 200 MHz. Note that in contrast to the π-FBG bandwidth, the AsE response is not divided into bands and is descending almost symmetrically around the peak except for a step at around 150 MHz.

6.4 AsE Applications

6.4.1 Optoacoustic Endoscopy

As discussed in the introduction (see chapter 1), optoacoustic endoscopy may represent the most challenging demands in terms of sensitivity and footprint towards acoustic sensors and was therefore one of the main incentives for the development of the AsE sensors. The forward-looking geometry of the AsE allows to apply the sensor in novel modalities, such as forward-looking endoscopy of vascular occlusions [18, 139]. Moreover, there are existing applications that actually demand the use of forward looking detectors, such as optoacoustic cystoscopy [140]. Here, the optoacoustic modality is particularly advantageous, as optoacoustic depth analysis could limit the need for biopsies in the case of bladder cancer and make surgical interventions more efficient. In order to verify the fundamental applicability of the AsE sensor for cystoscopy, an experimental setup was derived that exceeded previous designs as e.g. presented in the pilot study of Kamaya et al. [140]. Firstly, the system was supposed to reach a resolution governed by the optical focus. Secondly, a light delivery tailored towards forward-looking cystoscopy was to be utilized rather than using unfocused free-beam illumination.

Experimental Setup

These requirements were translated into the setup as depicted in Figure 6.8, where illumination was implemented by fiber-based light delivery together with a gradient-index (**GRIN**) lens for optical focusing. Here, the light-carrying optical fiber was a standard SMF-28 fiber with a 10 μm fiber-core diameter and was attached to a GRIN lens via a thin metallic housing. In turn, the GRIN housing was installed inside a metallic sleeve with a 0.5 mm thick flat window (AR coated) at its aperture to allow for immersion in the acoustic coupling medium. The AsE was then attached to a slit implemented inside the sleeve and fixated in level to the window at the bottom of the sleeve with capton tape. The GRIN lens had an actual working distance of around 3.54 mm and was placed inside the sheath at a distance of around 1.5 mm to the level of the AsE. The overall probe size was then around 2.8 mm in diameter and 30 mm in length, serving the requirements of cystoscopy. Corresponding to the core diameter of the SMF fiber, the probe could be estimated to have an effective optical resolution of around 10 μm minimum. AsE interrogation and acoustic signal read-out were performed as described above (subsection 6.2.2) and dual scanning was performed by installing the carrier sleeve inside a 3D-printed holder into the upper set of xyz-stages.

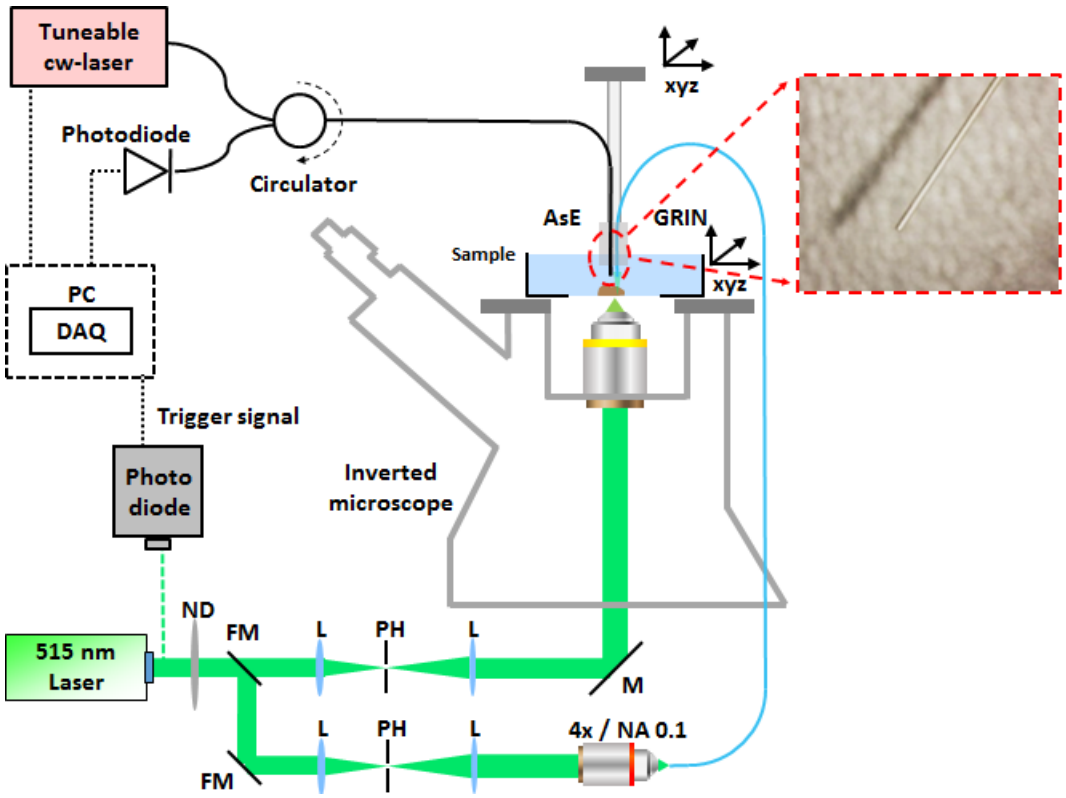

Figure 6.8: Demonstrator for AsE endoscopy: Combined optoacoustic endoscopy and microscopy setup: an alternative light path allows for fiber coupling into a multimode fiber and subsequent focusing by a GRIN lens. Inlet: Close-up photograph of a fiber based AsE of 125 μm diameter as installed adjacent to the grin lens. AsE, ultrasound sensor; DAQ, data acquisition card; FM, flip mount mirror; GRIN, gradient-index lens; L, lens; M, mirror; ND, neutral density filter; PH, pinhole.

Ex Vivo Imaging with Endoscopic Probe

In analogy to optoacoustic microscopy of thick samples as presented in chapter 5, optoacoustic endoscopy usually works in favourable reflection-mode imaging. Here, *ex vivo* or *in vivo* samples do not necessarily need to be excised or prepared for imaging, nor do they need to be thinner than around 0.5 - 1 mm as in the case of transmission-mode optoacoustic microscopy [37].

Nevertheless, nude mouse models were the sample of choice for initial experiments with the AsE, due to their high vascular density as well as the comparability with imaging performances obtained e.g. with piezoelectric detectors [27] or pi-FBGs [35, 60]. The experiments were performed with mouse ears from sacrificed female Nude-1 Foxn1 mice aged around 12 weeks and the ears were cauterized immediately after excision to prevent the outflow of blood. The ears were fixated at the bottom of a 35 mm microscopy Petri

dish and installed onto the microscopy stage below the optical axis of the grin lens. The dish was filled with deionized water for acoustic coupling and the distance of the AsE set to 1.7 mm above the fixated ear pinna. For accurate adjustment, the effective working distance of the grin lens could be matched to the AsE installation height by translating the grin lens vertically inside the sleeve. Due to a more suitable beam-shape for optical coupling, the 532 nm pulsed laser was replaced by a passively Q-switched 515 nm pulsed DPSS laser with a repetition rate fixed at 1.2 kHz, a maximum pulse energy of 570 μJ and pulse width of 1.8 ns (Flare HP PQ Green 2 k-500; Innolight GmbH, Hannover, Germany). The light path and remaining microscopy setup as well as the trigger diode was identical to the setup as described in subsection 6.2.2. The pulse energy of the fiber-coupled illumination light could be varied by ND filters prior to the coupling, but was effectively limited to a maximum of around 20 μJ per pulse in order to avoid thermal damage to the coupled fiber facet as well as to the grin lens. The latter was glued to its sleeve by UV curable epoxy which could dissolve at higher temperatures induced e.g. by stray light within the sleeve. Note that these energy levels are 10 to 20 times higher than the sub-μJ energies per pulse used in optoacoustic microscopy (see chapter 4 and chapter 5), which is mitigated by the long working distance of the grin lens and in particular by the around 20 times wider optical focus of the AsE probe.

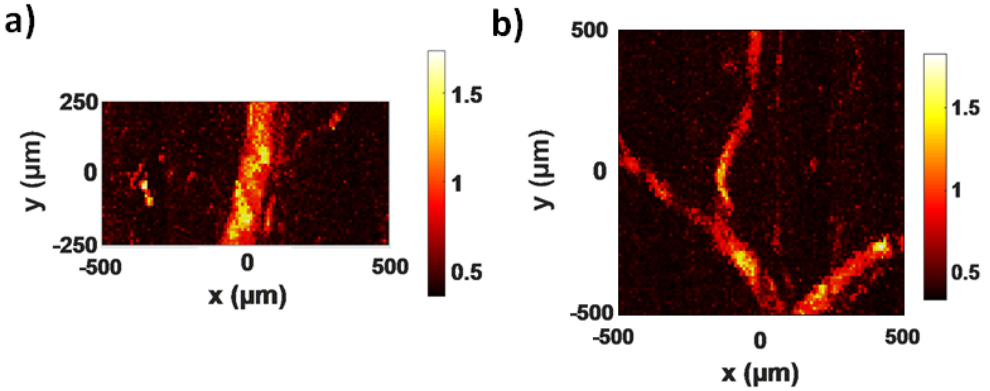

Figure 6.9: Ex vivo imaging with an endoscopic AsE probe: (a) and (b) Optoacoustic top-view MIP of two sections of an excised mouse ear revealing a subcutaneous artery/vein pair and branching arteries, respectively. Pixel size, 10 μm x 10 μm.

For optoacoustic imaging, the AsE probe head was scanned above the mouse ear by the upper set of xyz-stages and the resulting MIPs are presented in Figure 6.9a and Figure 6.9b. The recorded acoustic signals were averaged 100 times and a bandpass filter between 4 MHz and 100 MHz was applied onto the data. Both MIPs were scanned with a step-size of 10 μm and FOVs of 1 mm x 0.5 mm and 1 mm x 1 mm, respectively. The

images depict an artery/vein pair as well as the branching of arteries at the upper inner pinna of the mouse ear. Assuming a resolution of 10 μm, the individual vessel diameters ranged from around 20 μm up to 120 μm in size.

Compared to previous measurements of similar samples, the images suffer from a relatively low SNR of around 7 dB. The main reason for the low sensitivity was the displacement of the AsE relative to the optical axis of the grin-lens, which was owed to the geometry of the probe head as well as to the diameter of the grin-lens and its housing sleeve. In order to estimate the loss of sensitivity caused by this off-center geometry, the AsE sensitivity-map as depicted in subsection 6.3.1 was extrapolated for a relative distance between AsE and optical axis of 1.7 mm. The resulting loss of the maximum sensitivity achievable was then found to be in the order of -6.5 dB. Note that this is just an estimation and does not include the added acoustic attenuation especially for higher frequencies as induced by the extended acoustic pathway compared to the recording of the initial sensitivity map.

Nevertheless, these initial *ex vivo* experiments successfully showcased the AsE applicability for optoacoustic imaging for the first time. Moreover, the ultra-small footprint of the AsE proved to be advantageous for the implementation into endoscopy probes designed and suitably sized for cystoscopy.

6.4.2 AsE in Ionoacoustics

A second application for the AsE detector was found in the relatively novel field of ionoacoustics, which describes a way to determine the depth and location of energy deposition during *in vivo* particle therapy and in particular in proton therapy. Although not connected to optoacoustic imaging at first glance, ion-absorption in matter causes the excitation of acoustic waves, similarily to the photoacoustic effect.

Protons entering a medium such as water or tissue deposit their energy predominantly by interaction with prevalent electrons via electromagnetic Coulomb interactions [141]. Here, the energy loss for penetrating ions over a depth z inside a given medium with a density of ρ is commonly indicated by the stopping power S of ions with energy E. $S(E)$ can then be derived as [141]:

$$S(E) = \frac{1}{\rho}\frac{\partial E}{\partial z} \tag{6.1}$$

The Bethe-Bloch equation then states the analytical description for $S(E)$ for charged particles with masses much bigger relative to the electron mass as

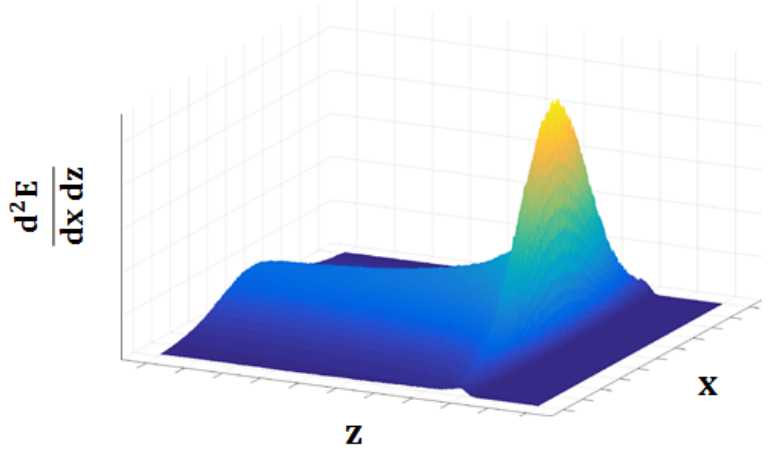

Figure 6.10: Mean energy loss of ions in water: Simulation of the differential distribution of the energy loss of a proton penetrating a water sample along the depth z and a virtual axis x perpendiucular to z. E.g., for a proton energy of 200 MeV, the mean absorption depth is 25.2 cm [142]. Simulation provided by Dr. Sebastian Lehrack, Lehrstuhl fuer medizinische Physik, LMU Muenchen.

$$S(E) = 0.307 \frac{Z}{A} \frac{1}{\beta^2} \left(\frac{1}{2} ln \frac{2 m_e c^2 \gamma^2 \beta^2 T_{max}}{I^2} - \beta^2 \right) \tag{6.2}$$

where m_e is the electron mass, T_{max} is the maximum transferable energy to a single electron, I the mean ionization potential of the given medium and A and Z its nuclear and atomic number, respectively. Moreover, β and γ are defined as kinematic terms via $\beta = \frac{v}{c}$ and $\gamma = \frac{1}{\sqrt{1-\beta^2}}$, respectively.

The statistic distribution of Coulomb interactions along the ion path through a the medium together with the statistical decrease in ion velocity v then reveals the well-known depth-dose curve, depicting the so called Bragg-peak that defines the depth (or relative position when looking at it in a 3D-volume) of the maximum dose and energy deposition right before the ions lose their kinetic energy and come to a rest. Figure 6.10 depicts a simulation of the corresponding Bragg curve and its characteristic energy loss over its pathway in z in analogy to Albul et al. [142].

The nature of the relatively well defined spatial volume of depth dose allows to utilize a particle beam to deposit energy inside a specific region of a given medium. Hence, the use of protons was suggested for tumor treatment in medical therapy already in the 1940s [143] and has been increasingly applied for actual medical therapy over the past decades [144]. However, the exact position of the depth dose depends on a number of parameters that are not easily determined, such as tissue density and varying proton energy. Furthermore,

tissue motion and patient movement as well as alterations in the patients morphology force the introduction of spatial safety margins during ion therapy, ultimately leading to a limitation of tumor tissue treated by the depth dose. The continuous monitoring of the dose deposition in a given ROI, preferably with simultaneous imaging and locating a given tumorous tissue, is therefore highly desireable in order to minimize such safety margins and maximize therapeutical outcome [141].
PET and gamma ray imaging are two methods that are currently being investigated for monitoring the position of the Bragg-peak during ion-therapy in tissue. However, both methods only deliver indirect information about the position of the Bragg-peak and require bulky, costly and complex instrumentation for detection [145]. Therefore, the measurement of the Bragg-peak by acoustic detection schemes, similar to methods employed in medical ultrasonography and optoacoustic imaging, could lead to a precise imaging tool for ion-therapy and has been suggested among others, by Assmann et al. with single element detection [146] and by Kellnberger et al. with tomographic detector arrays [147]. These approaches where based on piezoelectric ultrasound detectors and allowed the position of the Bragg-peak in sub-mm accuracy. However, the employed detectors showed a number of drawbacks during the experiments, such as high susceptibility towards EM noise as induced by the ion-beam and its high power magnetic steering coils as well as their bulky size. The latter has so far prevented the detection of the Bragg-peak from the same direction as the incident ion-beam, which limited its application to meaningful samples in analogy to the challenges of transmission-mode optoacoustic microscopy discussed in chapter 5 and chapter 4. Therefore, ionoacoustics could greatly benefit from an all-optical ultrasound detector that is immune to EM noise and exhibits an ultra-small footprint. Accordingly, the experiments discussed in this chapter were performed at the Lehrstuhl fuer medizinische Physik, LMU, where a proton-beam induced Bragg-peak was measured with the AsE sensor as introduced in subsection 6.2.2.

Experimental Setup and Bragg-Peak Imaging

The experimental setup and its functional principle is depicted in Figure 6.11a. Here, the setup can be divided into two parts:

1. Ion beam delivery and Bragg-peak generation.
2. Acoustic detection scheme with sensor alignment and AsE interrogation/read-out.

The generation of the ion beam was performed by the 12 MeV static tandem accelerator of the Maier-Leibnitz-Laboratory of the LMU and TU Munich, with proton energies of

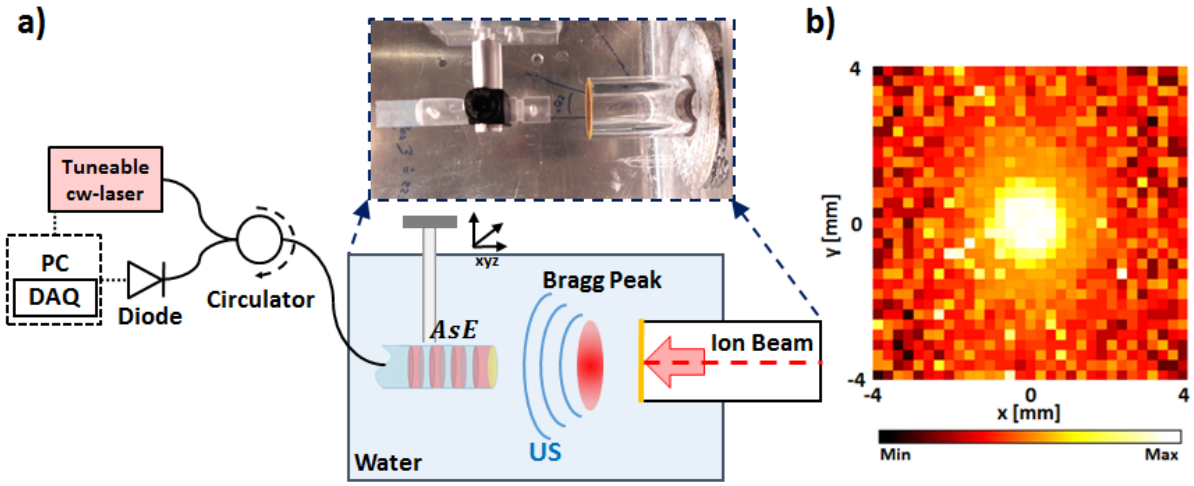

Figure 6.11: Experimental setup for 2D imaging of the Bragg-peak: (a) Schematic of the setup for raster scanning the AsE across a plane perpendicular to the proton beam. The ion beam is fed into the sample water tank via an air-filled tube. Inlet: photograph of the water tank with the ion-beam tube covered by a polyamid tape and the AsE installed in a protective plexiglass housing. (b) MIP of the scanned Bragg-peak corresponding to a disc-shaped dose deposition.

20 MeV ±10 keV. This energy corresponds to a mean deposition depth of 4 mm in water with a rather sharp Bragg-peak exhibiting a FWHM of 0.3 mm [147]. The proton pulse widths had a duration of around 10 ns and the beam chopping system served as trigger for data acquisition. The proton beam had a diameter of around 1 mm when exciting the vacuum tubes leading from the accelerator to the experimental setup. Before directed into a tank filled with deionized water, the beam had to pass a distance of around 8 cm in air and the coupling to the water was performed via a 50 μm polyamid (capton) window. A detailed description about the complete setup for proton delivery including possible repetition frequencies, accelerator currents as well as the hydrogen ion-source can be found e.g. in [146].

For the detection of acoustic signals, the AsE was installed inside a plexi-glass holder with the AsE tip in around 5 mm distance to the Bragg-peak. The holder allowed to position the AsE in the xy-direction perpendicular to the incident proton beam and to adjust its axial distance by the use of a μm resolution set of xyz-stages. Signal detection and AsE read-out were performed similar to the way described in subsection 6.4.1. The capability to image the 2D Bragg-disc was then demonstrated by recording MIPs as depicted in Figure 6.11b. Here, the AsE was scanned across a field of 8 mm x 8 mm with a step size of 0.25 mm. The recorded signals were averaged 500 times to increase SNR

and bandpass filtered between 500 kHz and 5 MHz in order to filter out noise induced by the magnet coils directing and focusing the proton beam. The FWHM of the Bragg-disc was determined to be around 2.4 mm by plotting through the center of the disc, which corresponded to the location of maximum dose deposition in the water sample.
While the AsE managed to image the Bragg-disc successfully, the relatively weak SNR became apparent. Note that in this framework the SNR was further reduced due to its primary frequency response at around 100 MHz which differs drastically from central frequency of the Bragg signal that was shown to be around 1.5 MHz [146]. Furthermore, the AsE functioned as an unfocused ultrasound detector and therefore did not allow to image with acoustic resolution. Instead, the resolution was determined by a convolution of the AsE diameter of around 125 μm, its opening angle of around 80 degrees as well as the NA of the acoustic signals originating in the Bragg-peak, which could be treated as individual acoustic point sources across the disc. Judging from the achieved resolution and comparing it to values in the literature where identical proton energies were examined, the resolution could be estimated to around 200 μm - 250 μm. However, once the AsE sensor is properly characterized for future experiments, a well defined sensor size or improved sensor design will allow for image reconstruction analogous to optoacoustic tomography for a point detector scanning atop a plane as discussed in chapter 2 and demonstrated by Kellnberger et al. [147]. Moreover, and contrary to piezoelectric ultrasound detectors, the optical nature of the AsE sensor allowed for continuous signal acquisition throughout the experiments, as the interrogation and read-out system was deployed in a distance of 50 m by the use of a protected SMF-28 optical fiber, outside the shielded ion-source installment and therefore well isolated from the EM noise induced e.g. by the magnetic beam coils.

6.5 Conclusion and Discussion

In this chapter, the AsE design was introduced as a novel optical ultrasound detector with a forward-looking point-like sensing geometry and a bandwidth of around 185 MHz. The AsE concept is advantageous compared to side-looking π-FBGs and could enable ultra-dense sensor arrays as well as the transfer of the optoacoustic modality towards challenging endoscopic applications. In particular, an AsE array has the potential to push the field of optoacoustic tomography, where spatial resolution depends on sensor bandwidth and the demonstrated central frequency response of around 100 MHz corresponds to spectra emitted by absorbers sized 10 μm and below. As derived in subsection 2.3.1, overall signal

acquisition time in tomography is proportional to the number of sensors employed and would also be greatly improved by dense sensor arrays. In the current fiber embodiment, 1D array densities of 7 detectors/mm are achievable, compared to e.g. 3 detectors/mm for piezoelectric arrays (Figure 3.6a) and around 13 detectors/mm for CMUT arrays (Figure 3.6b). As has been discussed in the literature [49, 50], lateral resolution is greatly blurred in tomographic imaging modalities by detector aperture and its acceptance angle. Consequently, the AsE design can help to push optoaocustic tomography towards spatial resolutions truly limited by sensor bandwidth.

A major insight was that the AsE footprint is not limited by the demonstrated fiber-based design but can be further miniaturized. In the demonstrator, the sensing area of the AsE facet correlated to the fiber core with a MFD of around 10 μm. Hence, the corresponding AsE sensor surface was around 27 times smaller than that of π-FBGs and around 4 times smaller than that of polymer micro-rings. Moreover, the reflection-mode sensor positioned at a fiber tip allowed for imaging in tight frameworks, not accessible by prevalent ultrasound detectors with comparable bandwidths. For an even reduced footprint, AsEs could be manufactured in optical fibers with reduced core diameters, which operate at reduced wavelengths or have tapered fiber cores [148]. Another incentive for moving away from standard waveguides with facets bigger than the actual sensing area is given by the presence of surface acoustic waves (**SAWs**). SAWs introduce a major challenge for silica or silicon based waveguides, as subsequent spectral shifts of the resonator can mask the time of incidence as well as introduce dominant spectral shifts exceeding the dynamic range of the sensor [145, 149]. On the other hand, a direct comparison between unfiltered B-scans of the π-FBG (Figure 4.3) and the AsE (Figure 6.5) revealed another advantage of the suggested design interrogated by a cw-laser, as the inherent intensity fluctuations at lower frequencies are negligible for the AsE. Cw-laser interrogation could enable AsE implementation at higher cost-efficiency compared to CPRI or PI methods [103].

While the demonstrated AsE can be seen as major advancement in the field of optical ultrasound sensing, there are a number of issues that remain to be tackled. The achieved sensitivity of around 50 Pa (NEP) is not sufficient yet to enable imaging of weak acoustic sources. As discussed in subsection 2.3.2, acoustic signals extend to the sub-Pa regime in optoacoustic microscopy. Moreover, a major mismatch between the acoustic impedances of water and the silica based fibers cause signal losses at the sensor surface. A workaround for this issue could be achieved by the implementation of acoustic matching layers or by the transition of the sensor design into e.g. polymer based waveguides with acoustic

impedances close to that of water [130]. Furthermore, AsE sensitivity could be enhanced by increasing the Q-factor of the resonator which in turn could be achieved by improving the reflectivity of either the grating or the reflection coating. Note that a mathematical analysis and simulation of the demonstrated AsE needs to be performed, before a statement about the AsE Q-factor can be deduced.

Eventually, the demonstrated AsE might pave the way towards novel imaging approaches: With lasers emitting intense and ultrashort light pulses as demonstrated in recent years [150], extended absorber surfaces may be illuminated, exciting planar acoustic wave fronts in analogy to acoustic point sources commonly excited in laser ultrasonics [38, 151]. With a given specimen introduced between the acoustic source and an AsE installed in parallel, shadowgraphy imaging could then be performed, resulting in a speed-of-sound map of the volume penetrated by the acoustic wave front. Corresponding initial experiments were performed by the CBI in collaboration with the Laboratory for Extreme Photonics of the LMU Muenchen.

7 Conclusion and outlook on all-optical ultrasound detectors

7.1 Conclusion

The work introduced in this thesis aimed at advancing optical ultrasound detectors and their translation into clinical optoacoustic imaging modalities. Therefore, the presented research included a broad review of prevalent methods for ultrasound detection as well as the implementation of Fabry-Pérot based sensors into optoacoustic imaging systems. The overall motivation to advance optical ultrasound detectors originated in initial experiments performed in intravascular [18] and gastrointestinal endoscopy [19], where the physical constraints of the employed piezoelectric ultrasound transducers became apparent. Further incentive was found when examining the current state of optoacoustic imaging as presented in chapter 3. Tomographic applications driven by piezoelectric and micro-machined ultrasound detectors have been optimised by close-to-ideal illumination and sensing geometries [152, 153], enabling label-free and *in vivo* imaging of model organisms [12, 15, 30, 39]. Here, in particular the research on handheld imaging devices, e.g. for imaging of subcutaneous micro-vasculature [154], is a steadily growing section in the field of optoacoustics [155]. Nevertheless, no major biological finding has been enabled by optoacoustic tomography yet. Optoacoustic microscopy has likewise demonstrated its capabilities in terms of penetration depth and complimentary contrast [40, 156, 157]. However, and despite advances in resolution and imaging speed [9,16], it is not yet closing in on clinical translation. The same applies for optoacoustic endoscopy, as this modality is still in its infancy, mainly due to challenges in micro-fabrication and related performance limitations of the applied detectors [158–160]. While approaches for intravascular imaging have been proposed, they have not yet been successfully demonstrated *in vivo*. Similarly, there is a broad interest for optoacoustic gastrointestinal endoscopy, but sophisticated sensor designs have not been demonstrated yet [19, 158].
In summary, optoacoustic imaging has advanced significantly over the past decade, but

progress in terms of image resolution and penetration depth have been slowing down recently. Moreover, practical aspects such as sensor footprint and sensing geometry limit the transition into challenging endoscopic modalities. By reviewing the landscape of existing optical ultrasound sensors [17], it was shown that optical detection of ultrasound may be a turning-point for the field of optoacoustic imaging.

Firstly, optical ultrasound detectors have been demonstrated to exceed the sensitivity, frequency/bandwidth and the footprint of prevalent piezoelectric and micro-manufactured ultrasound detectors.

Secondly, optical ultrasound detection may be performed in a myriad of embodiments, ranging from μm sized micro-rings [65] to large free-beam phase-sensitive sensing [54]. In contrast to e.g. piezoelectric sensors, this variety of detection geometries and physical concepts allows to select and adapt a suitable sensor for a given application.

Throughout this thesis work, emphasis was put onto the transition of optical ultrasound detection into imaging systems. In response, chapter 4 and chapter 5 therefore applied ultrasound sensors based on π-FBGs that are suitable for applications in optoacoustic microscopy and endoscopy. While such π-FBGs were demonstrated before by Rosenthal et al. [24, 62], they were applied for imaging of biological specimen for the first time in this thesis work. The first embodiment was discussed in chapter 4, where a transmission-mode optoacoustic microscope was introduced together with CRPI based sensor read-out, demonstrating the sensor capability for sensing weak optoacoustic signals originating in tissue [60]. The second embodiment was discussed in chapter 5, where a π-FBG based sensor-head allowed the creation of a novel multi-modal reflection-mode microscope [35]. This microscopy setup was capable of imaging samples of any thickness with the optoacoustic modality installed in parallel to existing microscopy modalities, such as standard fluorescence and multi-photon microscopy.

A novel ultrasound sensor design was demonstrated in chapter 6: the asymmetric etalon (AsE). In the implementation discussed in this thesis, the AsE constituted a fiber-based ultrasound sensor with a sensitivity (NEP) of around 50 Pa and a bandwidth of around 185 MHz at a central frequency of around 100 MHz. The AsE design was demonstrated in a GRIN-lens based optoacoustic endoscopy implementation as well as in ionoacoustics, where it imaged the Bragg-disc generated by a 20 MeV proton beam.

7.2 Outlook

Optoacoustic imaging has introduced major challenges onto prevalent ultrasound sensing technologies and has therefore fuelled interest in alternative sensing methods, such as micro-machined and optical ultrasound detectors. While it is commonly accepted in the optoacoustic imaging community that the transition to novel ultrasound sensors is inevitable, in particular piezoelectric sensors are still highly attractive and widespread. After all, this technology has undergone more than six decades of evolution, is economical in terms of production costs, can be read-out by relatively simple technological means and can be manufactured in advantageous designs, such as focused elements and sensor arrays.

Nevertheless, research on optical ultrasound detectors has already been surpassing the benchmarks set by piezoelectric sensors with the demonstration of e.g. sturdy plug & play FPs [100], π-FBGs capable of bulk production in the SOI platform [149] as well as parallelized sensors [97, 161]. Recently, FP interrogation has been demonstrated by a CRPI scheme with a wide spectral band of 80 nm [113]. Moreover, sensor sensitivity and bandwidth are constantly improved, such as in the case of single cell imaging based on laser ultrasonics [162] and optoacoustic microscopy utilizing imprinted polymer micro-rings [97]. By applying multiplexing approaches based e.g. on PI interrogation or frequency-division, FP based sensor arrays could be derived from the AsE sensors presented in this thesis and an implementation is depicted in Figure 7.1a. Here, the transition of the AsE principle into the SOI platform was performed at the TUM Chair for Biological Imaging (CBI), where sub-μm waveguides of around 400 nm to 500 nm in diameter were utilized for AsE manufacture. Following this approach, densely packed 2D arrays of AsE sensors could in future lead to CCD-like acoustic cameras constituting a valid replacement e.g. to present 2D hemispherical piezoelectric arrays [163] or flat virtual 2D arrays of optical FP detectors [164].

Regarding the clinical transition of optical sensors, an acoustically matched detector dedicated to optoacoustic microscopy is currently developed at the TUM CBI and is depicted in Figure 7.1b. Based on a novel method for Bragg grating inscription, cost-effective polymer based slabs could enable to manufacture impedance-matched specimen slides that contain π-FBG based ultrasound sensors and are optically transparent for other microscopy modalities. In the long run, cost-effective ultrasound transducers will go hand in hand with low-cost laser diodes and light-emitting diodes. Promising research on such illumination approaches has recently been shown to achieve ns-pulse durations

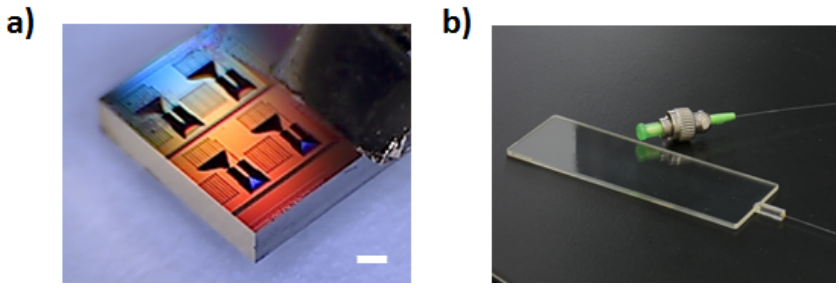

Figure 7.1: Outlook on optical ultrasound detection: (a) AsE sensors transferred to the SOI platform allow for dense arrays of point-like ultrasound detectors. Scale bar, 800 μm. (b) Polymer slabs with integrated and transparent ultrasound sensors allow for the substitution of standard microscopy slides.

as well as continuously and coded light modulation schemes, necessary for optoacoustic signal excitation [44, 165].

Eventually, a number of optoacoustic imaging approaches might be enabled by optical ultrasound detectors in future, which are inherently inaccessible for piezoelectric sensors. For example, beam-deflectometry enables the design of contact-free microscopy geometries [81] and advances in refractometric Schlieren-beam interrogation could lead to optoacoustic tomography without the need for computational image reconstruction [54].

However, major challenges remain for optical ultrasound detectors that seemingly go hand in hand with the fate of optoacoustic imaging. The latter has not achieved a breakthrough in the life sciences nor is it utilized in clinical applications yet, mainly due to a lack of sensitivity of current sensors, but also due to the challenging implementation of acoustic coupling and ultrasound detection into existing setups. Moreover, no implementable ultrasound detector has been demonstrated yet that combines sub-Pa sensitivity with a bandwidth of hundreds of MHz.

However, the research in the framework of this thesis showed that major technological advances addressing these challenges are foreseeable and will bring optical ultrasound detectors closer to the biomedical imaging community and thereby also boost optoacoustic imaging itself towards clinical translation.

8 Appendix

8.1 Exposure Limitations

8.1.1 Acoustic Pressure

According to the US Food and Drug Administration, the average intensity of an ultrasound pulse - as may be applied for pulse-echo ultrasonography - should be kept below $I = 190\frac{W}{cm^2}$ [166]. The corresponding maximum acoustic pressure amplitude p_{max} may then be calculated using the following equation [8]

$$p_{max} = \sqrt{\rho \nu I} \tag{8.1}$$

where ρ is the density of the medium and ν is the speed of sound in the medium. Estimating representative values of $\rho \approx 1000\frac{kg}{m^3}$ and $\nu \approx 1500\frac{m}{s}$, one obtains $p_{max} \approx 1.7\ MPa$.

8.1.2 Optical Fluence

According to the American National Standards Institute (ANSI), the local optical fluence (also referred to as radiant exposure) in the NIR must be kept below $U = 100\frac{mJ}{cm^2}$ [167]. During optoacoustic signal excitation, the corresponding acoustic pressure generated by a given laser pulse inside a given sample is provided by the equation [8]

$$p_{oa} = \Gamma \eta_{th} \mu_a U \tag{8.2}$$

where Γ is the Grüneisen coefficient, η_{th} the thermal efficiency and μ_a the optical absorption coefficient. At body temperature and assuming typical tissue parameters of $\Gamma \approx 0.2$, $\eta_{th} \approx 1$ and $\mu_a \approx 10cm^{-1}$ [43], one obtains $p_{oa} \approx 200\ kPa$.

8.2 Reflection-mode Pulsed Interferometry Interrogation

The $\pi-$FBG based ultrasound detectors for optoacoustic microscopy that were presented in chapter 4 and in chapter 5 were both interrogated and read out in transmission-mode. Yet, the interrogation setup can also be designed in a way as to allow reflection-mode read-out of the $\pi-$FBG, as illustrated in the simplified setup in Figure 8.1. Here, the PI or CRPI read-out as well as the demodulation of recorded acoustic signals is performed in the same manner as described in chapter 4. In contrast to transmission-mode read-out, the $\pi-$FBG is linked into the system via a 50/50 coupler. The reflection spectrum traversing back from the $\pi-$FBG can then be destructively interfered with the initial signal reflected back from a mirror installed in a second arm adjacent to the 50/50 coupler. The interference condition is preserved by a feedbacked piezoelectric fiber stretcher which is governed by the read-out of a photo-diode, coupled upstream of the demodulator by a 99/1 coupler (not depicted in Figure 8.1). The signal entering the downstream demodulator then comes with a notch shape corresponding to the spectral shape and FWHM in normal transmission-mode geometry.

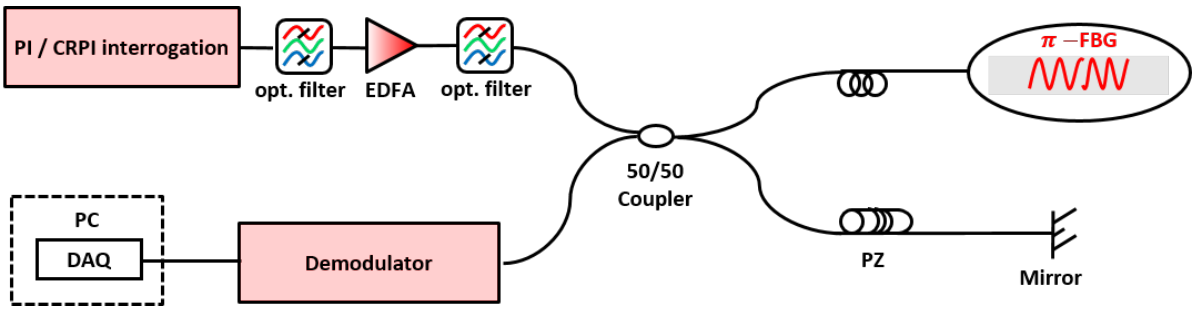

Figure 8.1: Reflection-mode CRPI read-out for a $\pi-$FBG.

A reflection-mode setup with a different form of applied CRF filter and tailored towards minimally invasive clincical imaging applications has been demonstrated in reference [24].

8.3 Epi-Illumination Optoacoustic Microscopy

8.3.1 Sensor-Head

The ability to deliver optoacoustic imaging as additional modality to existing microscopes and the approach to perform imaging in epi-illumination geometry was the key motivation

for the development of the sensor-head as demonstrated in chapter 5. Hence, the sensor-head was designed for easy use in existing off-the-shelf microscopes as underlined by Figure 8.2. Here, the sensor-head was installed into the sleeve and base-plate, atop the microscope objective placed into a revolving objective mount in an off-the-shelf microscope. This way, the sensor-head allowed for on-the-fly changes of objectives with e.g. higher NA and working distances.

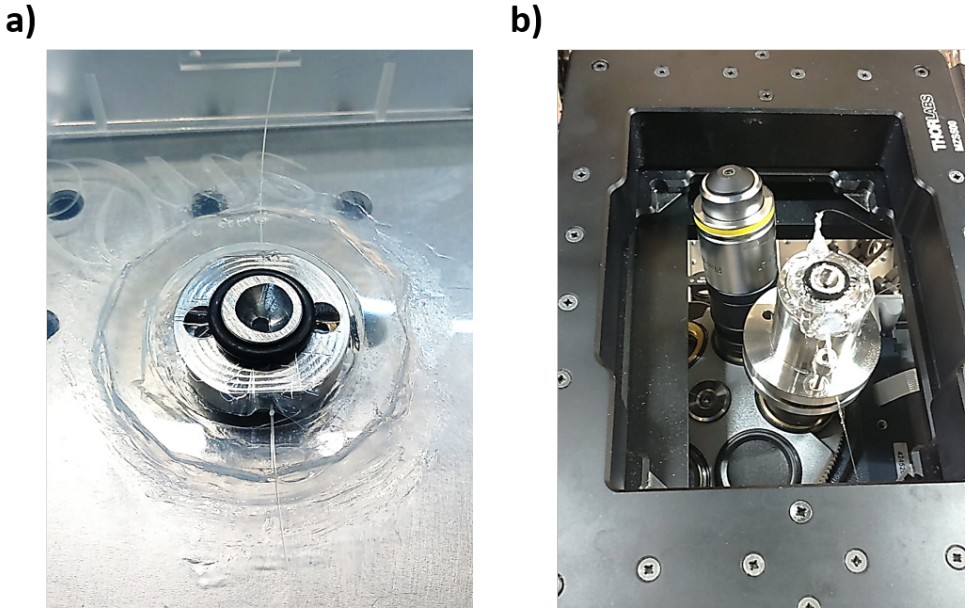

Figure 8.2: Installation of the $\pi-$FBG based sensor-head: (a) Sensor-head filled with de-ionized water and sealed with 10 μm PE-foil. (b) Sensor-head installed onto a standard revolving objective mount in an off-the-shelf microscope.

8.3.2 Silicon-on-Insulator Phantom

During initial phantom experiments and the characterization of the sensor-head as described in subsection 5.3.3, the facet of a SOI block (IMEC, Leuven, Belgium) was scanned. The image was taken via a scan of 100 x 100 pixels and a setup size of 0.63 μm. Interestingly, a symmetric pattern of regions with increased optoacoustic signal strength was observed throughout the facet and is depicted in Figure 8.3a.

The highlighted box in Figure 8.3b indicates the repetitive pattern element size of around 18.3 μm x 18.3 μm. A possible explanation of these patterns could be constructive interference of surface acoustic waves induced on the surface of the SOI block by optoacoustic excitation. It was discovered, that the pattern was more dominant at facets with

improved surface polish. Yet, a closer investigation is still necessary to reveal the pattern dependency e.g. on the amplitude of the induced acoustic waves, on the dimensions of the SOI facet as well as on the diameter of the optical excitation focus which might govern the frequency content of the induced acoustic waves.

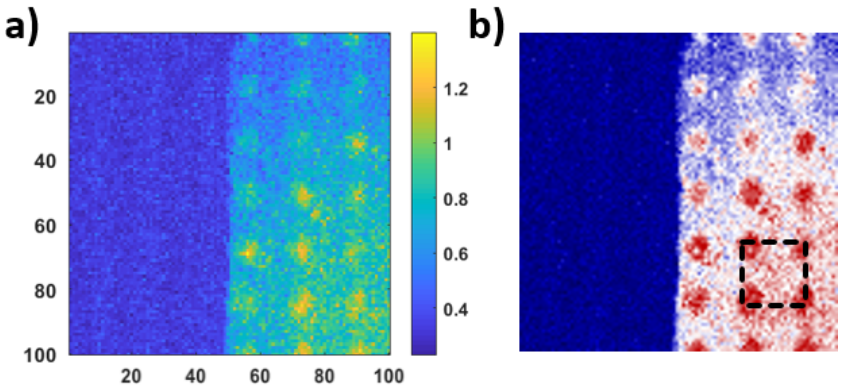

Figure 8.3: Intensity Pattern in Silicon-on-Insulator Phantom: (a) MIP of an optically-grade polished SOI block, indicating a pattern of increased acoustic signals detected on the facet. Image size, 63 μm. (b) Processed image of the SOI facet, with the approx. 18 μm side length of the fundamental square pattern indicated by a black box.

8.3.3 Wild-Type Mouse Model

Initial experiments with a wild-type mice ear on the setup as described in subsection 5.4.1 revealed dominant optical absorption by cutaneous pigment melanin rather than by the targeted haemoglobin in the vasculature and an exemplary result is depicted in Figure 8.4. The stitched image consists out of 6 x 5 individual MIPs, where stitching and image processing were performed similar to the experiments on nude mouse models, resulting in an overall image size of around 2 mm x 1.7 mm. The vertical lines in the image are dominant in the direction between outer rim and mouse head, indicating a flexed pinna atop the sensor-head with the outer parts of the individual epidermis section bulging out of the focal plane. Alternatively, these areas with low SNR might be caused by a slight bending of the PE-foil applied in the aperture of the sample holder.

In the course of the experiments presented in this thesis, it was not feasible to measure the degree of bulging - yet, an advanced setup might might implement thin polymer plates rather than stretchable PE foil, where bending is not an issue affecting the focal plane when imaging FOVs as small as 170 μm x 170 μm. Throughout the image, the dominant contrast reveals the melanin content in the epidermis layer and circular openings indicate

the position of hair follicles or of adjacent sebaceous glands. Exemplary hair-shafts leading into the corresponding hair follicles are indicated by white arrows in the image.

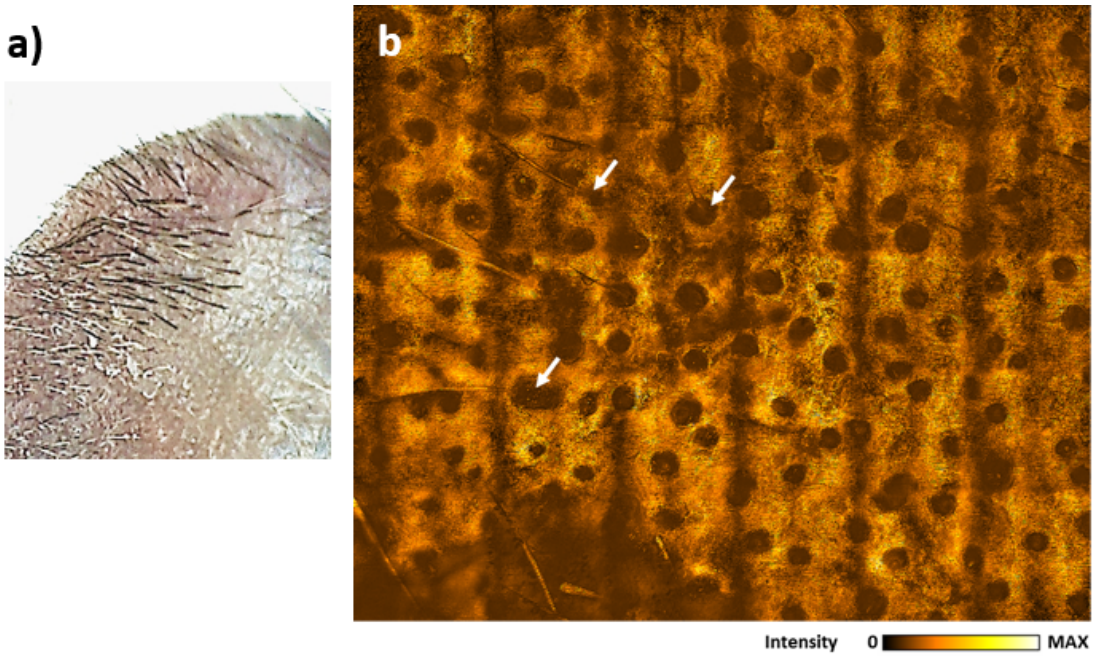

Figure 8.4: Optoacoustic microscopy of wild-type mouse ear: (a) Exemplary close-up photograph of a mouse ear with sparse hair-coat covering the outer pinna. (b) Optoacoustic microscopy image of mouse-ear pinna, dominated by melanin induced optical absorption contrast. White arrows indicate openings of hair follicles and adjacent sebaceous glands in the dermis. Image size, 2 mm x 1.7 mm.

Acknowledgments

How do you properly thank everybody involved in five years of fast paced and highly application driven research? The very research and the related projects that allowed me to meet numerous exciting people at excellent institutes through research visits, conferences and collaborations. The latter included institutions from near and far, such as the center for extreme photonics (LEX) in Garching, the center for non-destructive testing (NDT) in Linz as well as the cardiology department of the Massachusetts General Hospital (MGH) in Boston. It is safe to say that such a broad and multi-layered immersion into the field of sensors for biomedical and non-biomedical applications was a real find for me as well as a profitable and unique experience in every aspect.

Back to the question regarding an all-embracing acknowledgement - it is custom to give it a try nevertheless and I would like to particularly thank two persons:

Prof. Vasilis Ntziachristos, who supervised and supported my thesis and whose far sighted approach to both research and science enabled me to work application-oriented and on multiple interesting projects simultaneously. Moreover, he gave me the freedom to work independently and to develop own approaches and ideas. **Thank you Vasilis!**

Prof. Amir Rosenthal, who supervised my projects for the first two years (before becoming a professor at the Technion) and who (nevertheless) kept supporting me throughout experimental work and initial publications. In addition, he encouraged me to continue the development on optical detectors. **Thank you Amir!**

Furthermore, special thanks goes to Rami Shnaiderman for the countless days in the lab, for sharing and developing ideas together, for the discussions and the arguments, for the processing and the nerves, for the pushing and the pulling, for the introduction to the Democratic People's Republic of Korea (DPRK), for philosophizing on antimatter in Schwabing(er7) at 04:30 am as well as for everything else.

Next, I am of course much obliged to the CBI/IBMI wolf-pack: Yiyong Han, for the shared office time, for the introduction to tomographic reconstruction and the NERF theory. Johannes Rebling, for borrowing me equipment on a weekly basis, for fiber talks and the road-trip (great memories). Hailong He, for joint lab work on sensors and diodes

a long time ago as well as for good company in San Francisco not so long ago. Andriy Chmyrov, for the discussions about microscopy, the lunch breaks and the truck ride in the underground car park. Ludwig Prade for holding a mirror up to my face and also for not giving up on elaborating the depths of signal processing. See you in Glasgow! Paul Tommy Vetschera for the motivation, the dialect, the shared grantel-sessions as well as Vegas. See you in Cali! Christian Zakian for the MIB excursions, the mayhem and the philosophy. Sarah Glasl and Uwe Klemm for law and order in the labs, for making things possible and for not bearing a grudge against silver nitrate as well as on people who might have blown a lab up once. Or twice. Petri Heil! Dmitry Bozhko, for the Alexa Fluor, the Russian fish and the introduction to IBMI. Dominik Soliman, for the joint work on the optoacoustic microscope, for the finding of politicised DAQ cards and all the days in the lab - I will keep them in good mem0ry, too. Murad Omar, for managing IBMI's grapevine and for all the coffee. Walter Assmann, for giving me access to a 182 ton particle accelerator, just like that. Miguel Mapley Pleitez for joining the review paper as well as the discussions on Rotwild and Schlieren-detection schemes. Rodriguez Chapin, for mid-conversation brainteasers, polishing my English and politicising lunch breaks. Huang Yuanhui, for the Songshan Lake excursion, for believing in laser ultrasonics and for borrowing me half of his lab in parts - repeatedly. Say hi to Hong! Susanne Stern, for her problem solving skills, for 24/7 support in difficult situations and for all the chats. Babsi Schröder, for joint BMBF sparring, for grant writing support and for the wits. Thomas Gerlach and Josef Promoli, for never saying no whenever we wanted another device built (in microns!) and their expertise in hands-on mechanical engineering. And of course Ivan Olevir, for eventually solving the NERF issue.
Fortunately, the lack of strict formalities for acknowledgement chapters also allows me to consider family and friends: Oma, Caro, Isabel, Johann, Carola, Hias, Amy, Eier, Chris, Tom, Isy, Sebi, Linda, Andi, Manuel, Kitty, Aysel, Steffen, Kalli, Herb, Christian, Konsti, Danee, Maik und Maiki - people that continuously supplied me with food (food is love), evening schedules and who were always there.

Thank you.

Patents and Publications

Patent Submissions

1. **G. Wissmeyer**, R. Shnaiderman, and V. Ntziachristos. Sensor for tissue measurements. Patent application no. EP 18 16 0940.5, 2018.

2. V. Ntziachristos, **G. Wissmeyer**, and R. Shnaiderman. Sensor comprising a waveguide with optical resonator and sensing method. Patent application no. EP 18 16 0946.2, 2018.

First Author Publications

1. **G. Wissmeyer**, M. A. Pleitez, A. Rosenthal, and V. Ntziachristos, "Looking at sound: optoacoustics with all-optical ultrasound detection," *Light: Science and Applications*, vol. 7, no. 6, 2018.

2. R. Shnaiderman*, **G. Wissmeyer***, M. Seeger, D. Soliman, H. Estrada, D. Razansky, A. Rosenthal, and V. Ntziachristos, "Fiber interferometer for hybrid optical and optoacoustic intravital microscopy," *Optica*, vol. 4, no. 10, p. 1180, 2017.

3. **G. Wissmeyer**, D. Soliman, R. Shnaiderman, A. Rosenthal, and V. Ntziachristos, "All-optical optoacoustic microscope based on wideband pulse interferometry," *Optics Letters*, vol. 41, no. 9, pp. 1953-1956, 2016.

(* These authors contributed equally)

Second Author Publications

1. J. Rebling, H. Estrada, S. Gottschalk, G. Sela, M. Zwack, **G. Wissmeyer**, V. Ntziachristos, and D. Razansky, "Dual-wavelength hybrid optoacoustic-ultrasound biomicroscopy for functional imaging of large-scale cerebral vascular networks", *Journal of Biophotonics*. vol. 11, no. 9, pp. 1-7, 2018.

2. H. He, **G. Wissmeyer**, S. V. Ovsepian, A. Buehler, and V. Ntziachristos, "Optoacoustic endoscopy with optical and acoustic resolution," *Optics Letters*, vol. 41, no. 12, pp. 2708-2710, 2016.

3. D. Bozhko, E. A. Osborn, A. Rosenthal, J. W. Verjans, T. Hara, S. Kellnberger, **G. Wissmeyer**, S. V. Ovsepian, J. R. McCarthy, A. Mauskapf, A. F. Stein, F. A. Jaffer, and V. Ntziachristos, "Quantitative intravascular biological fluorescence-ultrasound imaging of coronary and peripheral arteries in vivo," *European Heart Journal - Cardiovascular Imaging*, vol. 18, no. 11, pp. 1253-1261, 2016.

4. I. A. Veres, P. Burgholzer, T. Berer, A. Rosenthal, **G. Wissmeyer**, and V. Ntziachristos, "Characterization of the spatio-temporal response of optical fiber sensors to incident spherical waves," *Journal of the Acoustical Society of America*, vol. 135, no. 1853, 2014.

Conference Proceedings

1. **G. Wissmeyer**, R. Shnaiderman, Q. Mustafa, D. Razansky, and V. Ntziachristos, "Pi-shifted Bragg grating in a silicon-on-insulator platform for optoacoustic imaging," in *Proccedings of SPIE*; submission accepted for 2019.

2. R. Shnaiderman, **G. Wissmeyer**, H. Estrada, D. Razansky, A. Chmyrov, Q. Mustafa, and V. Ntziachristos, "Ultrasound point detectors in the silicon photonics platform for high frequency optoacoustic tomography," in *Proccedings of SPIE*; submission accepted for 2019.

3. R. Shnaiderman, **G. Wissmeyer**, H. Estrada, M. Seeger, and V. Ntziachristos, "Intravital hybrid optical-optoacoustic microscopy based on fiber-Bragg interferometry," in *Proccedings of SPIE*, vol. 10494, p. 104942M, 2018.

4. **G. Wissmeyer***, R. Shnaiderman*, D. Soliman, and V. Ntziachristos, "Optoacoustic microscopy based on pi-FBG ultrasound sensors," in *Proccedings of SPIE*, vol. 10064, p. 1006423, 2017.

5. H. He, **G. Wissmeyer**, S. V. Ovsepian, A. Buehler, and V. Ntziachristos, "Optoacoustic endoscopy with optical and acoustic resolution," in *Proccedings of SPIE*, vol. 10064, p. 100641C, 2017.

(* These authors contributed equally)

Other

1. R. Shnaiderman*, **G. Wissmeyer***, H. Estrada, D. Razansky, A. Chmyrov, Q. Mustafa, and V. Ntziachristos, "Sub-micron silicon-on-insulator resonator for ultrasound detection," arXiv:1902.04115 [physics.app-ph], 2019.

2. **G. Wissmeyer**, S. Kefer, R. Shnaiderman, M. Rosenberger, R. Hellmann, and V. Ntziachristos, "Transparent Ultrasound Detector (TUD) enabling optoacoustic imaging in off-the-shelf microscopes," **in preparation**.

(* These authors contributed equally)

Reprint Permissions

Parts of the research presented in this work has been published in peer-reviewed journals throughout the duration of this thesis or is currently in the process of submission (see chapter on patents and publications). These elements were included as granted through the author rights in the copyright transfer agreements of the respective publishing journals. However, three external elements were included in this work to further improve relevant context and the respective reprint permissions are listed below.

Reprints

1. **Chapter 3, Figure 3.4:** Illustration taken from Akasheh et al. [73].
   Reprinted from **Sensors and Actuators**, vol. 52, no. 3, Firas Akasheh, Todd Myers, John D. Fraser, Susmita Bose, Amit Bandyopadhyay, Development of piezoelectric micromachined ultrasonic transducers, pp. 275 - 287, 2004, with permission from Elsevier. License no. 4372211504257.

2. **Chapter 3, Figure 3.6:** Photographs of commercial handheld piezoelectric and CMUT ultrasonography probes. Content and permission provided by Dr. Murad Omar, Helmholtz Zentrum Muenchen, via e-mail.

3. **Chapter 6, Figure 6.10:** Simulation of a 3D-Bragg-peak in water. Figure and permission provided by Dr. Sebastian Lehrack, Lehrstuhl fuer medizinische Physik, Ludwig-Maximilians-Universitaet Muenchen, via e-mail.

List of Figures

List of Tables

Bibliography

[1] N. B. Smith and A. Webb, *Introduction to Medical Imaging: Physics, Engineering and Clinical Applications*. Cambridge University Press, 2010.

[2] V. Ntziachristos, "Going deeper than microscopy: the optical imaging frontier in biology.," *Nature methods*, vol. 7, no. 8, pp. 603–614, 2010.

[3] K. Wang, N. G. Horton, K. Charan, and C. Xu, "Advanced fiber soliton sources for nonlinear deep tissue imaging in biophotonics," *IEEE Journal on Selected Topics in Quantum Electronics*, vol. 20, no. 2, 2014.

[4] P. Hoskins, *Diagnostic Ultrasound: Physics and Equipment*. Cambridge University Press, 2003.

[5] M. B. Zlatkin and J. V. Crues, *Clinical magnetic resonance imaging*. Philadelphia: Saunders, 1990.

[6] G. A. Cervantes, *Technical Fundamentals of Radiology and CT*. IOP Publishing, 2016.

[7] R. H. Webb, "Confocal optical microscopy," *Reports on progress in physics*, vol. 59, no. 3, pp. 427–471, 1996.

[8] L. V. Wang and H. Wu, *Biomedical Optics: Principles and Imaging*. John Wiley & Sons, 2012.

[9] L. V. Wang and L. Gao, "Photoacoustic microscopy and computed tomography: from bench to bedside," *Annual Review of Biomedical Engineering*, vol. 16, no. 7, pp. 155–185, 2014.

[10] D. Mauzerall, "Interactions between Light and Matter," pp. 215–237, 1972.

[11] M. Xu and L. V. Wang, "Photoacoustic imaging in biomedicine," *Review of Scientific Instruments*, vol. 77, no. 4, pp. 1–22, 2006.

[12] V. Ntziachristos, J. Ripoll, L. V. Wang, and R. Weissleder, "Looking and listening to light: The evolution of whole-body photonic imaging," *Nature Biotechnology*, vol. 23, no. 3, pp. 313–320, 2005.

[13] H. F. Zhang, K. Maslov, G. Stoica, and L. V. Wang, "Functional photoacoustic microscopy for high-resolution and noninvasive in vivo imaging.," *Nature biotechnology*, vol. 24, no. 7, pp. 848–851, 2006.

[14] L. Wang and S. Hu, "Photoacoustic Tomography: in Vivo Imaging Fro Organelles To Organs," *Science*, vol. 335, no. 6075, pp. 1458–1462, 2012.

[15] J. Xia, J. Yao, and L. V. Wang, "Photoacoustic tomography: principles and advances," *Progress In Electromagnetics Research*, vol. 4, no. 164, pp. 1–22, 2014.

[16] E. M. Strohm, M. J. Moore, and M. C. Kolios, "Single Cell Photoacoustic Microscopy: A Review," *IEEE Journal of Selected Topics in Quantum Electronics*, vol. 22, no. 3, pp. 1–15, 2016.

[17] G. Wissmeyer, M. A. Pleitez, A. Rosenthal, and V. Ntziachristos, "Looking at sound: optoacoustics with all-optical ultrasound detection," *Light: Science & Applications*, vol. 7, no. 6, 2018.

[18] D. Bozhko, E. A. Osborn, A. Rosenthal, J. W. Verjans, T. Hara, S. Kellnberger, G. Wissmeyer, S. V. Ovsepian, J. R. McCarthy, A. Mauskapf, A. F. Stein, F. A. Jaffer, and V. Ntziachristos, "Quantitative intravascular biological fluorescence-ultrasound imaging of coronary and peripheral arteries in vivo," *European Heart Journal – Cardiovascular Imaging*, vol. 18, no. 11, pp. 1253–1261, 2016.

[19] H. He, G. Wissmeyer, S. V. Ovsepian, A. Buehler, and V. Ntziachristos, "Optoacoustic endoscopy with optical and acoustic resolution," *Optics letters*, vol. 41, no. 12, pp. 2708–2710, 2016.

[20] D. Ochijewicz, M. Tomaniak, L. Koltowski, A. Rdzanek, A. Pietrasik, and J. Kochman, "Intravascular imaging of coronary artery disease: Recent progress and future directions," *Journal of Cardiovascular Medicine*, vol. 18, no. 10, pp. 733–741, 2017.

[21] P. G. Yock, D. T. Linker, B. A. Angelsen, and Tech, "Two-Dimensional Intravascular Ultrasound: Technical Development and Initial Clinical Experience," *Journal of the American Society of Echocardiography*, vol. 2, no. 4, pp. 296–304, 1989.

[22] G. J. Tearney, S. a. Boppart, B. E. Bouma, M. E. Brezinski, N. J. Weissman, J. F. Southern, and J. G. Fujimoto, "Scanning single-mode fiber optic catheter-endoscope for optical coherence tomography.," *Optics letters*, vol. 21, no. 7, pp. 543–545, 1996.

[23] X. Bai, X. Gong, W. Hau, R. Lin, J. Zheng, C. Liu, C. Zeng, X. Zou, H. Zheng, and L. Song, "Intravascular optical-resolution photoacoustic tomography with a 1.1 mm diameter catheter," *PLOS ONE*, vol. 9, no. 3, pp. 1–6, 2014.

[24] A. Rosenthal, S. Kellnberger, D. Bozhko, A. Chekkoury, M. Omar, D. Razansky, and V. Ntziachristos, "Sensitive interferometric detection of ultrasound for minimally invasive clinical imaging applications," *Laser Photonics Reviews*, vol. 8, no. 3, pp. 450–457, 2014.

[25] A. Hoffman, M. Goetz, M. Vieth, P. R. Galle, M. F. Neurath, and R. Kiesslich, "Confocal laser endomicroscopy: technical status and current indications," *Endoscopy*, vol. 38, no. 12, pp. 1275–1283, 2006.

[26] F. Helmchen, "Dynamic Confocal Imaging of Living Brain - Miniaturization of fluorescence microscopes using fibre optics," *Experimental Physiology*, vol. 87, no. 6, pp. 737–745, 2002.

[27] D. M. Soliman, *Augmented microscopy: Development and application of high-resolution optoacoustic and multimodal imaging techniques for label-free biological observation*. PhD thesis, Technical University of Munich, 2016.

[28] A. B. Bühler, *Multi-Spectral Optoacoustic Tomography: Methods and Applications*. PhD thesis, Technical University of Munich, 2014.

[29] L. Wang, *Photoacoustic Imaging and Spectroscopy*. CRC Press, 2009.

[30] L. V. Wang and S. Hu, "Photoacoustic Tomography: In Vivo Imaging from Organelles to Organs," *Science*, vol. 335, no. 6075, pp. 1458–1462, 2012.

[31] J. Yao and L. V. Wang, "Photoacoustic Microscopy," *Laser Photon Rev*, vol. 7, no. 5, pp. 1–36, 2012.

[32] S. Kellnberger, *Thermoacoustic Imaging in time and frequency domain. Theory and experiments*. PhD thesis, Technical University of Munich, 2012.

[33] C. Lutzweiler and D. Razansky, "Optoacoustic imaging and tomography: Reconstruction approaches and outstanding challenges in image performance and quantification," *Sensors (Switzerland)*, vol. 13, no. 6, pp. 7345–7384, 2013.

[34] S. J. Park, J. Eom, Y. H. Kim, C. S. Lee, and B. H. Lee, "Noncontact photoacoustic imaging based on all-fiber heterodyne interferometer," *Optics letters*, vol. 39, no. 16, pp. 4903–4906, 2014.

[35] R. Shnaiderman, G. Wissmeyer, M. Seeger, D. Soliman, H. Estrada, D. Razansky, A. Rosenthal, and V. Ntziachristos, "Fiber interferometer for hybrid optical and optoacoustic intravital microscopy," *Optica*, vol. 4, no. 10, p. 1180, 2017.

[36] A. G. Bell, "On the production and reproduction of sound by light.," *Am. J. Sci.*, vol. 20, no. 118, pp. 305–324, 1880.

[37] P. Beard, "Biomedical photoacoustic imaging," *Interface Focus*, vol. 1, no. 4, pp. 602–631, 2011.

[38] J. P. Monchalin, C. Néron, J. Bussière, P. Bouchard, C. Padioleau, R. Heon, M. Choquet, J. D. Aussel, G. Durou, and J. A. Nilson, "Laser-Ultrasonics: From the Laboratory to the Shop Floor," *Advanced Performance Materials*, vol. 5, pp. 7–23, 1998.

[39] L. V. Wang and J. Yao, "A practical guide to photoacoustic tomography in the life sciences," *Nature methods*, vol. 13, no. 8, pp. 627–638, 2016.

[40] P. Beard, "Biomedical photoacoustic imaging," *Interface Focus*, vol. 1, no. 4, pp. 602–631, 2011.

[41] D. Pan, B. Kim, L. V. Wang, and G. M. Lanza, "A Brief Account of Nanoparticle Contrast Agents for Photoacoustic Imaging," *Wiley Interdisciplinary Reviews: Nanomedicine and Nanobiotechnology*, vol. 5, no. 6, pp. 517–543, 2013.

[42] L. V. Wang and H.-i. Wu, *Biomedical optics*. John Wiley & Sons, 2007.

[43] J. V. Garcia, F. Zhang, and P. C. Ford, "Multi-photon excitation in uncaging the small molecule bioregulator nitric oxide," *Phil Trans R Soc A*, vol. 371, no. 1995, pp. 1–25, 2013.

[44] H. Zhong, T. Duan, H. Lan, M. Zhou, and F. Gao, "Review of Low-Cost Photoacoustic Sensing and Imaging Based on Laser Diode and Light-Emitting Diode," *Sensors*, vol. 18, no. 2264, 2018.

[45] C. Li and L. V. Wang, "Photoacoustic tomography and sensing in biomedicine," *Physics in Medicine and Biology*, vol. 54, no. 19, pp. 59–97, 2009.

[46] D. Soliman, G. J. Tserevelakis, M. Omar, and V. Ntziachristos, "Combining microscopy with mesoscopy using optical and optoacoustic label-free modes," *Scientific Reports*, vol. 5, no. 8, pp. 1–9, 2015.

[47] M. A. Áraque Caballero, *Incorporating Sensor Properties in Optoacoustic Imaging*. PhD thesis, Technical University of Munich, 2012.

[48] M. Xu and L. V. Wang, "Universal back-projection algorithm for photoacoustic computed tomography," *Physical Review E - Statistical, Nonlinear, and Soft Matter Physics*, vol. 71, no. 1, pp. 1–7, 2005.

[49] M. Xu, Y. Xu, and L. V. Wang, "Time-domain reconstruction algorithms and numerical simulations for thermoacoustic tomography in various geometries," *IEEE Transactions on Biomedical Engineering*, vol. 50, no. 9, pp. 1086–1099, 2003.

[50] M. Xu and L. V. Wang, "Analytic explanation of spatial resolution related to bandwidth and detector aperture size in thermoacoustic or photoacoustic reconstruction," *Physical Review E - Statistical Physics, Plasmas, Fluids, and Related Interdisciplinary Topics*, vol. 67, no. 5, p. 15, 2003.

[51] A. Rosenthal, D. Razansky, and V. Ntziachristos, "Fast semi-analytical model-based acoustic inversion for quantitative optoacoustic tomography," *IEEE Transactions on Medical Imaging*, vol. 29, no. 6, pp. 1275–1285, 2010.

[52] A. Rosenthal, V. Ntziachristos, and D. Razansky, "Acoustic Inversion in Optoacoustic Tomography: A Review," *Current Medical Imaging Reviews*, vol. 9, pp. 318–336, 2013.

[53] E. M. Strohm, E. S. L. Berndl, and M. C. Kolios, "High frequency label-free photoacoustic microscopy of single cells," *Photoacoustics*, vol. 1, no. 3-4, pp. 49–53, 2013.

[54] J. J. Niederhauser, M. Jaeger, and M. Frenz, "Real-time three-dimensional optoacoustic imaging using an acoustic lens system," *Applied Physics Letters*, vol. 85, no. 5, pp. 846–848, 2004.

[55] M. Moothanchery and M. Pramanik, "Performance characterization of a switchable acoustic resolution and optical resolution photoacoustic microscopy system," *Sensors (Switzerland)*, vol. 17, no. 2, 2017.

[56] C. Zhang, K. Maslov, S. Hu, R. Chen, Q. Zhou, K. Shung, and L. V. Wang, "Reflection-mode submicron-resolution in vivo photoacoustic microscopy," *Journal of Biomedical Optics*, vol. 17, no. 2, p. 020501, 2012.

[57] J. Yao and L. V. Wang, "Sensitivity of photoacoustic microscopy," *Photoacoustics*, vol. 2, no. 2, pp. 87–101, 2014.

[58] X. L. Deán-Ben, D. Razansky, and V. Ntziachristos, "The effects of acoustic attenuation in optoacoustic signals.," *Physics in medicine and biology*, vol. 56, no. 18, pp. 6129–48, 2011.

[59] F. L. Pedrotti, L. M. Pedrotti, and L. S. Pedrotti, *Introduction to Optics*. Pearson Education Limited, 3 ed., 2014.

[60] G. Wissmeyer, D. Soliman, R. Shnaiderman, A. Rosenthal, and V. Ntziachristos, "All-optical optoacoustic microscope based on wideband pulse interferometry," *Optics Letters*, vol. 41, no. 9, pp. 1953–1956, 2016.

[61] E. Z. Zhang and P. C. Beard, "A miniature all-optical photoacoustic imaging probe," *Proceedings of SPIE*, vol. 7899, pp. 78991F–1– 78991F–6, 2011.

[62] A. Rosenthal, D. Razansky, and V. Ntziachristos, "High-sensitivity compact ultrasonic detector based on a pi-phase-shifted fiber Bragg grating.," *Optics letters*, vol. 36, no. 10, pp. 1833–1835, 2011.

[63] S. J. Mathews, C. Little, C. D. Loder, R. D. Rakhit, W. Xia, E. Z. Zhang, P. C. Beard, M. C. Finlay, and A. E. Desjardins, "All-optical dual photoacoustic and optical coherence tomography intravascular probe," *Photoacoustics*, vol. 11, no. June, pp. 65–70, 2018.

[64] A. M. Winkler, K. Maslov, and L. V. Wang, "Noise-equivalent sensitivity of photoacoustics.," *Journal of biomedical optics*, vol. 18, no. 9, p. 97003, 2013.

[65] H. Li, B. Dong, Z. Zhang, H. F. Zhang, and C. Sun, "A transparent broadband ultrasonic detector based on an optical micro-ring resonator for photoacoustic microscopy.," *Scientific reports*, vol. 4, p. 4496, 2014.

[66] J. F. Tressler, S. Alkoy, and R. E. Newnham, "Piezoelectric sensors and sensor material," *Journal of Electroceramics*, vol. 2, no. 4, pp. 257–272, 1998.

[67] A. A. Vives, ed., *Piezoelectric Transducers and Applications*. Berlin, Heidelberg: Springer Berlin Heidelberg, 2008.

[68] G. Brodie, Y. Qiu, S. Cochran, G. Spalding, and M. MacDonald, "Optically transparent piezoelectric transducer for ultrasonic particle manipulation," *IEEE Transactions on Ultrasonics, Ferroelectrics, and Frequency Control*, vol. 61, no. 3, pp. 389–391, 2014.

[69] Y. Qiu, J. V. Gigliotti, M. Wallace, F. Griggio, C. E. Demore, S. Cochran, and S. Trolier-McKinstry, "Piezoelectric micromachined ultrasound transducer (PMUT) arrays for integrated sensing, actuation and imaging," *Sensors (Switzerland)*, vol. 15, no. 4, pp. 8020–8041, 2015.

[70] P. Muralt, N. Ledermann, J. Baborowski, A. Barzegar, S. Gentil, B. Belgacem, S. Petitgrand, A. Bosseboeuf, and N. Setter, "Piezoelectric micromachined ultrasonic transducers based on PZT thin films," *IEEE Transactions on Ultrasonics, Ferroelectrics, and Frequency Control*, vol. 52, no. 12, pp. 2276–2288, 2005.

[71] S. Trolier-McKinstry and P. Muralt, "Thin film piezoelectrics for MEMS," *Journal of Electroceramics*, vol. 12, pp. 7–17, 2004.

[72] I. O. Wygant, X. Zhuang, D. T. Yeh, Ö. Oralkan, A. S. Ergun, M. Karaman, and B. T. Khuri-Yakub, "Integration of 2D CMUT arrays with front-end electronics for volumetric ultrasound imaging," *IEEE Transactions on Ultrasonics, Ferroelectrics, and Frequency Control*, vol. 55, no. 2, pp. 327–341, 2008.

[73] F. Akasheh, T. Myers, J. D. Fraser, S. Bose, and A. Bandyopadhyay, "Development of piezoelectric micromachined ultrasonic transducers," *Sensors and Actuators, A: Physical*, vol. 52, no. 3, pp. 275–287, 2004.

[74] Q. Zhou, S. Lau, D. Wu, and K. K. Shung, "Piezoelectric films for high frequency ultrasonic transducers in biomedical applications," *Prog Mater Science*, vol. 56, no. 2, pp. 139–174, 2011.

[75] D. E. Dausch, K. H. Gilchrist, J. B. Carlson, S. D. Hall, J. B. Castellucci, and O. T. V. Ramm, "In Vivo Real-Time 3-D Intracardiac," *IEEE Trans. Ultrason., Ferroelectron., Freq. Contr.*, vol. 61, no. 10, pp. 1754–1765, 2014.

[76] W. Xia, D. Piras, J. C. G. van Hespen, S. van Veldhoven, C. Prins, T. G. van Leeuwen, W. Steenbergen, and S. Manohar, "An optimized ultrasound detector for photoacoustic breast tomography," *Medical physics*, vol. 40, no. 3, p. 032901, 2013.

[77] B. T. Khuri-Yakub and Ö. Oralkan, "Capacitive micromachined ultrasonic transducers for medical imaging and therapy," *Journal of Micromechanics and Microengineering*, vol. 21, no. 5, p. 054004, 2011.

[78] J. Rebling, O. Warshavski, C. Meynier, and D. Razansky, "Optoacoustic characterization of broadband directivity patterns of capacitive micromachined ultrasonic transducers," *Journal of Biomedical Optics*, vol. 22, no. 4, p. 041005, 2016.

[79] X. Zhu, Z. Huang, G. Wang, W. Li, D. Zou, and C. Li, "Ultrasonic detection based on polarization-dependent optical reflection," *Opt. Lett.*, vol. 42, no. 3, pp. 439–441, 2017.

[80] J. E. Parsons, C. a. Cain, and J. B. Fowlkes, "Cost-effective assembly of a basic fiber-optic hydrophone for measurement of high-amplitude therapeutic ultrasound fields.," *The Journal of the Acoustical Society of America*, vol. 119, no. 3, pp. 1432–1440, 2006.

[81] S. M. Maswadi, B. L. Ibey, C. C. Roth, D. A. Tsyboulski, H. T. Beier, R. D. Glickman, and A. A. Oraevsky, "All-optical optoacoustic microscopy based on probe beam deflection technique," *Photoacoustics*, vol. 4, no. 3, pp. 91–101, 2016.

[82] R. A. Barnes, S. Maswadi, R. Glickman, and M. Shadaram, "Probe beam deflection technique as acoustic emission directionality sensor with photoacoustic emission source," *Applied optics*, vol. 53, no. 3, pp. 511–519, 2014.

[83] N. Kudo, "Optical methods for visualization of ultrasound fields," *Japanese Journal of Applied Physics*, vol. 54, no. 7, p. 07HA01, 2015.

[84] R. Nuster, P. Slezak, and G. Paltauf, "High resolution three-dimensional photoacoutic tomography with CCD-camera based ultrasound detection," *Biomedical Optics Express*, vol. 5, no. 8, p. 2635, 2014.

[85] C. I. Zanelli and S. M. Howard, "Schlieren metrology for high frequency medical ultrasound," *Ultrasonics*, vol. 44, pp. 105–107, 2006.

[86] H. A. Deferrari and F. A. Andrews, "Technique for Measuring Small-Order Vibration Displacements," *J. Acoust. Soc. Am.*, vol. 39, p. 979, 1966.

[87] H. A. Deferrari, "Vibrational Displacement and Mode-Shape Measurement by a Laser Interferometer," *The Journal of the Acoustical Society of America*, vol. 42, no. 5, p. 982, 1967.

[88] J. A. Bucaro, "Fiber-optic hydrophone," *The Journal of the Acoustical Society of America*, vol. 62, no. 5, p. 1302, 1977.

[89] J. K. Thomson, H. K. Wickramasinghe, and E. A. Ash, "A Fabry-Perot acoustic surface vibration detector - application to acoustic holography," *Journal of Physics D: Applied Physics*, vol. 6, no. 6, pp. 677–687, 1973.

[90] R. J. Dewhurst and Q. Shan, "Optical remote measurement of ultrasound," *Measurement Science and Technology*, vol. 10, no. 11, pp. R139–R168, 1999.

[91] G. Paltauf, R. Nuster, M. Haltmeier, and P. Burgholzer, "Photoacoustic tomography using a Mach-Zehnder interferometer as an acoustic line detector," *Applied Optics*, vol. 46, no. 16, pp. 3352–3358, 2007.

[92] T. Berer, A. Hochreiner, S. Zamiri, and P. Burgholzer, "Remote photoacoustic imaging on solid material using a two-wave mixing interferometer.," *Optics letters*, vol. 35, no. 24, pp. 4151–4153, 2010.

[93] J. D. Hamilton and M. O. Donnell, "High frequency ultrasound imaging with optical arrays," *IEEE Transactions on Ultrasonics, Ferroelectrics, and Frequency Control*, vol. 45, no. 1, pp. 216–235, 1998.

[94] N. Hodgson and H. Weber, *Optical Resonators*. Springer-Verlag Berlin Heidelberg New York, 1997.

[95] P. Morris, A. Hurrell, A. Shaw, E. Zhang, and P. Beard, "A Fabry-Perot fiber-optic ultrasonic hydrophone for the simultaneous measurement of temperature and acoustic pressure.," *The Journal of the Acoustical Society of America*, vol. 125, no. 6, pp. 3611–3622, 2009.

[96] E. Zhang, J. Laufer, and P. Beard, "Backward-mode multiwavelength photoacoustic scanner using a planar Fabry Perot polymer film ultrasound sensor for high resolution three-dimensional imaging of biological tissues," *Applied Optics*, vol. 47, no. 4, pp. 561–577, 2008.

[97] C. Zhang, S. L. Chen, T. Ling, and L. J. Guo, "Review of imprinted polymer microrings as ultrasound detectors: Design, fabrication, and characterization," *IEEE Sensors Journal*, vol. 15, no. 6, pp. 3241–3248, 2015.

[98] A. Maxwell, S.-W. Huang, T. Ling, J.-S. Kim, S. Ashkenazi, and L. Jay Guo, "Polymer Microring Resonators for High-Frequency Ultrasound Detection and Imaging," *IEEE Journal of Selected Topics in Quantum Electronics*, vol. 14, no. 1, pp. 191–197, 2008.

[99] W. Rohringer, S. Preißer, M. Liu, S. Zotter, Z. Chen, B. Hermann, H. Sattmann, B. Fischer, and W. Drexler, "All-optical highly sensitive broadband ultrasound sensor without any deformable parts for photoacoustic imaging," *Proc. of SPIE*, vol. 9708, pp. 151–158, 2016.

[100] S. Preisser, W. Rohringer, M. Liu, C. Kollmann, S. Zotter, B. Fischer, and W. Drexler, "All-optical highly sensitive akinetic sensor for ultrasound detection and photoacoustic imaging," *Biomedical optics express*, vol. 7, no. 10, pp. 9027–9034, 2016.

[101] G. Rousseau, A. Blouin, and J.-P. Monchalin, "Non-contact photoacoustic tomography and ultrasonography for tissue imaging.," *Biomedical optics express*, vol. 3, no. 1, pp. 16–25, 2012.

[102] J. P. Monchalin, "Optical detection of ultrasound at a distance using a confocal Fabry-Perot interferometer," *Applied Physics Letters*, vol. 47, no. 1, pp. 14–16, 1985.

[103] A. Rosenthal, D. Razansky, and V. Ntziachristos, "Wideband optical sensing using pulse interferometry.," *Optics express*, vol. 20, no. 17, pp. 19016–29, 2012.

[104] A. Rosenthal, S. Kellnberger, G. Sergiadis, and V. Ntziachristos, "Wideband fiber-interferometer stabilization with variable phase," *IEEE Photonics Technology Letters*, vol. 24, no. 17, pp. 1499–1501, 2012.

[105] A. Hochreiner, J. Bauer-Marschallinger, P. Burgholzer, B. Jakoby, and T. Berer, "Non-contact photoacoustic imaging using a fiber based interferometer with optical amplification.," *Biomedical optics express*, vol. 4, no. 11, pp. 2322–31, 2013.

[106] H. Gabai, I. Steinberg, and A. Eyal, "Multiplexing of fiber-optic ultrasound sensors via swept frequency interferometry.," *Optics express*, vol. 23, no. 15, pp. 18915–24, 2015.

[107] A. D. Kersey, M. A. Davis, H. J. Patrick, M. LeBlanc, K. P. Koo, C. G. Askins, M. A. Putnam, and E. J. Friebele, "Fiber grating sensors," *Lightwave Technology, Journal of*, vol. 15, no. 8, pp. 1442–1463, 1997.

[108] B. Moslehi, "Noise Power Spectra," *Journal of lightwave technology*, vol. 4, no. 11, pp. 1704–1710, 1986.

[109] J. H. Chow, I. C. Littler, D. E. McClelland, and M. B. Gray, "Laser frequency-noise-limited ultrahigh resolution remote fiber sensing," *Optics express*, vol. 14, no. 11, pp. 4617–4624, 2006.

[110] J. Yao and L. V. Wang, "Sensitivity of photoacoustic microscopy," *Photoacoustics*, vol. 2, no. 2, pp. 87–101, 2014.

[111] G. Wissmeyer, R. Shnaiderman, D. Soliman, and V. Ntziachristos, "Optoacoustic microscopy based on pi-FBG ultrasound sensors," in *Proceedings of SPIE*, vol. 10064, pp. 1006423–1 – 1006423–7, 2017.

[112] T. Erdogan, "Fiber grating spectra," *Journal of Lightwave Technology*, vol. 15, no. 8, pp. 1277–1294, 1997.

[113] O. Volodarsky, Y. Hazan, and A. Rosenthal, "Ultrasound detection via low-noise pulse interferometry using a free-space Fabry-Pérot," *Optics Express*, vol. 26, no. 17, p. 22405, 2018.

[114] I. A. Veres, P. Burgholzer, T. Berer, A. Rosenthal, G. Wissmeyer, and V. Ntziachristos, "Characterization of the spatio-temporal response of optical fiber sensors to incident spherical waves," *The Journal of the Acoustical Society of America*, vol. 135, no. 4, pp. 1853–1862, 2014.

[115] A. Krumholz, L. Wang, J. Yao, and L. V. Wang, "Functional photoacoustic microscopy of diabetic vasculature.," *Journal of biomedical optics*, vol. 17, no. 6, p. 060502, 2012.

[116] F. S. Foster, C. J. Pavlin, K. A. Harasiewicz, D. A. Christopher, and D. H. Turnbull, "Advances in ultrasound biomicroscopy," *Ultrasound in Med. & Biol.*, vol. 26, no. 1, pp. 1–27, 2000.

[117] V. P. Efremov, M. F. Ivanov, A. D. Kiverin, and I. S. Yakovenko, "Shock-wave processes evolution in fused quartz under intense energy action," *Journal of Physics: Conference Series*, vol. 774, no. 1, 2016.

[118] G. J. Tserevelakis, D. Soliman, M. Omar, and V. Ntziachristos, "Hybrid multiphoton and optoacoustic microscope.," *Optics letters*, vol. 39, no. 7, pp. 1819–1822, 2014.

[119] M. Seeger, A. Karlas, D. Soliman, J. Pelisek, and V. Ntziachristos, "Multimodal optoacoustic and multiphoton microscopy of human carotid atheroma," *Photoacoustics*, vol. 4, no. 3, pp. 102–111, 2016.

[120] S. Hu, K. Maslov, and L. V. Wang, "In vivo functional chronic imaging of a small animal model using optical-resolution photoacoustic microscopy," *Medical Physics*, vol. 36, no. 6, pp. 2320–2323, 2009.

[121] B. Dong, L. Hao, Z. Zhang, K. Zhang, S. Chen, C. Sun, and H. F. Zhang, "Isometric multimodal photoacoustic microscopy based on optically transparent micro-ring ultrasonic detection," *Optica*, vol. 2, no. 2, pp. 169–176, 2015.

[122] R. Shnaiderman, G. Wissmeyer, H. Estrada, M. Seeger, and V. Ntziachristos, "Intravital hybrid optical-optoacoustic microscopy based on fiber-Bragg interferometry," in *Photons Plus Ultrasound: Imaging and Sensing 2018* (A. A. Oraevsky and L. V. Wang, eds.), p. 92, SPIE, 2018.

[123] E. Z. Zhang, J. G. Laufer, R. B. Pedley, and P. C. Beard, "In vivo high-resolution 3D photoacoustic imaging of superficial vascular anatomy.," *Physics in Medicine and Biology*, vol. 54, no. 4, pp. 1035–1046, 2009.

[124] T. Kundu, *Ultrasonic Nondestructive Evaluation: Engineering and Biological Material Characterization*. CRC Press, 2004.

[125] R. G. Maev, *Acoustic Microscopy: Fundamentals and Applications*. Wiley-VCH Verlag, 2008.

[126] J. D. N. Cheeke, *Fundamentals and applications of ultrasonic waves*. CRC Press, 2002.

[127] S. Preibisch, S. Saalfeld, and P. Tomancak, "Globally optimal stitching of tiled 3D microscopic image acquisitions," *Bioinformatics*, vol. 25, no. 11, pp. 1463–1465, 2009.

[128] Z. Xie, S.-L. Chen, T. Ling, L. J. Guo, P. L. Carson, and X. Wang, "Pure optical photoacoustic microscopy," *Optics express*, vol. 19, no. 10, pp. 9027–9034, 2011.

[129] M. Kietzmann, D. Lubach, and H.-J. Heeren, "The mouse epidermis as a model in skin pharmacology: Influence of age and sex on epidermal metabolic reactions and their circadian rhythms," *Laboratory Animals*, vol. 24, no. 4, pp. 321–327, 1990.

[130] H. Grün, T. Berer, K. Pühringer, R. Nuster, G. Paltauf, and P. Burgholzer, "Polymer fiber detectors for photoacoustic imaging," *Proc. SPIE*, vol. 7564, p. 75640M, 2010.

[131] M. Rosenberger, G. Koller, S. Belle, B. Schmauss, and R. Hellmann, "Planar Bragg grating in bulk Polymethylmethacrylate," *Optics Express*, vol. 20, no. 25, p. 27288, 2012.

[132] M. Rosenberger, S. Kefer, M. Girschikofsky, G.-L. Roth, S. Hessler, S. Belle, B. Schmauss, and R. Hellmann, "High-temperature stable and sterilizable waveguide Bragg grating in planar cyclo-olefin copolymer," *Optics letters*, vol. 43, no. 14, pp. 3321–3324, 2018.

[133] T. Liu and M. Han, "Analysis of π-phase-shifted fiber Bragg gratings for ultrasonic detection," *IEEE Sensors Journal*, vol. 12, no. 7, pp. 2368–2373, 2012.

[134] S. Laurent and P. Boutouyrie, "Large and Small Artery Alterations," *Circ Res*, vol. 116, no. 6, pp. 1007–1022, 2015.

[135] M. T. Schram, S. J. Sep, C. J. Van Der Kallen, P. C. Dagnelie, A. Koster, N. Schaper, R. M. Henry, and C. D. Stehouwer, "The Maastricht Study: An extensive phenotyping study on determinants of type 2 diabetes, its complications and its comorbidities," *European Journal of Epidemiology*, vol. 29, no. 6, pp. 439–451, 2014.

[136] M. Omar, M. Schwarz, D. Soliman, P. Symvoulidis, and V. Ntziachristos, "Pushing the optical imaging limits of cancer with multi-frequency-band raster-scan optoacoustic mesoscopy (RSOM).," *Neoplasia*, vol. 17, no. 2, pp. 208–214, 2015.

[137] P. Beard, "Optical detection system for biomedical photoacoustic imaging," *Proceedings of SPIE*, vol. 3916, no. 1, pp. 34–42, 2001.

[138] F. Trepanier, G. Brochu, M. Morin, and A. Mailloux, "High-End FBG Design and Manufacturing for Industrial Lasers, Sensing and Telecommunications," in *Advanced Photonics*, (Washington, D.C.), p. BM4D.1, OSA, 2014.

[139] F. a. Jaffer, M. a. Calfon, A. Rosenthal, G. Mallas, R. N. Razansky, A. Mauskapf, R. Weissleder, P. Libby, and V. Ntziachristos, "Two-dimensional intravascular near-infrared fluorescence molecular imaging of inflammation in atherosclerosis and stent-induced vascular injury," *Journal of the American College of Cardiology*, vol. 57, no. 25, pp. 2516–2526, 2011.

[140] A. Kamaya, S. Vaithilingam, B. I. Chung, O. Oralkan, and B. T. Khuri-Yakub, "Photoacoustic imaging of the bladder: A pilot study," *Journal of Ultrasound in Medicine*, vol. 32, no. 7, pp. 1245–1250, 2013.

[141] A. C. Knopf and A. Lomax, "In vivo proton range verification: A review," *Physics in Medicine and Biology*, vol. 58, no. 15, pp. 131–160, 2013.

[142] V. I. Albul, V. B. Bychkov, S. S. Vasil, K. E. Gusev, V. S. Demidov, E. V. Demidova, N. K. Krasnov, and A. F. Kurchanov, "Acoustic field generated by a beam of protons stopping in a water medium," *Acoustical Physics*, vol. 51, no. 1, pp. 33–37, 2005.

[143] R. R. Wilson, "Radiological Use of Fast Protons," *Radiology*, vol. 47, no. 5, pp. 487–491, 1946.

[144] D. Schardt, T. Elsässer, and D. Schulz-Ertner, "Heavy-ion tumor therapy: Physical and radiobiological benefits," *Reviews of Modern Physics*, vol. 82, no. 1, pp. 383–425, 2010.

[145] S. Kellnberger, A. Rosenthal, A. Myklatun, G. G. Westmeyer, G. Sergiadis, and V. Ntziachristos, "Magnetoacoustic Sensing of Magnetic Nanoparticles," *Physical Review Letters*, vol. 116, no. 10, p. 108103, 2016.

[146] W. Assmann, S. Kellnberger, S. Reinhardt, S. Lehrack, A. Edlich, P. G. Thirolf, M. Moser, G. Dollinger, M. Omar, V. Ntziachristos, and K. Parodi, "Ionoacoustic characterization of the proton Bragg peak with submillimeter accuracy," *Medical Physics*, vol. 42, no. 2, pp. 567–574, 2015.

[147] S. Kellnberger, W. Assmann, S. Lehrack, S. Reinhardt, P. Thirolf, D. Queirós, G. Sergiadis, G. Dollinger, K. Parodi, and V. Ntziachristos, "Ionoacoustic tomography of the proton Bragg peak in combination with ultrasound and optoacoustic imaging," *Scientific Reports*, vol. 6, no. 6, pp. 1–7, 2016.

[148] V. I. Kopp, J. Park, M. Wlodawski, J. Singer, D. Neugroschl, and A. Z. Genack, "Pitch Reducing Optical Fiber Array and multicore fiber for space-division multiplexing," in *2013 IEEE Photonics Society Summer Topical Meeting Series*, vol. 2, pp. 99–100, IEEE, 2013.

[149] A. Rosenthal, M. Omar, H. Estrada, S. Kellnberger, D. Razansky, and V. Ntziachristos, "Embedded ultrasound sensor in a silicon-on-insulator photonic platform," *Applied Physics Letters*, vol. 104, no. 2, p. 021116, 2014.

[150] A. Baltuška, T. Udem, M. Uiberacker, M. Hentschel, E. Goulielmakis, C. Gohle, R. Holzwarth, V. S. Yakovlev, A. Scrinzi, T. W. Hänsch, and F. Krausz, "Attosecond control of electronic processes by intense light fields," *Nature*, vol. 421, no. 6923, pp. 611–615, 2003.

[151] C. Scruby and L. Drain, *Laser Ultrasonics Techniques and Applications*. CRC Press, 1990.

[152] Y. Han, V. Ntziachristos, and A. Rosenthal, "Optoacoustic image reconstruction and system analysis for finite-aperture detectors under the wavelet-packet framework," *Journal of Biomedical Optics*, vol. 21, no. 1, p. 016002, 2016.

[153] V. Ntziachristos and D. Razansky, "Molecular imaging by means of multispectral optoacoustic tomography (MSOT)," *Chemical Reviews*, vol. 110, no. 5, pp. 2783–2794, 2010.

[154] J. Aguirre, M. Schwarz, N. Garzorz, M. Omar, A. Buehler, K. Eyerich, and V. Ntziachristos, "Precision assessment of label-free psoriasis biomarkers with ultra-broadband optoacoustic mesoscopy," *Nature Biomedical Engineering*, vol. 1, no. 5, pp. 1–8, 2017.

[155] M. W. Schellenberg and H. K. Hunt, "Hand-held optoacoustic imaging: A review," *Photoacoustics*, vol. 11, no. 2, pp. 14–27, 2018.

[156] M. Seeger, A. Karlas, D. Soliman, J. Pelisek, and V. Ntziachristos, "Multimodal optoacoustic and multiphoton microscopy of human carotid atheroma," *Photoacoustics*, vol. 4, no. 3, pp. 102–111, 2016.

[157] Y. Zhou, W. Xing, K. I. Maslov, L. A. Cornelius, and L. V. Wang, "Handheld photoacoustic microscopy to detect melanoma depth in vivo," *Optics Letters*, vol. 39, no. 16, p. 4731, 2014.

[158] H. He, A. B. Bühler, and V. Ntziachristos, "Optoacoustic endoscopy with curved scanning," *Optics Letters*, vol. 40, no. 20, pp. 4667–4670, 2015.

[159] B. Dong, S. Chen, Z. Zhang, C. Sun, and H. F. Zhang, "Photoacoustic probe using a microring resonator ultrasonic sensor for endoscopic applications.," *Optics letters*, vol. 39, no. 15, pp. 4372–5, 2014.

[160] J.-M. Yang, C. Li, R. Chen, B. Rao, J. Yao, C.-h. Yeh, A. Danielli, K. Maslov, Q. Zhou, K. K. Shung, and L. V. Wang, "Optical-resolution photoacoustic endomicroscopy in vivo," *Biomedical Optics Express*, vol. 23, no. 4, pp. 362–364, 2015.

[161] J. Bauer-Marschallinger, K. Felbermayer, K.-D. Bouchal, I. A. Veres, H. Grün, P. Burgholzer, and T. Berer, "Photoacoustic projection imaging using a 64-channel fiber optic detector array," *SPIE BiOS*, vol. 9323, p. 93233U, 2015.

[162] T. Dehoux, M. A. Ghanem, O. F. Zouani, J.-M. Rampnoux, Y. Guillet, S. Dilhaire, M.-C. Durrieu, and B. Audoin, "All-optical broadband ultrasonography of single cells," *Scientific Reports*, vol. 5, no. 1, p. 8650, 2015.

[163] X. L. Deán-ben, H. López-schier, and D. Razansky, "Optoacoustic micro-tomography at 100 volumes per second," *Scientific reports*, vol. 7, no. 6850, pp. 1–8, 2017.

[164] S. W. Huang, Y. Hou, S. Ashkenazi, and M. O'Donnell, "High-resolution ultrasonic imaging using an etalon detector array," *Applied Physics Letters*, vol. 93, no. 11, pp. 1–4, 2008.

[165] A. Stylogiannis, L. Prade, A. Buehler, J. Aguirre, G. Sergiadis, and V. Ntziachristos, "Continuous wave laser diodes enable fast optoacoustic imaging," *Photoacoustics*, vol. 9, pp. 31–38, 2018.

[166] *Information for Manufacturers Seeking Marketing Clearance of Diagnostic Ultrasound Systems and Transducers*. American Food and Drug Association, 2008.

[167] *American National Standard for Safe Use of Lasers*. Laser Institute of America, z136.1 ed., 2007.